Performance Enhancement of Wireless Power Transfer Rectenna System for IoT applications

A Thesis Submitted

in Partial Fulfilment of the Requirements

for the Degree of

DOCTOR OF PHILOSOPHY

by

Manoj Kumar

(2018eez0020)

DEPARTMENT OF Electrical Engineering

INDIAN INSTITUTE OF TECHNOLOGY ROPAR

Nov., 2022

To my dear parents, sister, wife, and son.

Declaration of Originality

I hereby declare that the work presented in the thesis entitled **Performance Enhancement of Wireless Power Transfer Rectenna System for IoT Applications** has been solely authored by me. It represents the result of my own independent investigation and research conducted during the period from 07/01/2019, when I joined the Ph.D. program, to 23/11/2022, when I submitted my Ph.D. thesis, under the supervision of Dr. Ashwani Sharma, Assistant Professor. To the best of my knowledge, this is an original work, both in terms of research content and narrative, and has not been submitted or accepted elsewhere, in part or in full, for the award of any degree, diploma, fellowship, associateship, or similar title of any university or institution. Furthermore, I have attributed due credit to the relevant state-of-the-art and collaborations (if any) with appropriate citations and acknowledgments, in line with established ethical norms and practices. I also declare that any idea, data, fact, or source stated in my thesis has not been fabricated, falsified, or misrepresented. I have followed all the principles of academic honesty and integrity. I fully understand that if the thesis is found to be unoriginal, fabricated, or plagiarized, the Institute reserves the right to withdraw the thesis from its archive and revoke the associated degree conferred. Additionally, the Institute reserves the right to appraise all concerned sections of society of the matter for their information and necessary action (if any). If accepted, I hereby consent for my thesis to be available online in the Institute's Open Access repository, inter-library loan, and the title & abstract to be made available to outside organizations.

Signature

Name: Manoj Kumar
Entry Number: 2018eez0020
Program: PhD
Department: Electrical Engineering
Indian Institute of Technology Ropar
Rupnagar, Punjab 140001

Date: 11/05/2023

Acknowledgement

First and foremost, I would like to express my gratitude to the omnipotent power for giving me the fortitude to complete this thesis. I am deeply grateful for the assistance and advice of several well-known individuals, without whom this accomplishment would not have been possible. I want to extend my heartfelt appreciation to my supervisor, Dr. Ashwani Sharma, whose expertise, experience, perceptive conversations, and extensive knowledge have motivated me throughout my research. He taught me a lot, both academically and personally. Thank you for your valuable recommendations and guidance in completing this thesis. I also wish to acknowledge Dr. Ignacio Julio Garcia Zuazola for his excellent assistance and academic advice. I will always be grateful for his encouragement, support, and guidance. Moreover, I would like to express my gratitude to Mr. Sundeep Kumar for his efforts and collaborations in conducting experimental setups for this research. Lastly, I would like to thank all of my friends and colleagues in the RF group at IIT Ropar for providing a wonderful environment for research. Your support and encouragement have been invaluable to me.

Certificate

This is to certify that the thesis entitled **Performance Enhancement of Wireless Power Transfer Rectenna System for IoT applications**, submitted by **Manoj Kumar (2018eez0020)** for the award of the degree of **Doctor of Philosophy** of Indian Institute of Technology Ropar, is a record of bonafide research work carried out under my guidance and supervision. To the best of my knowledge and belief, the work presented in this thesis is original and has not been submitted, either in part or full, for the award of any other degree, diploma, fellowship, associate, or similar title of any university or institution. In my opinion, the thesis has reached the standard fulfilling the requirements of the regulations relating to the Degree.

Signature of the Supervisor

Ashwani Sharma
Electrical Engineering Department
Indian Institute of Technology Ropar
Rupnagar, Punjab 140001

Date: 11/05/2023

Lay Summary

This thesis focuses on improving the performance of wireless power transfer (WPT) rectennas, which concurrently provide wireless charging of sensor nodes. The author proposes four new types of WPT rectennas that are better than the state-of-the-art designs. The results are analysed using simulation and are validated by measurements conducted in the AMR Lab at IIT Ropar. Overall, the research in this thesis aims to make wireless charging of sensor nodes more efficient and effective.

Abstract

The rapid growth of the Internet of Things (IoT) has led to an increased demand for monitoring various types of data for different applications, including home automation, smart cities, and industrial applications. However, due to the limited battery capacity of IoT sensor nodes, replacing or recharging a large number of batteries can be prohibitively costly and labor-intensive. Therefore, Wireless Power Transfer (WPT) is a potential option that uses a dedicated RF transmitter (Tx) and a rectenna (Rx) system deployed at the IoT sensor node for remote battery recharge or even battery-less operations. However, real-world applications continue to necessitate the optimal design of a rectenna. The cutting-edge designs suffer from significant research problems such as angular misalignment, non-uniform 3-D coverage, and non-scalability in WPT rectenna systems. This thesis is divided into seven chapters. The first two chapters present the research problems and a fundamental description of WPT rectennas. Chapter 3 presents an analytical framework for mitigating angular misalignment by driving specific conditions on the DC power pattern. Following the analytical framework, three antennas with omnidirectional capabilities in the azimuth plane are designed to improve power conversion efficiency (PCE). Furthermore, chapter 4 analyzes the non-uniform coverage of the transmitter (Tx) by employing two novel fully integrated planar multi-sector rectenna arrays to obtain substantially uniform 3D spherical DC coverage. Chapter 5 presents dynamic power harvesting and polarization-insensitive operations employing a scalable plug-in-type WPT system. The scalable technique eliminates the need to design various rectenna modules if the energy needs or orientation of the sensor nodes change in an IoT application, resulting in a low-cost system. Chapter 6 presents several WPT-enabled IoT antennas for long reading range, robustness, and platform tolerance. Chapter 7 presents the conclusion and future work in the WPT rectenna system. Thus, this thesis presents a new WPT system that can be used for future applications that require efficient WPT.

Keywords: Angular misalignment, Integrated rectennas, Omnidirectional IoT rectenna, Multisector wireless power transfer, Scalability, wireless sensor nodes

List of Publications

Journal

Article 1

M. Kumar, S. Kumar and A. Sharma, "A Planar Orbicular Rectenna Array System With 3-D Uniform Coverage for Wireless Powering of IoT Nodes," in ***IEEE Transaction Microwave Theory Techniques***, vol. 71, no. 3, pp. 1366-1373, March 2023, doi: 10.1109/TMTT.2022.3217073.

Article 2

M. Kumar, S. Kumar and A. Sharma, "An Analytical Framework of Multisector Rectenna Array Design for Angular Misalignment Tolerant RF Power Transfer Systems," in ***IEEE Transaction Microwave Theory Techniques***, vol. 71, no. 4, pp. 1835-1847, April 2023, doi: 10.1109/TMTT.2022.3222195.

Article 3

M. Kumar, S. Kumar, A. S. Bhadauria and A. Sharma, "A Planar Integrated Rectenna Array With 3-D-Spherical DC Coverage for Orientation-Tolerant Wireless-Power-Transfer-Enabled IoT Sensor Nodes," in ***IEEE Transaction Antenna and Propagation***, vol. 71, no. 2, pp. 1285-1294, Feb. 2023, doi: 10.1109/TAP.2022.3228708.

Article 4

M. Kumar, S. Kumar, S. Jain and A. Sharma, "A Plug-in Type Integrated Rectenna Cell for Scalable RF Battery Using Wireless Energy Harvesting System," in ***IEEE Microwave and Wireless Components Letters***, vol. 33, no. 1, pp. 98-101, Jan. 2023, doi: 10.1109/LMWC.2022.3202711.

Article 5

M. Kumar, S. Kumar and A. Sharma, "Dual-Purpose Planar Radial-Array of Rectenna Sensors for Orientation Estimation and RF-Energy Harvesting at IoT Nodes," in ***IEEE Microwave and Wireless Components Letters***, vol. 32, no. 3, pp. 245-248, March 2022, doi: 10.1109/LMWC.2022.3145196.

Article 6

M. Kumar, S. Kumar and A. Sharma, "A Compact 3-D Multisector Orientation Insensitive Wireless Power Transfer System," in ***IEEE Microwave and Wireless Technology Letters***, vol. 33, no. 3, pp. 363-366, March 2023, doi: 10.1109/LMWC.2022.3212599.

Article 7

M. Kumar, A. Sharma, and I. J. G. Zuazola, "Compact UHF RFID Balun-Like Integrated Tag Antenna for Long Range Detection of Water Bottles," in ***IET Microwaves, Antennas and Propagation***, vol. 13, no. 4, pp. 1-11, Sep. 2022, doi: 10.1049/mia2.12299.

Article 8

S. Agarwal, A. Sharma, IJ. Garcia Zuazola, and **M. Kumar**, "A compact SWB MIMO Antenna with 45° Clock-wise Square Patch Inclusions for Polarization Diversity

Applications", in ***International Journal of Microwave and Wireless Technologies***, vol. 15, no. 3, pp. 513–525, Apr. 2022, doi: 10.1017/S1759078722000435.

Article 9

M. Kumar, A. Sharma, and I. J. G. Zuazola, "All-in-One UHF RFID Tag Antenna for Retail Garments Using Nonuniform Meandered Lines," in ***Progress In Electromagnetics Research Letters***, Vol. 94, 133-139, 2020.

Article 10

M. Kumar, A. Sharma, and I. J. G. Zuazola, "Bendable UHF RFID Tag Antenna for Retail Garments using Nonuniform Meandered Lines", in ***Engineering Reports***, vol. 3, no. 11, pp. 1-11, Feb. 2021.

Conference Proceeding

Article 1

M. Kumar, S. Agarwal and A. Sharma, "A Multi-application Compact Ultra Wideband Vivaldi Antenna for IoT, 5G, ITS, and RFID," 2019 ***IEEE Indian Conference on Antennas and Propagation (InCAP)***, 2019, pp. 1-3.

Article 2

M. Kumar, A. Sharma and I. J. G. Zuazola, "A biodegradable multi-platform tolerant passive UHF RFID tag antenna for short-life cycle IoT applications," 2021 ***IEEE Indian Conference on Antennas and Propagation (InCAP)***, 2021, pp. 391-394.

Article 3

S. Jain, **M. Kumar** and A. Sharma, "A Highly Efficient Compact High Gain RFID Tag Antenna for Millimeter Wave Applications," 2021 ***IEEE Indian Conference on Antennas and Propagation (InCAP)***, 2021, pp. 402-404, doi: 10.1109/InCAP52216.2021.9726189.

Acronyms

2-D Two Dimensional

3-D Three Dimensional

5G Fifth Generation

ADS Advance Design Simulator

BSR Bore-Sight Rectenna

CP Circular Polarised

CPW Coplanar waveguide

DC Direct Current

DC-LPF DC-Low Pass Filter

EFR End-Fire Rectenna

EM Wave Electromagnetic Wave

HFSS High Frequency Structure Simulator

IoT Internet of Things

IMN Impedance Matching Network

LP Linear polarised

LSSP Large Signal S-Parameters

MRC Magnetic Resonance Coupling

MPA Microstrip Patch Antenna

RF Radio Frequency

PCE Power Conversion Efficiency

PMN Power Management Network

SMD Surface Mounted Device

WPT Wireless Power Transfer

VD Voltage Doubler

Contents

List of Figures

List of Tables

Chapter 1

Introduction

1.1 Introduction

The next generation wireless communication system will enable the large-scale deployment of small IoT nodes for data collection and information analysis in various smart applications. The foreseen requirements include smart homes, offices, transportation, medical, and industrial applications [1, 2], which are expected to reach a market value of over 30.9 billion by 2025. Essentially, to achieve sustainability in these smart applications, future wireless systems need to enable the deployment of zero-energy IoT sensor nodes [3]. This can be achieved by utilizing various energy harvesting schemes to recharge sensor node batteries or enable batteryless operation. This will enhance the lifetime of wireless sensor networks, eliminating the need for frequent battery replacement or redeployment of sensor nodes, resulting in a drastic reduction in maintenance costs [4]. Several wireless recharging technologies exist to enhance the battery life of IoT nodes, including solar, wind, vibration, and electromagnetic waves (EM waves). However, sun, wind, and vibration energy sources are dependent on climatic conditions, making them impractical for indoor applications. The prevalence of RF sources, such as radio, cellular, and WiFi networks, makes RF power a potential source for battery charging in indoor scenario [5]. This technique is frequently known as wireless power transfer (WPT), which can be divided into near-field (inductive and magnetic resonance coupling) [6] and far-field (ambient and dedicated WPT) [7], as shown in Fig. 1.1.

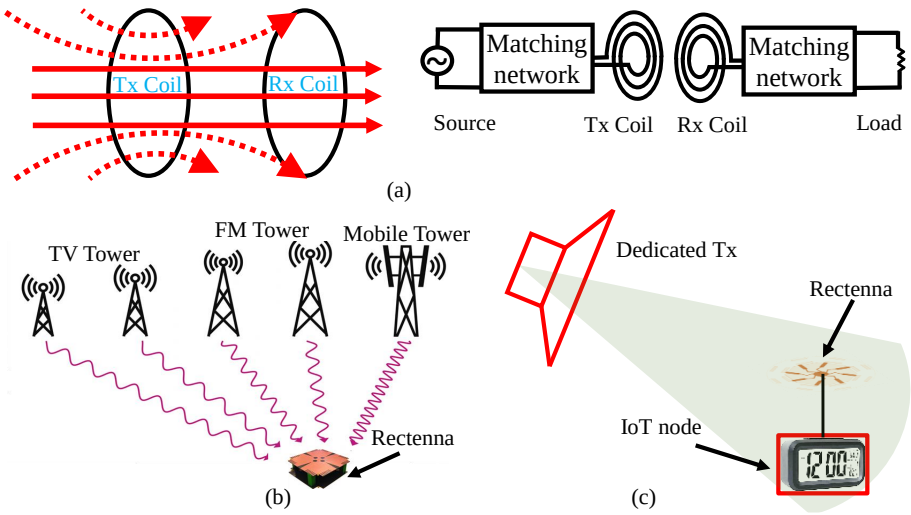

Figure 1.1: (a) Near-field, (b) far-field ambient, and (c) far-field dedicated WPT.

The former utilizes inductive and magnetic resonance coupling techniques [6, 7] to provide

substantial power over a short range. However, these techniques are unsuitable for charging a large number of sensor nodes over a longer distance. Therefore, far-field WPT has received significant attention for charging IoT nodes ranging from a few meters to kilometers [8]. This technique utilizes radiating antennas [6, 7, 8],which can be broadly classified into ambient and dedicated power transfer techniques. The ambient WPT offers intermittent RF power from mobile towers and Wi-Fi networks operating in free licensed frequency bands [7, 8], i.e., 80 MHz, 900 MHz, 1.8 GHz, 2.4 GHz, 3.6 GHz, 5.2 GHz, and 5.8 GHz. However, due to the low power density of this technique, battery-free operation seems impossible. To address this problem, a dedicated WPT system can be employed to recharge IoT nodes, as shown in Fig. 1.1 (c). This includes a dedicated transmitter (T_x) antenna and a rectifying antenna commonly known as a rectenna [9]. The performance of the rectenna depends on the transmitted power (Ptx), Rectenna (Rx)-gain, and matching network efficiency (η_{mn}) [10]. Therefore, it is important to consider these factors while designing a dedicated WPT system. In a dedicated WPT system, T_x can be installed

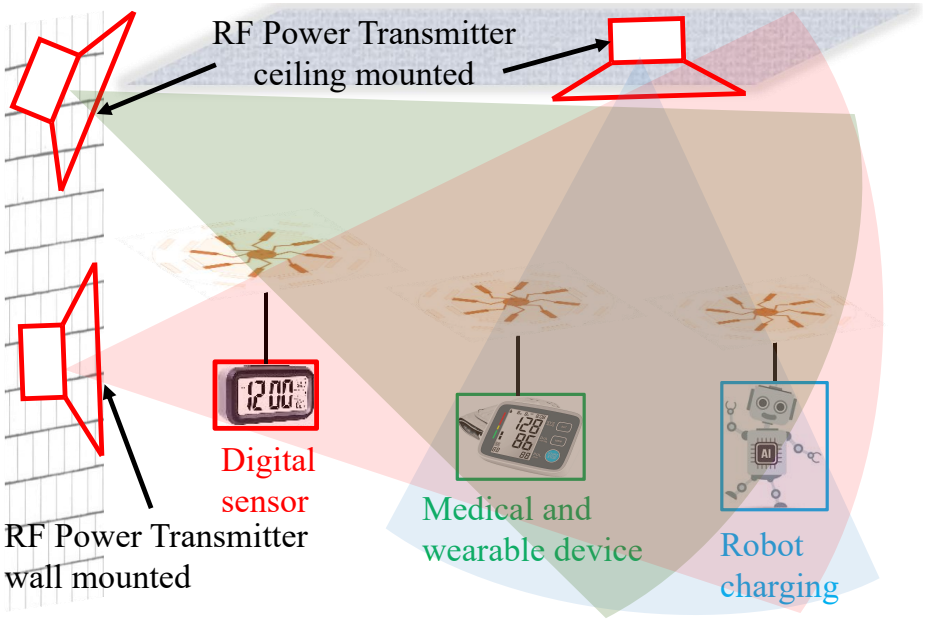

Figure 1.2: Generalized applications of far-field techniques.

on walls and ceilings to recharge randomly distributed IoT sensor nodes, as shown in Fig. 1.2. However, this system suffers from various significant problems resulting in low power conversion efficiency (PCE). These challenges and their impact on the performance of the system are discussed in detail in Section 1.1.1.

1.1.1 Problems in the Dedicated WPT system

The dedicated WPT system suffers from low PCE [11] due to the following problems,

- Angular misalignment.
- Non-uniform 3-D DC coverage of the R_x.

- Distributed impedance matching network R_x resulting in bulky design in a space constraint sensor nodes.
- Non-scalable rectenna unsuitable for dynamic power requirement application scenario.
- Platform-dependent, lack of robustness and large footprint.

The PCE is the ratio of harvested DC power to captured RF power, which primarily depends on the rectifier circuit deployed for RF to DC conversion [12]. It is worth noting that the PCE of the rectifier is directly proportional to its input RF power [13]. Therefore, it is essential to design the rectenna system in such a way that it can efficiently capture the RF power, ensuring that a high PCE can be achieved. Several WPT

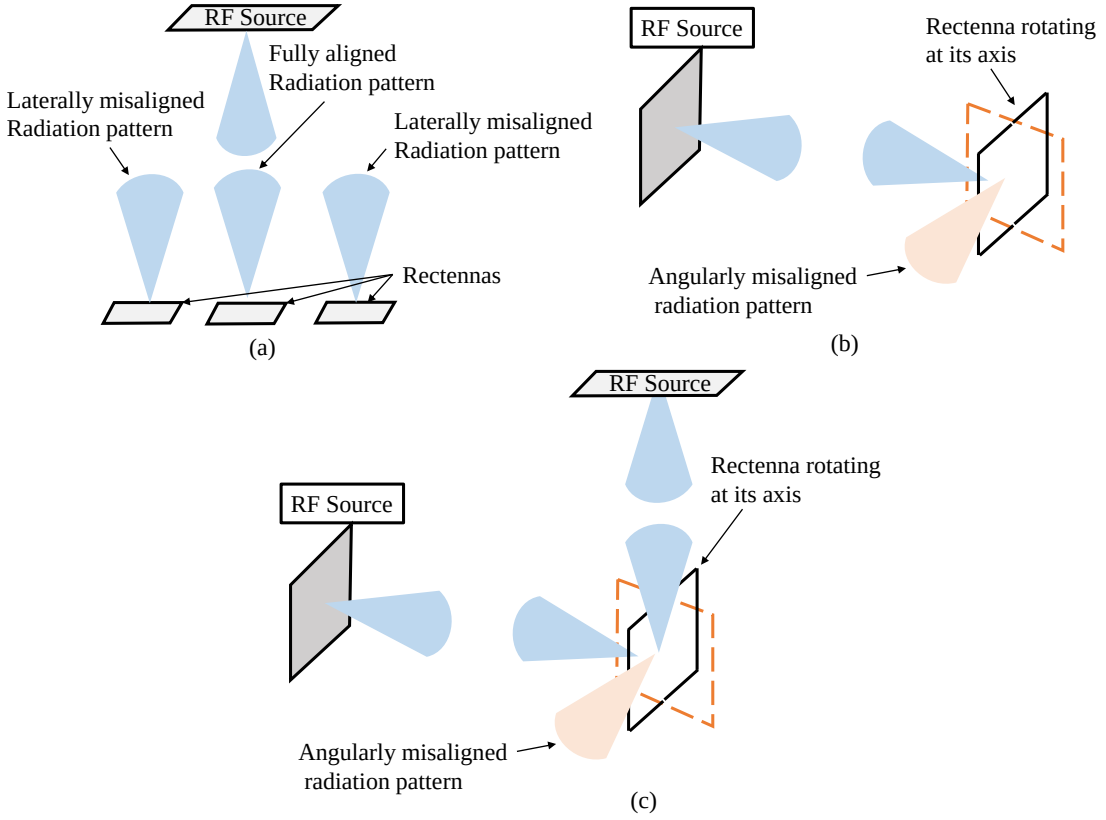

Figure 1.3: (a) Lateral misalignment (b) Angular misalignment and (c) 3-D spherical misalignment.

rectenna systems are designed to enhance the PCE by utilizing second harmonics [14, 15], multi-polarization [16], wide-dynamic range rectennas [17], and high-gain rectenna arrays [18]. Although high-gain rectennas offer high PCE, however, the tolerance against angular misalignment decreases due to narrow beam width [19]. In general, lateral [20, 21], angular, and 3-D spherical misalignments [20, 22, 23, 24, 25] of WPT systems are shown in Fig. 1.3. These misalignments occur due to variations in the R_x location [26] and the relative rotation between R_x and T_x position, respectively. In 3-D spherical misalignment, tilted or rotated [27] sensor nodes offer low-power harvesting capabilities. Therefore,

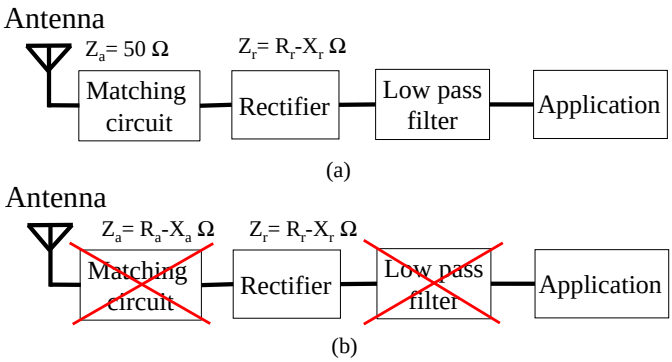

Figure 1.4: (a) Conventional and (b) conjugate matched rectenna topologies.

customization of the R_x at WPT nodes is necessary to ensure orientation-oblivious [11, 28] continuous DC power harvesting with high PCE. Furthermore, conventional WPT rectennas employ distributed impedance matching networks (IMN) [29] to match the impedance of the receiving antenna (50Ω) [30] with the rectifier input impedance, and further employ a DC-low pass filter (DC-LPF) to eliminate higher-order harmonics, as shown in Fig. 1.4(a). Some sensor nodes require power and polarization insensitivity to perform their functions smoothly, which can be achieved with the scalable features of the rectenna system. A miniaturized and platform-tolerant WPT rectenna system is the most commonly chosen approach for achieving efficient IoT nodes. Prior work on the WPT system is discussed in Section 1.1.2.

1.1.2 Prior Work and Motivation

This thesis covers several research areas, including angular misalignment problems, dynamic power harvesting, integrated rectennas, and 3-D and 2-D planar designs, which are highlighted in gray in Fig. 1.5. The literature is organized based on these areas, starting with the angular misalignment problem. This issue can be addressed by analyzing and categorizing the directional characteristics of the RF and DC patterns [31] of the WPT rectenna. The former measures the RF radiation pattern [32], whereas the latter analyzes the harvested DC power pattern [33] of the WPT element. Therefore, the DC pattern can determine the angular misalignment tolerance of the WPT node [34]. An omnidirectional DC pattern implies complete mitigation of the angular misalignment issue [35]. Therefore, the WPT antenna is customized to produce a specific RF pattern corresponding to the desired DC pattern. Although the RF pattern shapes the DC pattern of the rectenna, the two are not always identical due to various circuit elements (matching circuits, filters, rectifier, and RF-DC combiner) cascaded along the RF to DC conversion path and their effects in terms of rectifier non-linearity [36], efficiency, and attenuation [37]. Particularly for the WPT node employing a single antenna element, an omnidirectional RF pattern implies an omnidirectional DC pattern. Therefore, dipoles [11] and monopoles [38] become the appropriate choices for the single antenna element. However, such conventional antennas with a single element exhibit low RF gain, which significantly compromises

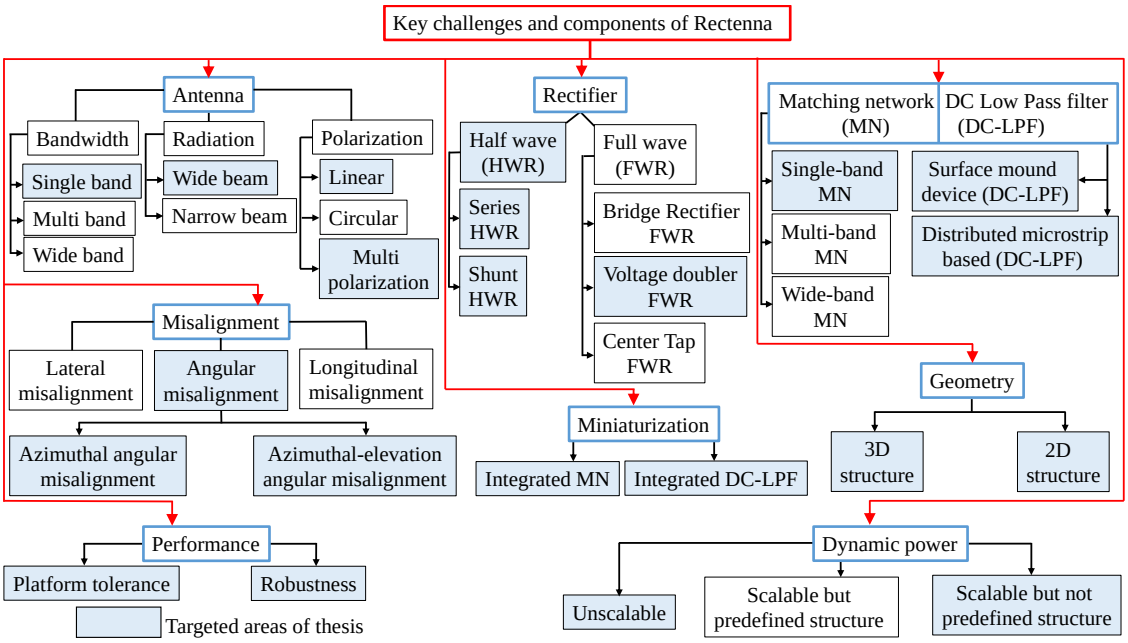

Figure 1.5: Research areas in WPT-Rectenna system

.

the PCE and the harvested DC power. To improve spatial coverage and harvested DC power, WPT nodes with multiple sectors, combined using RF combining [39] and DC combining [40] techniques, are discussed in Section 2.3.3. However, such conventional antennas with a single element exhibit low RF gain, which significantly compromises the PCE and the harvested DC power. To improve spatial coverage and harvested DC power, WPT nodes with multiple sectors, combined using RF combining [39] and DC combining [40] techniques, are discussed in Section 2.3.3.

For instance, WPT systems with multi-port rectennas in [35, 41, 42, 43] are combined using DC combining approaches to improve azimuth coverage. Though these designs improved PCE and harvested DC, mitigating the angular misalignment problem is unattended. Similarly, the six-beam Rotman Lens rectenna array presented in [44] achieves an angular coverage of 140° only, and therefore, has a low tolerance for angular misalignment. Moreover, the large dimension renders it unsuitable for small WPT nodes. Recently, multi-sector structures of rectenna arrays have been designed to harvest RF power from the entire 360° of the azimuth plane. For instance, a multi-sector planar quasi Yagi rectenna having a narrow beam is presented in [45]. The low angular coverage requires a large number of sectors to achieve 360° coverage, making it unsuitable due to mutual coupling and dimensional constraints. In contrast, a planar radial array of eight rectennas is presented in [34] to estimate the orientation and harvest RF energy with improved angular misalignment tolerance for orientation-oblivious operation. Similarly, a few 3-D multi-sector rectenna arrays are investigated in the literature to enhance the spatial angular coverage. For instance, two-sector rectenna [46], cubic-shape structure [47], three-sector [35], four-sector [39], and six-sector [48, 49, 50, 51] rectenna arrays have been presented. Moreover, a five-sector cylindrical structure with a patch array is

presented in [28],[52] and integrated with a hybrid combining technique [53] to enhance the angular coverage in the elevation and azimuth plane. The major limitation of the aforementioned designs is their inconsistent DC patterns, which resemble star shapes rather than the desired omnidirectional patterns in the azimuth plane. In contrast, a consistent omnidirectional DC pattern response is achieved by utilizing six Yagi-Uda [54] and twelve Vivaldi rectennas [55]. However, concrete analytical evidence needs to be provided to choose and relate the optimal number of sectors with the DC pattern of the rectenna element. Moreover, these WPT systems have a large footprint, which is unsuitable for IoT nodes. Correspondingly, the immediately-reported designs need to provide 3D-spherical coverage to completely mitigate the angular misalignment.

Further, the immediately mentioned designs do not have the capability of polarization-insensitive [56, 57, 58], miniaturization, and dynamic DC power harvesting [59] for diverse power requirements. Some other scalable [60, 61] and orientation-insensitive [62, 63, 64], and differential WPT rectenna systems [65, 66, 67, 68, 69, 70] are reported to improve the power harvesting. Similarly, designs with integrated impedance matching also exist employing frequency selective surface (FSS) for scalability and polarization-insensitive operation. For instance, FSS-based full-wave integrated dipole rectenna [71, 72], tightly coupled antenna (TCA)[73], and stacked half-wave dipole FSS rectenna[74] are presented to enhance power conversion efficiency (PCE). The major limitations of these designs are their large fixed footprints and complex impedance matching with the rectifier circuit, rendering them unsuitable for IoT applications. The scarcity of orientation-insensitive, miniaturized, low-profile, and scalable rectenna systems encourages designing a novel WPT system along with all the required capabilities. Various cutting-edge low-profile and miniaturized receiving antennas have been reported in the literature. For instance, aperture-coupled dual linear patch antenna [75], CPW-fed patch [76], microstrip-fed dipole [77], inverted-F planar [78], folded dipoles [79, 80], printed flat dipole antenna [81, 82], ME dipole [83], antipodal Vivaldi [84], fractal [85], MIMO, monopole [86], dual loops [87], Yagi [88], dielectric resonator antennas [89], patch [90], π-shaped multi-layer PIFA meandering strip [91], slot-loaded folded dipole [92], and L-probe stacked patch rectenna [93] are shown in Fig. 1.6. Multiband and wideband antennas are the foremost choices for ambient RF energy harvesting. In contrast, dedicated WPT systems usually prefer single narrow-band antennas to improve the quality factor of the WPT system. Linear polarized (LP) and circular polarized (CP) antennas significantly affect the performance of a WPT system. This is because LP antennas [94] capture EM power from a single plane, either horizontal or vertical, whereas CP antennas [95, 96] harvest power from both horizontal and vertical planes simultaneously. Therefore, a CP antenna can be a better choice to improve polarization diversity, although with the trade-off of reduced power in each polarization. To address this issue, some multi-polarization rectenna systems have been designed [97, 98], but these systems have large dimensions, which make them unsuitable for IoT applications.

The state-of-the-art designs have different sectors for different rectenna elements selected

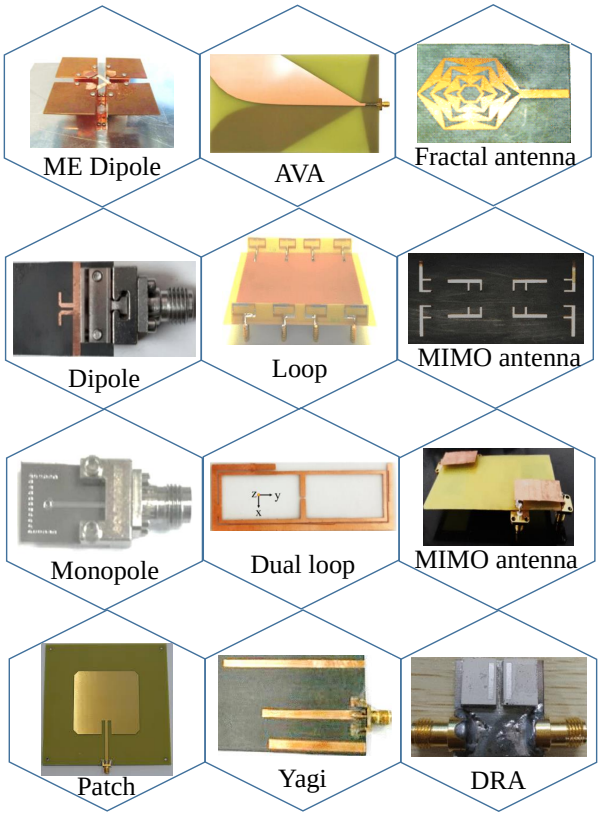

Figure 1.6: State-of-the-art antenna designs.

by qualitative analysis of the RF patterns, which makes them unsuitable for addressing the problem of orientation misalignment. However, concrete analytical evidence is required to select and relate the optimal number of sectors with the DC pattern of the rectenna element to mitigate angular misalignment and achieve 3D spherical DC coverage. Moreover, the cutting-edge designs lack scalability, polarization insensitivity, and miniaturization features altogether and have a predefined structure that is unsuitable for dynamic power harvesting applications. Therefore, the proposed work aims to conduct a comprehensive study and provide a novel mathematical framework along with an innovative antenna element for full angular misalignment mitigation with plug-in type scalable rectenna modules.

1.2 Thesis Objective

The major objective of this thesis is to design an orientation-insensitive, miniaturized, low profile, scalable and robust WPT rectenna system.
To achieve the objective of the thesis following are the sub-objectives.

Sub-objectives:

H1: To develop an analytical frame work to mitigate the azimuthal angular misalignment.
↳ By optimising DC power patterns of adjacent sectors.

H1A1: Drive an analytical framework to synthesize an optimal DC pattern of the rectenna element with a compact WPT system to mitigate the angular misalignment problem.

H1A2: Drive conditions on the radiation pattern to mitigate the angular misalignment problems using a high-gain WPT system.

H1A3: Design a planar WPT system with orientation estimation capabilities by improving tolerance against angular misalignment.

H2: To develop a WPT system with 3D-Spherical coverage to address the issue of orientation misalignment.
↳ By optimising DC power patterns in elevation and azimuth planes.

H2B1: To design a tilted beam bore-sight and an end-fire integrated rectenna sector that can offer azimuth and elevation coverage with preserving an acceptable PCE.

H2B2: To address 3D-spherical coverage problems by designing a fully integrated, compact WPT rectenna system.

H3: To design a rectenna system with scalability, polarization-insensitive, dynamic power harvesting, and miniaturization capabilities to address the problem of low PCE.
↳ By designing a scalable, extendable rectenna cell that can be used per the application power demand.

H3C1: To design a multi-function Plug-In type WPT rectenna cell that can be deployed according to application requirements.

H4: To design antennas by developing novel techniques to make them a surface-tolerant, miniaturize and long-range WPT system.

H4D1: To design a long range, robust and miniaturized antenna by developing a novel dual loop and non-uniform meander-line technique.

The following targets are achieved to fulfill the above mentioned sub-objectives.

1.3 Thesis Outline

This thesis comprises seven chapters covering azimuthal angular misalignment, 3D-spherical coverage, scalability, and IoT antennas for WPT applications. The chapter description of this thesis is outlined as follows:

Chapter 1: This chapter presents an overview of the WPT system, including a literature survey, motivation, objectives, and thesis outline.

Table 1.1: Targets achieved in the sub-objectives.

Outcomes	Angular misalignment	3D-spherical coverage	3D design	Planner design	Integrated design	Scalability	Miniaturization	Robustness	Long Reading range
H1-A1	✓	×	✓	×	×	×	×	×	✓
H1-A2	✓	×	✓	×	×	×	✓	×	✓
H1-A3	✓	×	−−	−−	×	×	✓	✓	×
H2-B1	✓	✓	×	✓	✓	×	×	✓	✓
H2-B2	✓	✓	×	✓	✓	×	✓	✓	✓
H3-C1	✓	✓	✓	✓	✓	✓	✓	✓	✓
H4-D1	×	×	×	✓	✓	×	✓	✓	✓

✓ Achieved objectives.
× Not achieved objectives.
−− This is a planner design, however the enclosure has 3d metallic walls.

Chapter 2: This chapter presents the basic building blocks of a conventional WPT system with theoretical backgrounds of rectenna analysis, simulations, and measurement processes. RF and DC combining techniques are discussed to design a multisector rectenna array to enhance the performance of the WPT system.

Chapter 3: This chapter presents an analytical framework to mitigate the azimuthal angular misalignment for sub-objective: H1 and design a miniaturized (H1A1), high-gain (H1A2), and planar (H1A3) WPT system.

Chapter 4: For sub-objective H2, this chapter presents novel design procedure for achieving 3D-spherical coverage using planar design. To evaluate the 3D-spherical coverage, the output DC voltage and PCE are investigated using simulation and measurements.

Chapter 5: This chapter introduces sub-objective: H3, which presents a novel scalable WPT scheme for dynamic power harvesting and polarization-insensitive operations.

Chapter 6: This chapter introduces sub-objective: H4, which presents robust WPT systems for high-dielectric and low-dielectric materials for IoT applications. The analytically calculated reading range of IoT antennas is verified by simulation and measurements.

Chapter 7: This chapter presents the conclusion and future scope to improve the performance of the WPT system.

Chapter 2

Theoretical background: Conventional Rectenna system for WPT

The previous chapter presented a comprehensive literature survey on the challenges of angular misalignment, scalability, miniaturization, and antenna inefficiencies in the context of WPT systems for IoT applications. This chapter builds upon that knowledge and focuses on the fundamental components of a conventional WPT system, which includes rectenna analysis, simulation, and measurement processes [99, 100]. Additionally, a multisector rectenna array is designed to achieve orientation-insensitive operations by using a conventional patch antenna and several DC combining techniques [101, 102]. The performance of the proposed design is evaluated through simulations and measurements, demonstrating improved power harvesting capabilities for IoT nodes.

2.1 WPT Rectenna system

2.1.1 Basic Building Blocks of Rectenna System

The basic building blocks of the rectenna system are shown in Fig. 2.1, which include a 50 Ω conventional antenna, a matching network, rectifying circuits, a low pass filter (LPF), and a power management network (PMN) [103]. The RF power is captured by the

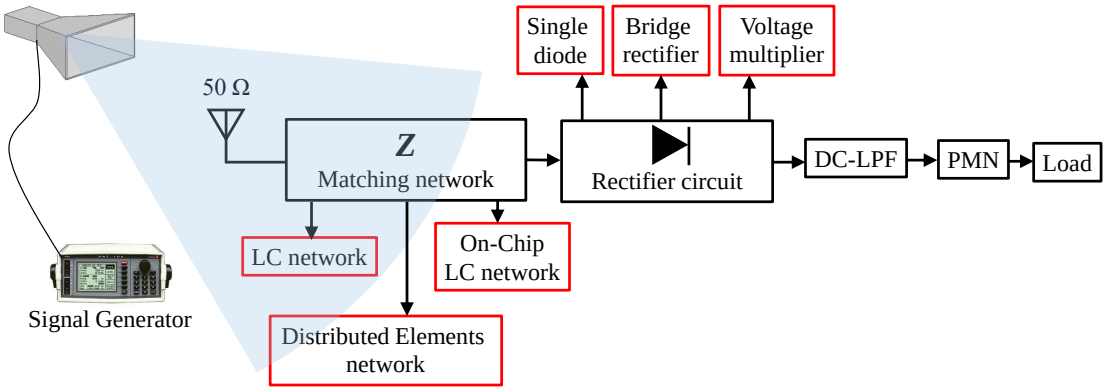

Figure 2.1: Block diagram of the WPT system.

50 Ω conventional antenna and rectified using a rectifier circuit, as shown in Fig. 2.1. The resulting DC voltage is subsequently passed through a DC low pass filter (DC-LPF) to obtain a ripple-free output DC voltage [104]. Additionally, a power management network (PMN) [105] is employed to regulate the output DC power level to fulfill the requirements of various IoT nodes. The performance of the WPT rectenna system is evaluated in terms

of its power conversion efficiency (η) [106], which is presented in subsection 2.1.2.

2.1.2 Power conversion efficiency (η)

The η is the ratio of output DC power P_{dc} to the received RF power P_{rx} at the antenna aperture [12, 106]. This can be calculated, as

$$\eta = \frac{P_{dc}}{P_{rx}} \times 100\%. \tag{2.1}$$

Further, P_{dc} is evaluated by harvested DC voltage [107], which is estimated across the optimal load as,

$$P_{dc} = \frac{V_{dc}^2}{R_l}. \tag{2.2}$$

Moreover, in Equation 2.1, the P_{rx} is received RF power, which is calculated using the Friis transmission equation [108], as

$$P_{rx} = P_t + G_t + G_r + 20log_{10}\left(\frac{\lambda}{4\pi r}\right) \tag{2.3}$$

In Equation 2.3, P_t is the transmitted power, G_t is Tx antenna gain, G_r is the simulated antenna gain, λ is the signal wavelength and r is the distance between Tx and rectenna system. Moreover, in Equation 2.3, the WPT systems suffer from low power density [15] due to path losses, which can be improved using high-gain antenna arrays or directional antennas.

2.2 Research Areas in WPT rectennas

The WPT rectenna system has multiple research areas [109], including antennas [110], matching networks [111], rectifier circuits [112], DC filters [113], and power management circuits [114], as shown in Fig. 2.2. To design an efficient WPT rectenna, various types of high-gain, multi-polarized, wideband, and multiband antennas are reported in Section 1.1.2. Furthermore, the performance of the WPT rectenna also depends on the matching network and rectifier circuits, which are discussed in the following subsections.

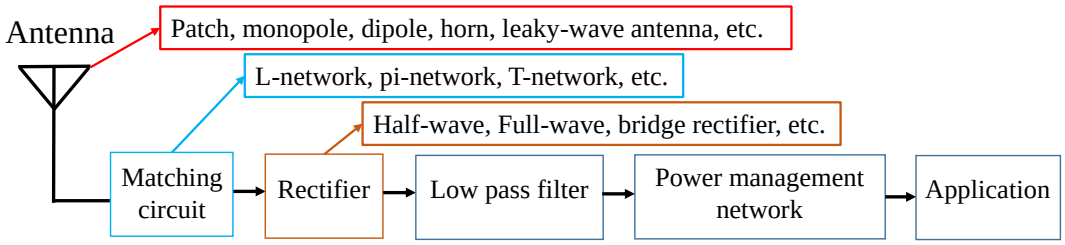

Figure 2.2: Research Scopes in the WPT system.

2.2.1 Matching Network

According to the maximum power transfer theorem, the maximum PCE is obtained when the impedances of the rectifier circuit and antenna are matched as complex conjugates [98].

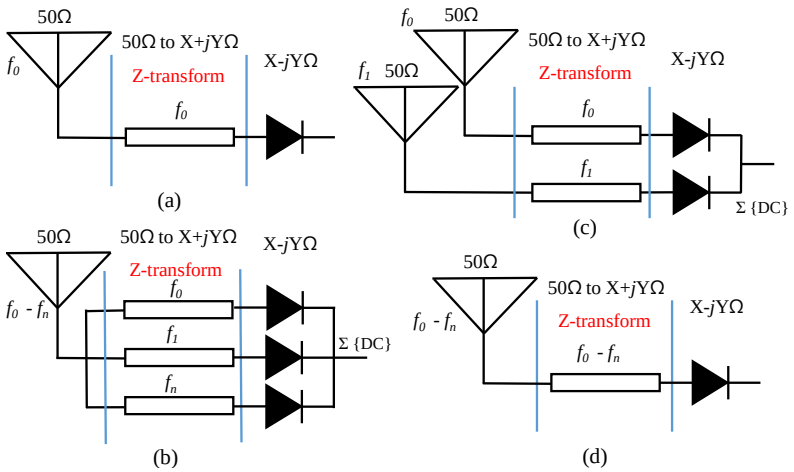

Figure 2.3: Various antenna and rectifier typologies of the WPT system.

The conventional antennas and rectifier circuits are integrated with matching circuits to improve the PCE. In the literature, various matching network topologies are reported to improve harvesting capabilities, i.e., single-band [34], multiband [115], and wideband impedance matching networks [111, 116], as shown in Fig. 2.3. The single-band rectifier circuit is utilized to improve the PCE by achieving a higher quality factor. Moreover, multiband and wideband matching networks are employed to harvest RF energy from the ambient scenario.

2.2.2 Rectifier circuits

In the WPT system, the Schottky diode is used as a rectifying element, and its performance is determined by the input RF power, series resistance (R_s), breakdown voltage (V_{br}), and junction capacitance (C_j) [117, 118, 119]. For instance, at low power levels, PCE reduced due to corresponding forwarding voltage drop. The equivalent circuit of a Schottky

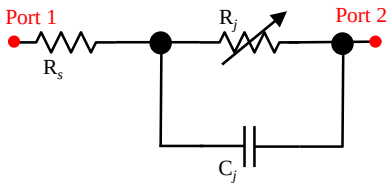

Figure 2.4: Equivalent circuit of Schottky diode.

diode [120, 121] is depicted in Fig. 2.4. The junction resistance (R_j) provides a non-linear resistance with a non-linear behavior of the Schottky diode because each diode has a different voltage breakdown potential.

2.2.3 ADS simulation

The rectifier circuit is designed using ADS software to characterize the performance and impedance of the Schottky diode, as shown in Fig. 2.5. The complete rectifier circuit comprises a 50Ω power port, a DC block capacitor, a Smith chart utility, and a Schottky

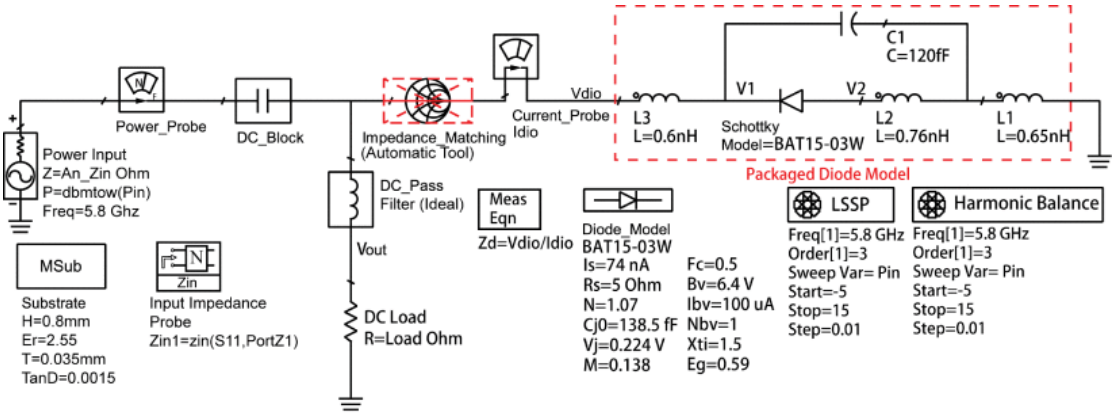

Figure 2.5: ADS simulation schematic diagram.

diode to analyze the results [121]. The diode impedance at the desired frequency is determined using the Large Signal S-Parameters and harmonic balancing techniques. It is important to note that the impedance of the Schottky diode depends on the operating frequency, DC load, and input power level. Further, various rectifier techniques are discussed in Section 2.2.4.

2.2.4 Rectifier Topologies

Various rectifier topologies are shown in Fig. 2.6, which include series [122], shunt [123], and voltage doubler configurations [124]. The shunt and series rectifier topologies are

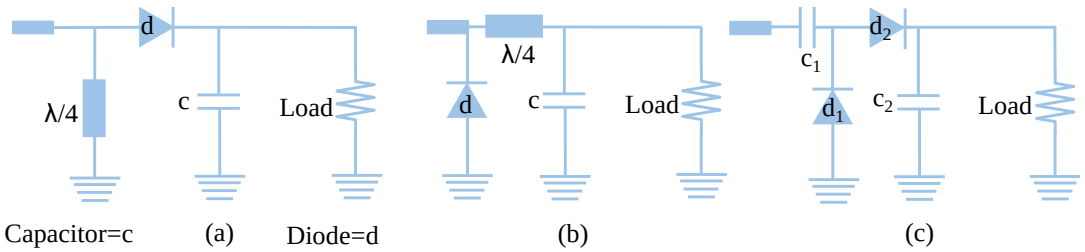

Figure 2.6: Rectifier topologies (a) series half-wave (b) Shunt half-wave and (c) Voltage doubler rectifier circuit.

widely used in low-power applications (below -5dBm). Similarly, voltage doubler topology rectifies both positive and negative cycles of EM waves at high power levels. Moreover, the DC-Low pass filter removes the noises and smooths the output DC power to make a ripple-free circuit. A complete WPT rectenna system is designed in the section 2.3.

2.3 Complete Conventional WPT Rectenna Design

2.3.1 Conventional Microstrip Patch Antenna

The conventional microstrip patch antenna (MPA) [125] is used because of its low profile, high gain, low fabrication cost, and easy integration with small circuits. This is designed on a dual-sided copper cladded FR4 substrate (dielectric loss, $\epsilon_r = 4.4$, and loss tangent

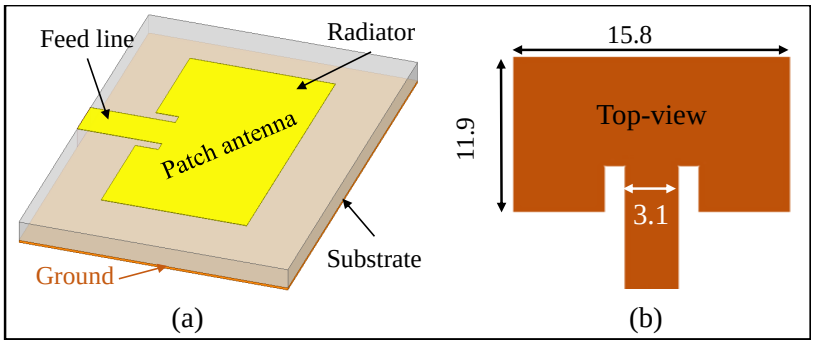

Figure 2.7: Geometry and layout of the MPA.

tanδ = 0.02) using ANSYS HFSS software at 5.8 GHz. The dimensional parameters of the MPA is depicted in Fig. 2.7. The simulated reflection coefficient (S11) and 2-D gain

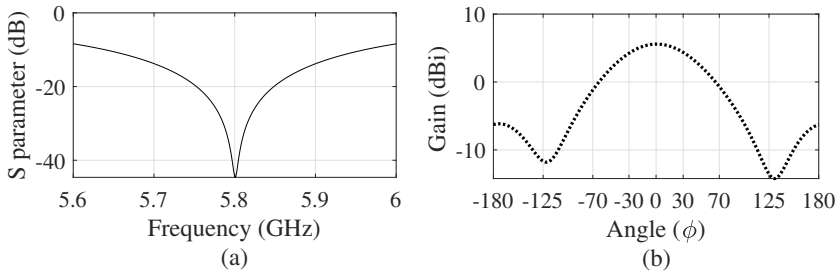

Figure 2.8: (a) Reflection coefficient (b) Gain pattern of the conventional patch antenna.

pattern of the MPA are shown in Fig 2.8. Further, literature reported various feeding

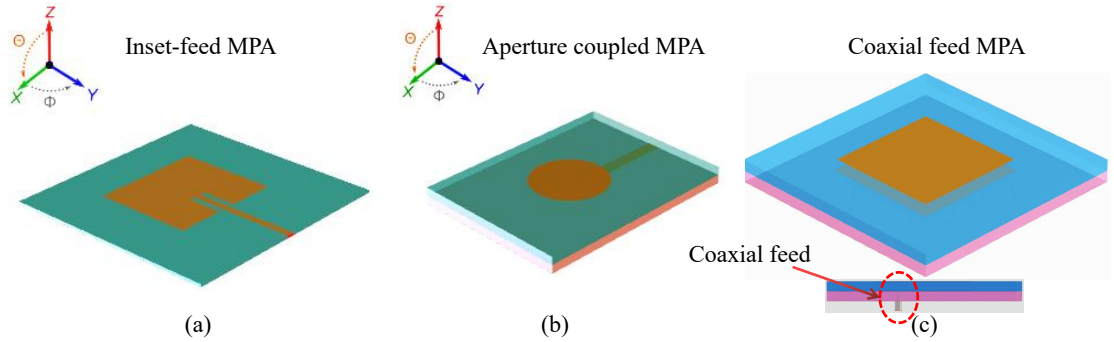

Figure 2.9: Feeding network techniques.

structures, i.e., inset, co-axial and aperture coupled feedings as shown in Fig. 2.9. Each feeding network has particular bandwidth, isolation, and radiation pattern properties.

2.3.2 Integration of Antenna, Matching Network and Post Rectification Low Pass Filter

The matching network and low pass filter are designed in the Keysight ADS software at −10 dBm power level, taking into account the nonlinear effects of the Schottky diode (SMS-7630-079LF). The matching network is designed with two open stubs and one shorted stub for better impedance matching, as illustrated in Fig. 2.10 (a). These stubs

are tailored to reduce the impacts of higher-order harmonics and increase the efficiency of the WPT system. Moreover, the output DC-LPF is optimized in ADS software with four

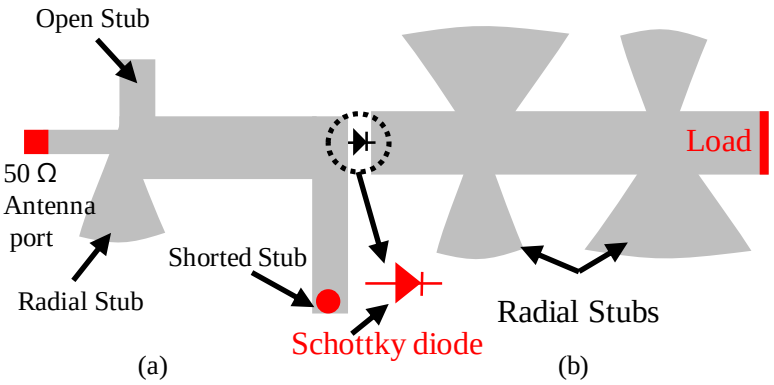

Figure 2.10: (a) Impedance matching network (b) post rectification filter.

radial stubs to reduce noise and ripples in output DC voltage. The layout of the DC-LPF is depicted in Fig. 2.10 (b). The complete layout of the conventional MPA rectenna is shown in Fig. 2.11. The simulated harvested power vs spatial angle (ϕ) and measured η vs P_{rx} pattern are shown in Fig. 2.12.

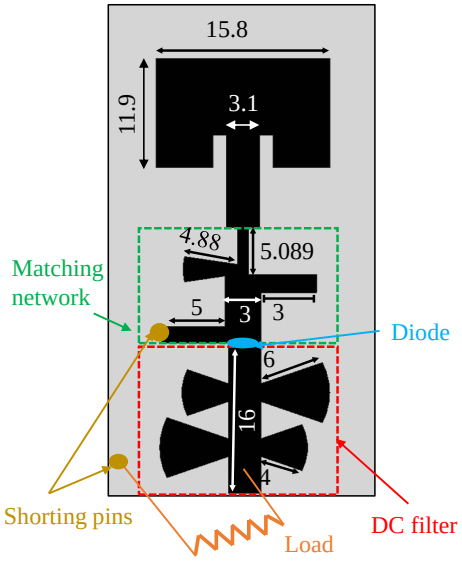

Figure 2.11: Complete layout of the conventional WPT system.

The simulated half-power beam width and harvested DC voltage of a conventional rectenna system are 45° and 600 mV, respectively. The various DC combining topologies are discussed in section 2.3.3.

2.3.3 DC Combining Technique

The angular misalignment is mitigated using a multi-sector rectenna array combined with RF and DC combining techniques to harvest DC power, as shown in Fig. 2.13 (reproduced from [39]). The RF combining technique utilizes an RF combiner to capture RF power

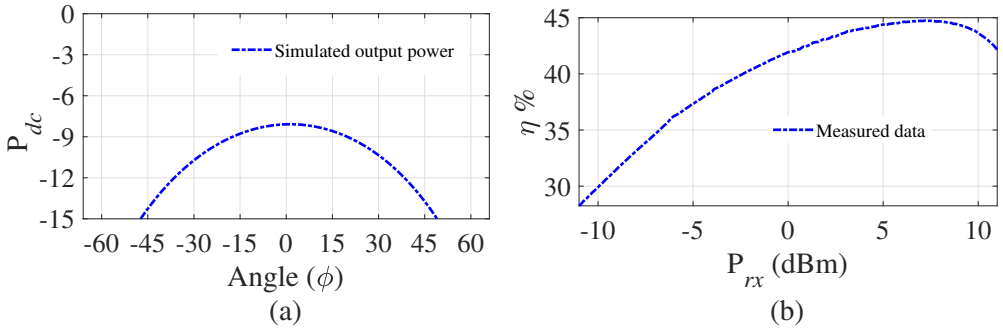

Figure 2.12: (a) Simulated DC power pattern (b) measured η of the conventional WPT system.

using various antenna elements (a phasor summation of RF waves), which is fed to a single rectifier circuit [39]. Therefore, the radiation beam pattern becomes narrow (uniform array concept) with the increase in the number of antenna elements combined using RF combining [126, 127] circuits. On the other hand, the DC combining technique [128] uses an individual rectifier circuit for each antenna element, and there is no phasor summation of RF. Therefore, the beamwidth remains the same as the individual element, resulting in a wider beamwidth as compared to the RF combining. Thus, a DC combining technique is used to design a multi-sector rectenna for mitigating angular misalignment. A hybrid combining technique can increase the beamwidth while achieving higher DC power, as illustrated in Fig. 2.13. The normalized DC power of the reported combining techniques is shown in Fig. 2.14(reproduced from [39]). The subarray-based structure is recommended for DC combining as it provides more DC power with a wider beamwidth. However, these complex strategies are challenging to implement in practice. Therefore, this thesis adopts a simple DC combining technique that is easily implementable without complex structures.

2.3.4 Power management unit

Power management units (PMUs) are essential components in energy harvesting systems, managing the flow of energy between the energy source and the energy storage element. PMUs are especially important in systems with multiple energy sources and outputs. Energy harvesting systems often use various energy sources, such as RF, solar, thermal, and mechanical energy, each with different voltage and current characteristics. Thus, it is necessary to convert and manage the energy to make it suitable for charging batteries or powering electronic devices. PMUs are designed to manage multiple energy sources and outputs by performing various functions, including voltage regulation, maximum power point tracking (MPPT), and energy storage management. These functions ensure that the energy from multiple sources is used efficiently and that the output power is stable and reliable. PMUs can prioritize energy sources based on their characteristics and availability. For instance, if the system has a solar panel and a RF energy harvester, the PMU can prioritize the solar panel and RF harvester during the day when the solar energy is available and only RF energy harvester at night when the solar energy is not available. PMUs can

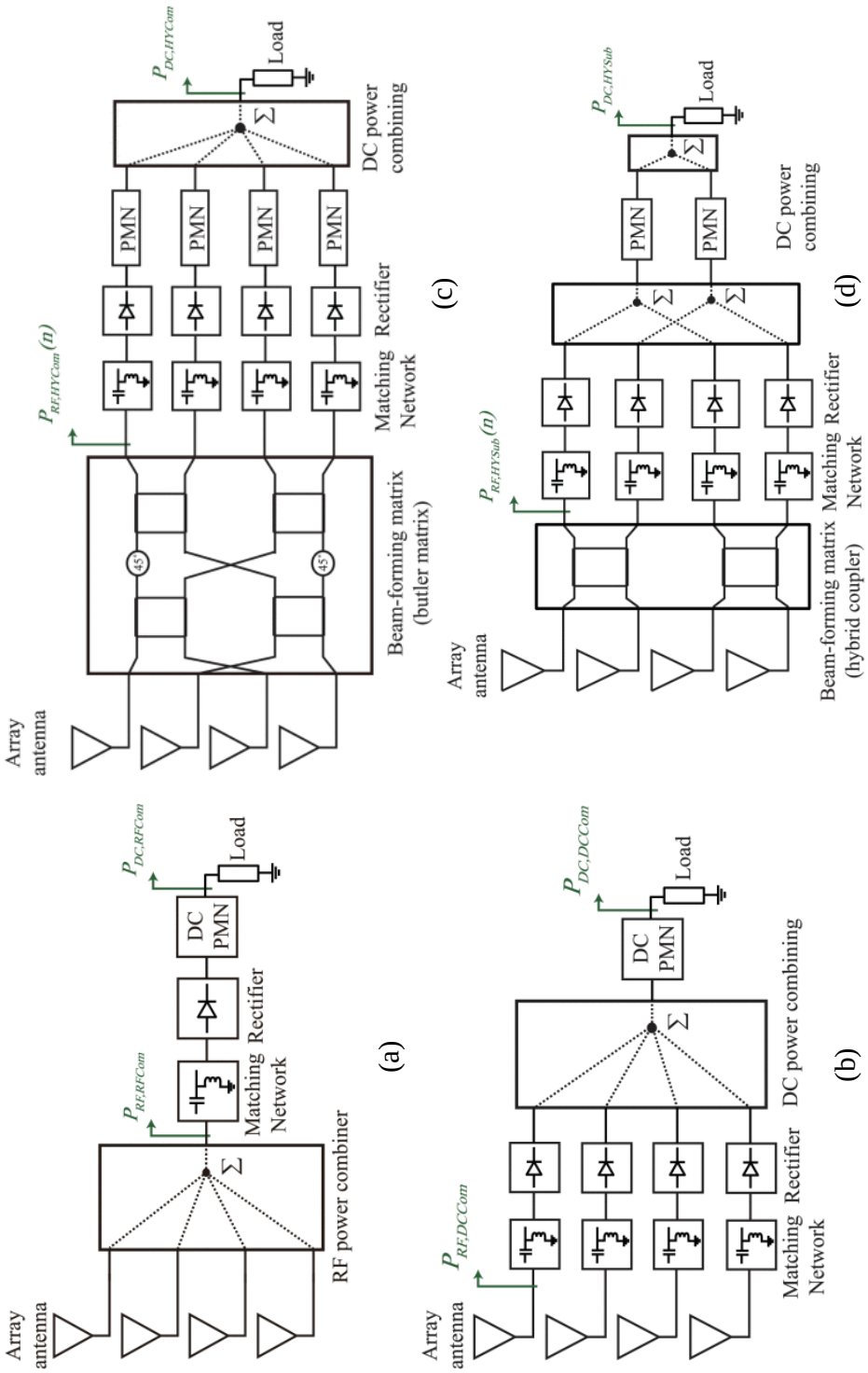

Figure 2.13: (a) RF power combining (b) DC power combining (c) hybrid power combining and (d) hybrid power combining subarray.

also handle multiple energy outputs by providing separate power paths for each output. This can be achieved by using a multi-port PMU with separate input and output ports for each energy source and output. Alternatively, a single-port PMU can be used with a power splitter or power combiner to distribute the power to multiple outputs. In summary, PMUs are crucial for efficient energy management in systems with multiple energy sources

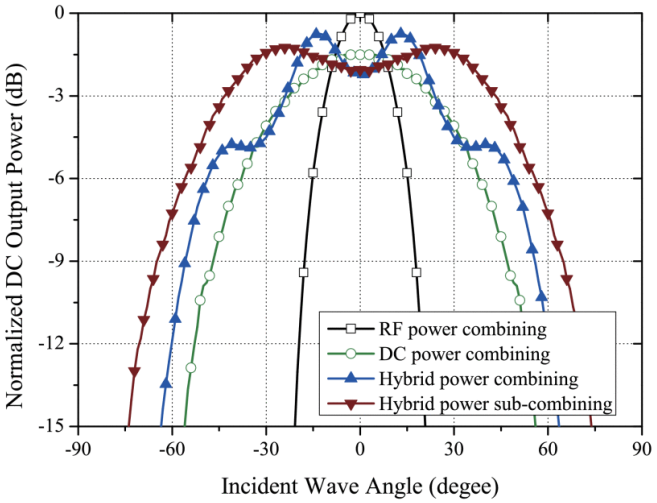

Figure 2.14: Various combining techniques with incident wave angle.

and outputs, ensuring reliable and stable output power. As a limitation, the PMU adds to the cost of the overall system and also increases the system's dimensions, making the WPT system bulky. Moreover, this results in a slightly lower harvesting efficiency due to internal parasitic losses present in the capacitor and surface mount device (SMD) components.

2.3.5 Multisector rectenna array

The application scenario to mitigate the angular misalignment is shown in Fig. 2.15.

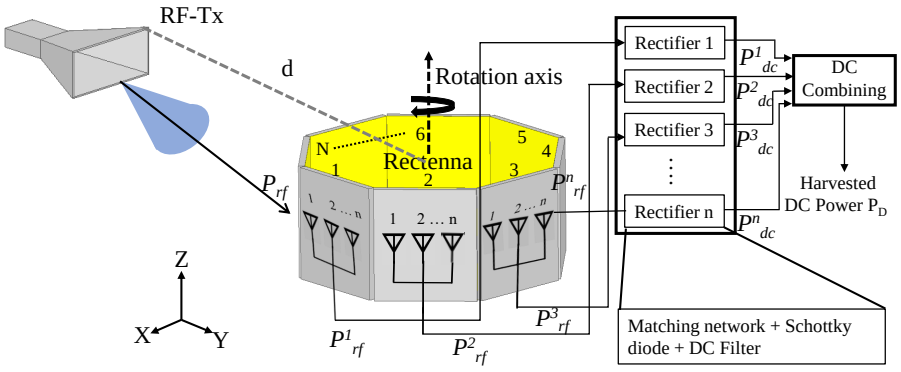

Figure 2.15: Multi-sector rectenna array of the conventional WPT system.

The N number of sectors with layout of single patch antenna are shown in Fig. 2.16. The simulated P_D pattern of the conventional antenna is demonstrated for various N in Fig. 2.17 to mitigate the angular misalignment. The results show that $N = 8$ sectors are sufficient to achieve a uniform $P_D(\phi)$ and completely mitigate the angular misalignment. The experimental validation of the conventional design are described in the section 2.3.6.

2.3.6 Measurement and Results

The multi-sector fabricated prototype and measurement setup of the proposed WPT rectenna system is shown in Fig 2.18. The conventional rectenna elements are integrated

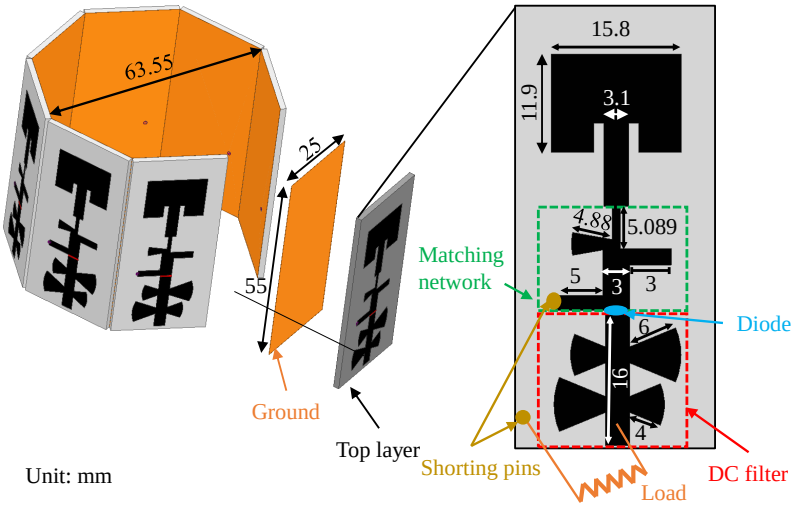

Figure 2.16: Multi-sector rectenna array of the conventional WPT system.

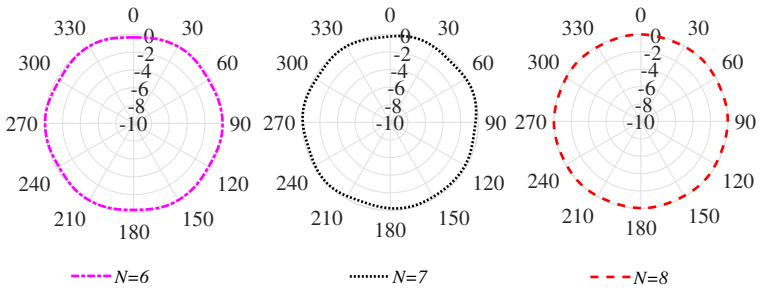

Figure 2.17: Simulated P_D pattern of the conventional WPT system for (a) N = 6 (b) N = 7 and (c) N = 8 sectors.

in the azimuth to cover 360° to build five prototypes with $N = 4, 5, 6, 7, 8$ sectors to verify the simulation results. The DC power received from individual sectors is integrated using series DC combining technique. An optimum load of 2010 Ω is employed to harvest a maximum P_{dc} calculated for a single rectenna. Whereas, for the conventional WPT designs, the optimum loads used 16080 Ω, respectively. In the measurement setup of Fig 2.18, a Tx antenna having 8.6 dBi gain is installed at 100 cm distance from the WPT node. The Tx is fed using a RF signal generator (Agilent Technologies E8257D) set at 25 dBm output power level [129]. The maximum power transfer range is limited by the frequency of operation, EIRP of the RF shower, and rectifier circuit sensitivity governed by Schottky diode. For a given WPT system, a higher range can be obtained by allowing higher EIRP values for RF showers as per the application requirements. For instance, in the outdoor application scenarios where biological interventions are less likely as compared to the indoor, EIRP of as high as 53 dBm[130] have also been used. Whereas, for the other applications, exposure is constrained by limiting EIRP value for a maximum allowed SAR, e.g., 1.6 W/Kg, from the FCC guidelines. The conventional system is measured for designs with $N = 4 - 8$ sectors and the DC patterns are shown in Fig 2.19. The measured results indicate that the conventional WPT system has dips in the P_D patterns for the designs with $N = 4 - 7$. The P_D pattern is uniform for $N = 8$ design, as shown in

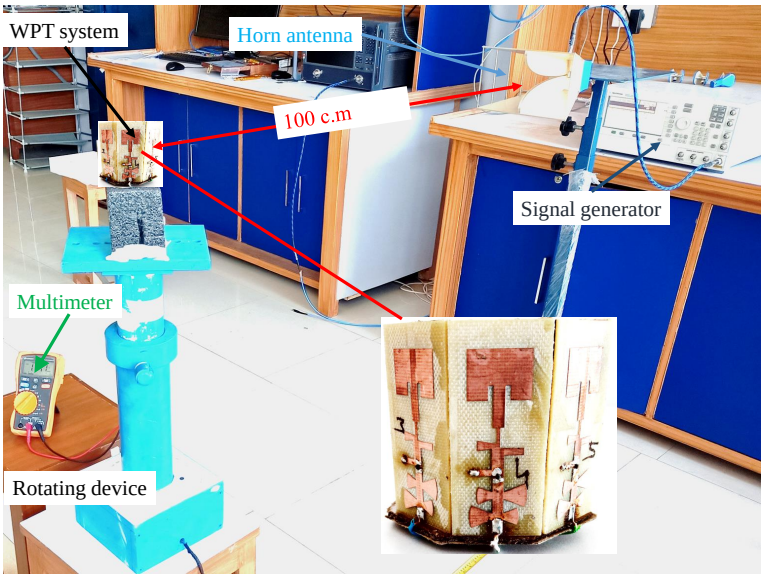

Figure 2.18: The fabricated prototype of the conventional WPT node and measurement setup.

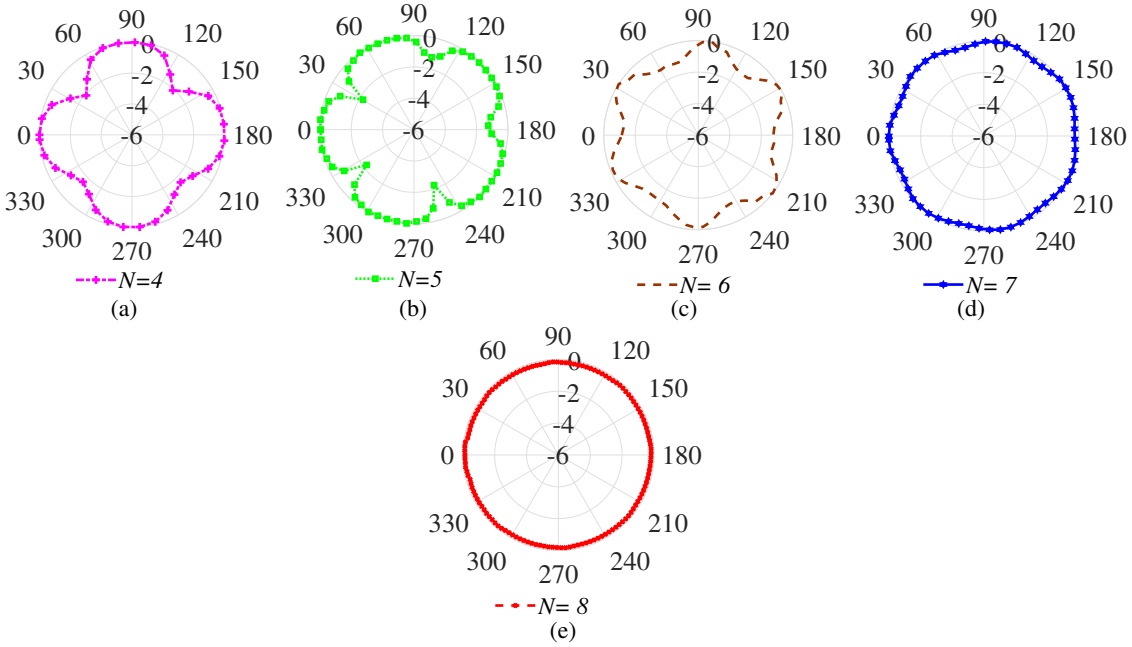

Figure 2.19: Measured P_D of the conventional WPT system with single element for (a) $N = 4$ (b) $N = 5$ (c) $N = 6$ (d) $N = 7$, and (e) $N = 8$ sectors.

Fig 2.19 (e), indicating the optimal sectors required to mitigate the angular misalignment problem by the conventional patch antenna. The measured open DC voltage readings of the conventional single rectenna and multi-sector WPT systems are 550 and 1148 mV, respectively, and the conventional single rectenna offers 65 % PCE at -10 dBm. The complete multi-sector rectenna system offers low voltage because of the single RF source, which illuminates only a few sectors non-uniformly in the conventional WPT system, as depicted in Fig. 2.15. Therefore, the performance of the direct series dc combining is degraded due to unexcited rectennas, which do not face the Tx and serve as dead loads [44].

The performance of the multi-sector rectenna array can be enhanced using a multi-source technique that illuminates all the sectors simultaneously or utilizes a smart network, which is discussed in Chapter 3.

2.4 Summary

In this chapter, the basic building blocks of the WPT rectenna are discussed to design a complete conventional WPT rectenna. Further, the simulated DC beamwidth is analyzed to mitigate the angular misalignment. The single-sector DC beamwidth decides the number of sectors that can later be combined using RF and DC techniques. The complete conventional WPT system performance is investigated experimentally. The complete conventional WPT rectenna has large, 3-D dimensions with low PCE. Therefore, to achieve the optimal number of sector to mitigate the angular misalignment, a mathematical analysis is presented in the Chapter 3.

Chapter 3

Multi-sector Rectenna Array Design for Uniform Azimuth Coverage

3.1 Introduction

The azimuthal angular misalignment occurs when the WPT node rotates with respect to the Tx antenna as discussed in Chapter 1, subsection 1.1.1. The directional radiation pattern of the rotating WPT rectenna is misaligned with the Tx, which reduces the harvested power [8]. Therefore, the WPT nodes need customization to achieve a consistent harvested DC power and high PCE oblivion to their orientations [11, 28, 52]. Moreover, an omnidirectional DC pattern essentially represents complete mitigation of the angular misalignment problem, therefore, efforts are made to customize the WPT antenna with a specific RF pattern that corresponds to the desired DC pattern. Further, this chapter presents a design procedure for an angular misalignment tolerant multi-sector rectenna array used as a WPT system.
The main content of this chapter are the following:

- An analytical framework to synthesize an optimal DC pattern of rectenna element is presented for the multi-sector WPT nodes.
- The conditions on radiation pattern characteristics of a single sector rectenna are derived to determine the optimal number of sectors required to achieve omnidirectional coverage with miniaturization.
- The 3D and planar designs (H1A1, H1A2, and H1A3) are presented to mitigate the azimuth angular misalignment and offer a compact footprint with high PCE compared to the state-of-the-art designs.

The main content related to objective H1 is presented in this chapter in Section 3.2.

3.2 H1: Analytical framework to mitigate the azimuth angular misalignment

To analyze the effect of angular misalignment problem, the DC pattern of a multi-sector WPT node is analytically modeled. The schematic diagram of a 3-D WPT node composing of a rectenna array with n elements arranged to form a multi-sector structure with number of sectors N is depicted in Fig. 3.1. Each sector houses one rectenna element composed of a receiving antenna, matching network, rectifier with Schottky diode, followed by a common

DC combining circuit and a load. To shape the RF patterns of the sectors, a linear array of n elements is considered as the receiving antenna in each sector. A dedicated RF Tx is assumed situated in the azimuth plane at a distance d from the WPT node. The antennas

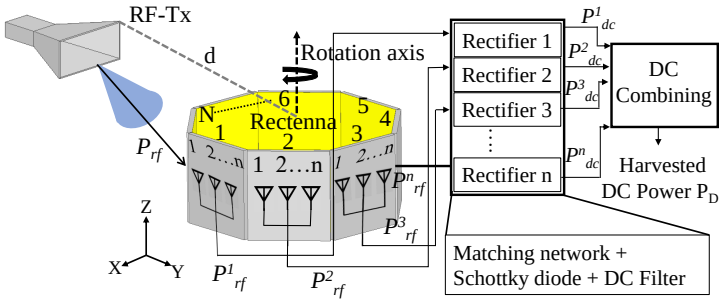

Figure 3.1: Schematic diagram of the considered WPT system.

of the sectors oriented in particular directions capture the RF signal powers, P^i_{rf}, which are individually rectified to DC signals, P^i_{DC}, and combined to produce the total harvested DC power, P_D, as shown in Fig. 3.1. When the node rotates, the P_D level varies with the node orientation ϕ due to directional received RF power pattern $P_{rf}(\phi)$ of each sector antenna followed by the non-linear rectification to $P_{DC}(\phi)$ and then DC combining of rectenna array. Ideally, the DC pattern $P_D(\phi)$ of the WPT node should be independent of ϕ to mitigate the angular misalignment problem. To realize the significance of this angular dependency, $P_{rf}(\phi)$, $P_{DC}(\phi)$, and $P_D(\phi)$ are analytically modelled.

3.2.1 Analysis of the DC pattern under misalignment

The total DC power $P_D(\phi)$ of the misaligned WPT node is analyzed by formulating the power $P_{DC}(\phi)$ harvested by the individual rectenna. For analysis, the geometrical model of the WPT node under misalignment by ϕ angle is depicted in Fig. 3.2. The node is

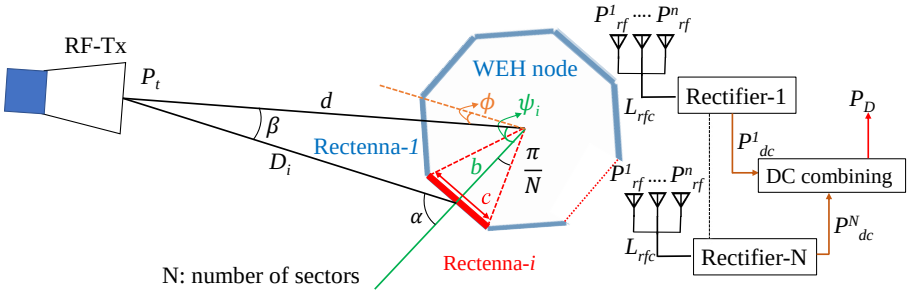

Figure 3.2: Geometrical model of the WPT node under angular misalignment.

assumed in perfect alignment for $\phi = 0$ when the rectenna-1 sector edge is perfectly aligned with the Tx antenna. Under node misalignment, the RF power, $P^i_{rf}(\phi)$, received by the antenna belonging to rectenna-i $\forall\ i \in \{1, 2, ...N\}$ is converted to DC power $P^i_{DC}(\phi)$ and contributes to the total $P_D(\phi)$. As apparent from Fig. 3.2, the placement of the antennas exhibits angular symmetry, therefore, the rectenna-i captures the RF power in accordance to its sector's actual orientation ψ_i. However, since the rectenna centers do not

coincide with the node center (origin) due to multi-sector structure, the pattern $P^i_{rf}(\phi)$ is not directly realizable from the receiver antenna gain pattern, $G_r(\alpha)$, which is defined with respect to the local coordinates of the rectenna elements. Similarly, the Tx antenna gain with pattern, $G_t(\beta)$, varies with the sector location at a distance D_i in a given direction β which is defined in the Tx antenna local coordinate system in Fig. 3.2. Therefore, geometrical transformations are required to establish relationships between ϕ, α, β, and D_i. The parameters are defined in Fig. 3.2 and evaluated in terms of known parameters, N, ϕ, and d, as

$$\alpha = \beta + \psi_i, \qquad \beta = \tan^{-1}\left(\frac{b\sin\psi_i}{d - b\cos\psi_i}\right) \tag{3.1a}$$

$$D_i = \frac{b \times \sin(\psi_i)}{\sin(\beta)} \qquad \psi_i = \frac{\pi}{N}(2i-1) - \phi \tag{3.1b}$$

$$b = \frac{0.5 \times c}{\tan\frac{\pi}{N}}, \quad \text{and} \quad c = (n-1)\frac{\lambda_0}{2} + w + 12h \tag{3.1c}$$

where, b is the perpendicular distance of the sector from the origin, c is the size of a sector, w is the width of a single antenna element, and h is the substrate height of the antenna.

The received RF power by the rectenna-i is evaluated using Friss transmission equation as

$$P^i_{rf}(\phi) = \frac{P_t G_t(\beta) G_r(\alpha) \lambda^2}{(4\pi D_i)^2} \tag{3.2}$$

where, P_t is the transmitted power of the RF Tx and λ is the wavelength at operating frequency f_0. The parameters $G_t(\beta)$, $G_r(\alpha)$, and D_i are evaluated through geometrical transformation relations using (3.1). The RF power $P^i_{rf}(\phi)$ received by the rectenna-i is transformed into DC power $P^i_{DC}(\phi)$ with rectification efficiency $\eta^i(\phi)$ as

$$P^i_{DC}(\phi) = \eta^i(\phi) P^i_{rf}(\phi) \tag{3.3}$$

Here, since $\eta^i(\phi)$ varies proportionally with $P^i_{rf}(\phi)$, it is a function of misalignment ϕ and also depends on the electrical characteristics of the Schottky diode [13], which is mathematically expressed as

$$\eta^i(\phi) = P^i_{rf}(\phi) \times \left(\frac{\eta_{MN} \Re_I \sqrt{R_j}}{2 + 8\pi^2 f_0^2 R_j R_s}\right)^2 \tag{3.4}$$

Where, $\Re_I$ is the current responsivity, η_{MN} is the matching network losses, R_s is the series resistance, and R_j is the non-linear junction resistance of the Schottky diode. Based on 3.4, it can be observed that efficiency is directly proportional to the input RF power.

All the exposed rectennas capture the RF power in accordance to their sector's actual orientation ψ_i. However, due to structural angular symmetry and identical rectenna circuits, the $P^i_{DC}(\phi)$ pattern of the rectenna-i can be written in terms of angular shifted

versions of the general rectenna DC pattern (denoted as $P_{DC}(\phi)$) as

$$P^{i}_{DC}(\phi) = P_{DC}\left(\phi - \frac{\pi}{N}(2i-1)\right), \tag{3.5}$$

For instance, $P^{1}_{DC}(\phi) = P_{DC}(\phi - \frac{\pi}{N})$ is the DC pattern of the rectenna-1 with respect to the node misalignment ϕ. The $P_{DC}(\phi)$ is formulated by substitutions from (3.3)-(3.5) and expressed as

$$P_{DC}(\phi) = \left(\frac{\eta_{MN}\Re_I\sqrt{R_j}}{2+8\pi^2 f_0^2 R_j R_s} \times P^{1}_{rf}\left(\phi - \frac{\pi}{N}\right)\right)^2 \tag{3.6}$$

which by using (3.2) and (3.6) is obtained as

$$\begin{aligned} P_{DC}(\phi) &= \left(\frac{\eta_{MN}\Re_I\sqrt{R_j}}{2+8\pi^2 f_0^2 R_j R_s} \times \frac{P_t G_t(\beta_1) G_r(\alpha_1)\lambda^2 \sin^2(\beta_1)}{(4\pi b\sin(\phi))^2}\right)^2 \\ &\text{where } \beta_1 = \tan^{-1}\left(\frac{b\sin\phi}{b\cos\phi - d}\right), \text{and } \alpha_1 = \beta_1 + \frac{\pi}{N} - \phi \end{aligned} \tag{3.7}$$

The total harvested DC power P_D is the combination of $P^{i}_{DC}\ \forall\ i \in \{1, 2, ...N\}$ and evaluated as

$$P_D(\phi) = \sum_{i=1}^{N} P_{DC}\left(\phi - \frac{\pi}{N}(2i-1)\right) \cdot (1 - L_{DCc}) \tag{3.8}$$

where, L_{DCc} represents the combining loss of the N-element DC combiner circuit. To note that if the rectennas of the multi sectors are identical, it is sufficient to formulate and synthesize only the P_{DC} pattern of a single sector to obtain the total pattern P_D of the WPT node.

3.2.2 Omnidirectional $P_D(\phi)$ as Design Objective to Mitigate Angular Misalignment

In this section, the misalignment problem persisting in the conventional designs is illustrated for two multi-sector WPT systems ($N = 4$ and $N = 6$) having single patch antenna element per sector ($n = 1$). The patterns are analytically calculated using (3.7) by taking into account the actual performance parameters of the conventional patch antenna gain (5 dBi), matching network efficiency ($\eta_{MN} = 1$), Tx antenna gain (8.6 dBi), and Schottky diode parameters (SMS-7630 – 09LF). The analyzed $P_D(\phi)$ patterns for the two cases are depicted in Fig. 3.3. The plots demonstrate the variations in $P_D(\phi)$ with the orientation of the WPT node. Particularly towards the sector edge directions, significant dips in the patterns are evident, which form due to the limited beamwidth of the DC power pattern $P_{DC}(\phi)$ of a single sector for both the cases. This illustrates the angular misalignment problem persisting in the designs where the RF and DC patterns of the multi-sector design are not optimized to achieve constant P_D with respect to the node misalignment ϕ. This is similarly evident in the multi-sector designs available in the literature, where the harvested DC Power varies with the orientation of the WPT

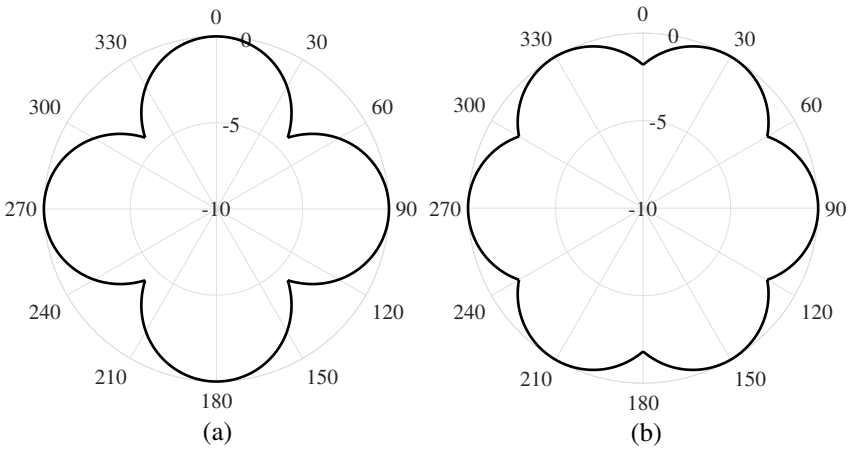

Figure 3.3: Angular misalignment in (a) 4-sector and (b) 6-sector WPT node.

node. This motivates this study to present an analytical framework for analysis and optimization of multi-sector WPT nodes by adopting an omnidirectional $P_D(\phi)$ as the design objective to completely mitigate the angular misalignment problem. The presented analytical study synthesizes the $P_{DC}(\phi)$ pattern and determines the appropriate number of sectors necessary to accomplish the design objective.

3.2.3 A Closed-form Solution for $P_{DC}(\phi)$ Pattern Synthesis

To analytically obtain the target omni-directional $P_D(\phi)$ pattern, the reverse problem of (3.8) is first formulated to synthesize the $P_{DC}(\phi)$ pattern as a closed-form solution of any general $P_D(\phi)$ objective. In this regard, the normalized $P_D(\phi)$ in (3.8) can be equivalently expressed as the convolution $(*)$ of normalized $P_{DC}(\phi)$ with train of Dirac delta function (δ) written by

$$P_D(\phi) = P_{DC}(\phi) * \sum_{i=1}^{N} \delta\left(\phi - \frac{\pi}{N}(2i-1)\right) \tag{3.9}$$

By exerting the Fourier Transform (FT) on both the sides of (3.9) followed by the use of convolution property $\mathrm{FT}[A * B] = \mathrm{FT}[A] \cdot \mathrm{FT}[B]$ gives

$$\mathrm{FT}\left[P_D(\phi)\right] = \mathrm{FT}\left[P_{DC}(\phi)\right] \cdot \mathrm{FT}\left[\sum_{i=1}^{N} \delta\left(\phi - \frac{\pi}{N}(2i-1)\right)\right] \tag{3.10}$$

Further manipulations on (3.10) are conducted to derive the $P_{DC}(\phi)$ as

$$\begin{aligned} \mathrm{FT}\left[P_{DC}(\phi)\right] &= \frac{\mathrm{FT}\left[P_D(\phi)\right]}{\mathrm{FT}\left[\sum_{i=1}^{N} \delta\left(\phi - \frac{\pi}{N}(2i-1)\right)\right]} \\ \Rightarrow P_{DC}(\phi) &= \mathrm{IFT}\left[\frac{\mathrm{FT}\left[P_D(\phi)\right]}{\mathrm{FT}\left[\sum_{i=1}^{N} \delta\left(\phi - \frac{\pi}{N}(2i-1)\right)\right]}\right] \end{aligned} \tag{3.11}$$

where $\mathrm{IFT}[\cdot]$ denotes the inverse of FT operation. The relation,

$$\mathrm{FT}\left[\sum_{i=1}^{N} \delta\left(\phi - \frac{\pi}{N}(2i-1)\right)\right] = e^{-j\omega_\phi \pi} N \frac{sinc\left(\omega_\phi\right)}{sinc\left(\frac{\omega_\phi}{N}\right)}, \tag{3.12}$$

is used in (3.11) to obtain

$$P_{DC}(\phi) = \text{IFT}\left[\frac{\text{FT}\left[P_D(\phi)\right] \cdot sinc\left(\frac{\omega_\phi}{N}\right)}{e^{-j\omega_\phi \pi} N sinc\left(\omega_\phi\right)}\right] \tag{3.13}$$

Here, ω_ϕ represents the angular frequency domain corresponding to the ϕ dimension. The expression in (3.13) represents the closed-form solution of $P_{DC}(\phi)$ pattern that is synthesized to achieve any predefined objective $P_D(\phi)$ pattern.

3.2.4 Synthesizing $P_{DC}(\phi)$ for an Ideal $P_D(\phi)$ Objective

To completely mitigate the angular misalignment problem, an ideal omnidirectional $P_D^o(\phi)$ as objective function is mathematically defined as

$$P_D^o(\phi) = rect\left(\frac{\phi - \pi}{2\pi}\right) = \begin{cases} 1 & 0 \leq \phi \leq 2\pi \\ 0 & \text{otherwise} \end{cases} \tag{3.14}$$

The optimal $P_{DC}(\phi)$ solution to achieve this objective function is evaluated by substituting (3.14) in (3.13) to obtain

$$P_{DC}(\phi) = \text{IFT}\left[\frac{\text{FT}\left[rect\left(\frac{\phi-\pi}{2\pi}\right)\right] sinc\left(\frac{\omega_\phi}{N}\right)}{e^{-j\omega_\phi \pi} N sinc(\omega_\phi)}\right] \tag{3.15}$$

Since $FT\left[rect\left(\frac{\phi-\pi}{2\pi}\right)\right] = 2\pi e^{-j\omega_\phi \pi} sinc(\pi\omega_\phi)$, the closed form solution of (3.15) is obtained as

$$\begin{aligned} P_{DC}(\phi) &= \text{IFT}\left[\frac{2\pi e^{-j\omega_\phi \pi} sinc(\pi\omega_\phi) sinc\left(\frac{\omega_\phi}{N}\right)}{e^{-j\omega_\phi \pi} N sinc\left(\omega_\phi\right)}\right] \\ &= \text{IFT}\left[\frac{2\pi}{N} sinc\left(\frac{\omega_\phi}{N}\right)\right] \\ \Rightarrow P_{DC}(\phi) &= rect\left(\frac{N\phi}{2\pi}\right) \end{aligned} \tag{3.16}$$

The $P_{DC}(\phi)$ solution of (3.16) obtained for the ideal objective $P_D^o(\phi)$ represents a uniform DC pattern (flat-beam) covering the range $-\frac{\pi}{N} \leq \phi \leq \frac{\pi}{N}$, thus, having a Flat-Beam Width $(FBW) = \frac{2\pi}{N}$, as an optimal solution for a given N. Conversely, the corresponding optimal N represents a solution for which the relation $N = \frac{2\pi}{FBW}$ is satisfied. For all other possible $P_{DC}(\phi)$ patterns including the flat-beams not following this relation, the $P_D(\phi)$ encounters void or overlap between the $P_{DC}(\phi)$ patterns of the adjacent rectennas, as visualized in Fig. 3.4. The $FBW = \frac{2\pi}{N}$ in Fig. 3.4 (b) results in the optimal solution of omnidirectional $P_D(\phi)$ to mitigate the angular misalignment problem. Whereas, the voids are apparent for $FBW < \frac{2\pi}{N}$ in Fig. 3.4 (a) and overlapping for $FBW > \frac{2\pi}{N}$ in Fig. 3.4 (c), the both cases are unable to achieve the desired omnidirectional $P_D^o(\phi)$ pattern. Ideally, the $P_{DC}^i(\phi)$ patterns of the multiple sectors should adopt to the optimal flat-beam shape with $FBW = \frac{2\pi}{N}$, however, it is not practically feasible to design a rectenna which can strictly achieve such stringent pattern requirement for a given N. In general, the rectennas have more wider DC patterns also containing side-lobes, hence, overlapping can not be avoided.

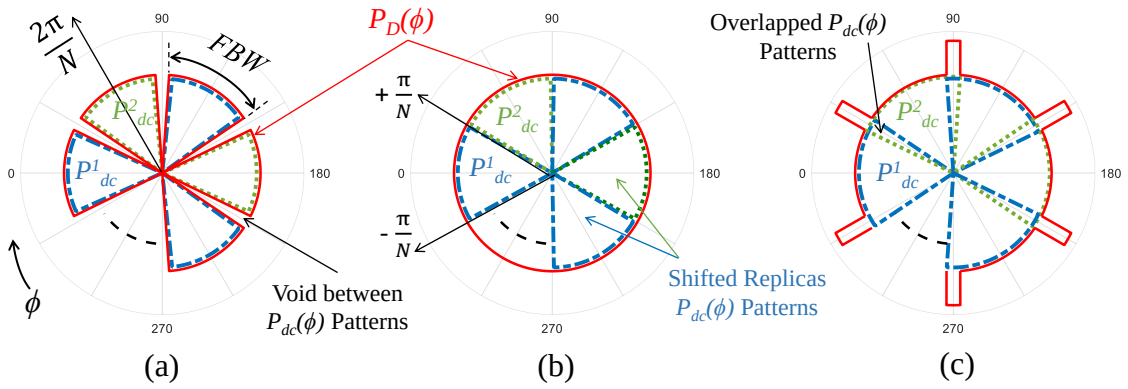

Figure 3.4: Ideal $P_D(\phi)$ patterns for flat-beam $P_{DC}(\phi)$ solution having (a) $FBW < \frac{2\pi}{N}$ (b) $FBW = \frac{2\pi}{N}$ (c) $FBW > \frac{2\pi}{N}$.

Therefore, to synthesize a practically feasible $P_{DC}(\phi)$ pattern with gradual shaping and allowed overlapping, a realistic $P_D(\phi)$ objective function is essential to be defined.

3.2.5 Synthesizing $P_{DC}(\phi)$ for a realistic $P_D(\phi)$ Objective

The realistic objective DC pattern, $P_D^r(\phi)$, is mathematically defined to synthesize a practically feasible $P_{DC}(\phi)$ solution. For that, the $P_D^r(\phi)$ function is set uniform in the range $\eta \leq \phi \leq (2\pi - \eta)$ and a roll-off region with angular expansion of 2η units as depicted in Fig. 3.5 (a) is included in the definition. Here, the omnidirectional feature of

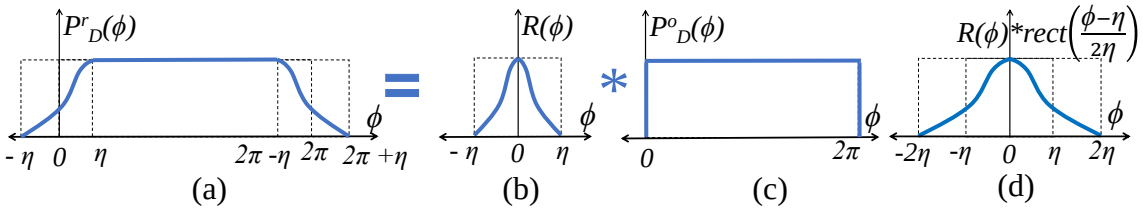

Figure 3.5: (a) Realistic $P_D^r(\phi)$ objective function (b) roll-off forming function $R(\phi)$ (c) ideal uniform objective $P_D^o(\phi)$ (d) actual roll-off function.

the P_D objective persists due to its periodicity and symmetry at $\phi = 2\pi$ and ensured by considering the overlapping of the regions $-\eta \leq \phi \leq \eta$ and $(2\pi - \eta) \leq \phi \leq (2\pi + \eta)$ to contribute to a uniform DC pattern identical to the P_D^o. The roll-off region is incorporated by introducing a roll-off forming function (for mathematical convenience), $R(\phi)$, as depicted in Fig. 3.5 (b), defined in the range $[-\eta, \eta]$ as an arbitrary even function with unit area and properties defined by

$$\begin{aligned} &R(\phi) = 0 \;\; \forall \;\; \phi \in (-\infty, \eta)\,\&\,(\eta, \infty)\,, \quad R(\phi) = R(-\phi), \\ &\text{and} \quad \int_{-\infty}^{\infty} R(\phi)d\phi = \int_{-\eta}^{\eta} R(\phi)d\phi = 1 \end{aligned} \tag{3.17}$$

The $R(\phi)$ is defined such that its convolution with uniform $P_D^o(\phi)$ inserts roll-off region in $P_D^o(\phi)$ to equate to the $P_D^r(\phi)$ as illustrated in Fig. 3.5 (a-c). The realistic objective function $P_D^r(\phi)$ is thus defined as

$$P_D^r(\phi) = R(\phi) * P_D^o(\phi) \tag{3.18}$$

which, by using (3.14) and (3.17), expended to (Fig. 3.5 (a))

$$P_D^r(\phi) = \begin{cases} 0 & -\infty < \phi \leq -\eta \\ R(\phi-\eta) * rect\left(\frac{\phi-\eta}{2\eta}\right) & -\eta < \phi \leq \eta \\ 1 & \eta < \phi \leq (2\pi-\eta) \\ R(\phi-2\pi+\eta) * rect\left(\frac{\phi-2\pi+\eta}{2\eta}\right) & (2\pi-\eta) < \phi \leq (2\pi+\eta) \\ 0 & (2\pi+\eta) < \phi < +\infty \end{cases} \tag{3.19}$$

Here, the term $R(\phi) * rect\left(\frac{\phi}{2\eta}\right)$ is an even function with range $\phi \in [-2\eta, 2\eta]$ as depicted in Fig. 3.5 (d) which represents the actual roll-off region shaped in $P_D^r(\phi)$. The $P_D^r(\phi)$ from (3.18) is substituted in (3.13) to synthesize optimal $P_{DC}(\phi)$ achieving the objective (3.19), this gives

$$\begin{aligned} P_{DC}(\phi) &= \text{IFT}\left[\frac{\text{FT}\left[R(\phi) * P_D^o(\phi)\right] \cdot sinc\left(\frac{\omega_\phi}{N}\right)}{e^{-j\omega_\phi \pi} N sinc\left(\omega_\phi\right)}\right] \\ &= \text{IFT}\left[\frac{\text{FT}\left[R(\phi)\right] \cdot \text{FT}\left[P_D^o(\phi)\right] \cdot sinc\left(\frac{\omega_\phi}{N}\right)}{e^{-j\omega_\phi \pi} N sinc\left(\omega_\phi\right)}\right] \\ &= \text{IFT}\left[\frac{\text{FT}\left[R(\phi)\right] \cdot \text{FT}\left[rect\left(\frac{\phi-\pi}{2\pi}\right)\right] \cdot sinc\left(\frac{\omega_\phi}{N}\right)}{e^{-j\omega_\phi \pi} N sinc\left(\omega_\phi\right)}\right] \text{(by using (3.14))} \\ &= \text{IFT}\left[\text{FT}\left[R(\phi)\right] \cdot \frac{2\pi}{N} sinc\left(\frac{\omega_\phi}{N}\right)\right] \qquad \text{(by using (3.15) \& (3.16))} \\ &= \text{IFT}\left[\text{FT}\left[R(\phi)\right] \cdot \text{FT}\left[rect\left(\frac{N\phi}{2\pi}\right)\right]\right] \qquad \text{(by using (3.16))} \\ &= \text{IFT}\left[\text{FT}\left[R(\phi) * rect\left(\frac{N\phi}{2\pi}\right)\right]\right] \text{(using FT}[A * B] = \text{FT}[A] \cdot \text{FT}[B]) \end{aligned}$$

$$\implies P_{DC}^{opt}(\phi) = R(\phi) * rect\left(\frac{N\phi}{2\pi}\right) \tag{3.20}$$

The $P_{DC}^{opt}(\phi)$ derived in (3.20) represents the optimal realistic solution to achieve desired omni-directional $P_D(\phi)$ pattern. To note that, since the $R(\phi)$ can adopt any shape which satisfies the conditions in (3.17), the equivalent conditions are imposed on $P_{DC}^{opt}(\phi)$ by following the convoluted transformation of (3.20). For specifically the rectennas having DC patterns with negligible side-lobe-levels (SLL), the solution (3.20) can be simplified. For such simplified cases, any $P_{DC}(\phi)$ pattern which to be synthesized as an optimal solution in (3.20) must be bounded by the following constraints:

- $P_{DC}^{opt}(\phi)$ is an even function
- $P_{DC}^{opt}(\phi)$ pattern has roll-off region symmetric around $\phi = \pm\frac{\pi}{N}$
- $P_{DC}^{opt}(\phi)$ has a minimum beam extension from $\frac{-\pi}{N}$ to $\frac{\pi}{N}$
- $P_{DC}^{opt}(\phi + \frac{\pi}{N}) + P_{DC}^{opt}(\phi - \frac{\pi}{N}) = 1$, $\forall\phi \in \left[\frac{-\pi}{N}, \frac{\pi}{N}\right]$ must be satisfied when SLL are negligible.

These constraints indicate that to completely mitigate the angular misalignment problem, the harvested DC power pattern of the adjacent sectors should ideally cross over at their 3 dB point. This implies that the RF power patterns of the adjacent sectors should cross over at higher than 3 dB points. Furthermore, the constraints indicate that a receiver antenna with wider beamwidth can reduce the overall size (lower N) of the 3D WPT system. However, generally the increase in beamwidth results in a low antenna gain, which ultimately lowers the peak harvested power. Therefore, besides satisfying the constraint of angular misalignment, the major antenna design challenge is to achieve wider beamwidth without compromising the gain performance.

3.2.6 Outline of the Proposed Design Procedure

The proposed design procedure to mitigate angular misalignment in a multi-sector WPT system has the following steps:

1. Design a novel antenna (or array) for a rectenna element of a sector with symmetrical RF radiation pattern P_{rf}.
2. Evaluate the DC power pattern P_{DC} from P_{rf} of a single sector using (3.7) which accounts for various RF to DC conversion efficiencies.
3. If P_{DC} has significant SLL, execute Step-1-2 to satisfy optimal solution in (3.20), obtain N, and jump to Step-6.
4. If P_{DC} has negligible SLL, execute Step-1-2 to satisfy initial three constraints on P_{DC}.
5. Find number of sectors N for which the forth constraint $P_{DC}(\phi+\frac{\pi}{N}) + P_{DC}(\phi-\frac{\pi}{N}) = 1$, $\forall\phi \in \left[\frac{-\pi}{N}, \frac{\pi}{N}\right]$ is satisfied for the radiation pattern obtained in Step-4.
6. Use P_{DC} patterns to evaluate the total harvested DC pattern P_D.

The optimal N obtained as a result determines the overall size of the designed multi-sector WPT system.

3.2.7 Validation of the Proposed Analytical Framework using Conventional Patch Antenna

The constraints over P_{DC} derived using the proposed analytical framework are validated by considering the patch antenna as an element in the sectors. It is because the patterns and design equations of this type of antenna are mathematically tractable and is evaluated as

$$E_\phi = E_0 \cos v \, \frac{\sin u}{u} \cos\theta \sin\phi \tag{3.21a}$$

$$E_\theta = E_0 \cos v \, \frac{\sin u}{u} \cos\phi \tag{3.21b}$$

$$E(\theta,\phi) = \sqrt{E_\theta^2 + E_\phi^2} \tag{3.21c}$$

$$v = \frac{kl\cos\theta}{2}, \quad u = \frac{kw\sin\theta\sin\phi}{2} \tag{3.21d}$$

where, k is the propagation constant in free space, w is width and l is length of the patch. The $E(\theta,\phi)$ field in the azimuth plane is evaluated by putting $\theta = 90°$. Moreover, the array factor of linear array of patch elements in a sector is given by

$$AF(\theta,\phi) = \sum_{m=1}^{n} \exp\left[jky_m \sin\theta\sin\phi\right] \tag{3.22}$$

The total radiation pattern of the linear array in a single sector can be determined by multiplying $E(\theta,\phi)$ and $AF(\theta,\phi)$ evaluated using (3.21) and (3.22) respectively. Fig. 3.6 demonstrates the analytically evaluated normalized RF and DC power patterns

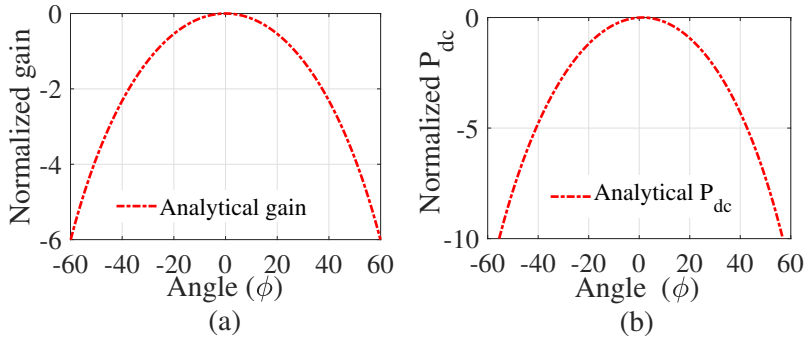

Figure 3.6: Analytical (a) gain and (b) normalized P_{DC} of the conventional patch antenna.

of a conventional patch antenna. According to the constraints to mitigate the angular misalignment, particularly the forth constraint $P_{DC}^{opt}(\phi + \frac{\pi}{N}) + P_{DC}^{opt}(\phi - \frac{\pi}{N}) = 1$, $\forall\phi \in \left[\frac{-\pi}{N}\ \frac{\pi}{N}\right]$ needs to be satisfied by the $P_d(\phi)$ pattern of Fig. 3.6 (b). The other constraints are satisfied due to the symmetric radiation pattern characteristic of the patch antenna. In the condition, $P_{DC}^{opt}(\phi + \frac{\pi}{N})$ represents the Sector-1 P_{DC}, whereas, $P_{DC}^{opt}(\phi - \frac{\pi}{N})$ belongs to the Sector-2 P_{DC}. The optimal solution is obtained where the normalized combined P_{DC} achieves unity in $\phi \in \left[\frac{-\pi}{N}\ \frac{\pi}{N}\right]$. To illustrate the solution, this condition is analyzed for different number of elements ($n = 1,\ 2$) and sectors (N) to achieve optimal P_{DC}. Fig. 3.7 and Fig. 3.8 demonstrate the P_{DC} patterns for $n = 1$ and $n = 2$, respectively. The results indicate that $N = 8$ and $N = 12$ are the optimal number of sectors required to mitigate the angular misalignment in the WPT system, respectively, for $n = 1$ and $n = 2$ patch antenna elements. The results for N lower than optimal value show dip in the total DC pattern whereas N larger than optimal value shows enhanced overlap in the DC pattern. The increase in the number of antenna elements per sector improves the harvesting capability due to increased RF gain. However, the beamwidth becomes narrower, and thus a higher N is required to mitigate the angular misalignment problem; this is evident from the comparison of the $n = 1$ and $n = 2$ plots. Moreover, the higher N and n choices increase the overall size of the WPT system and not suitable for deployment at the miniaturized IoT nodes. For instance, in Fig. 3.7, $N = 8$ is determined as the optimal number of sectors to mitigate the angular misalignment while using conventional

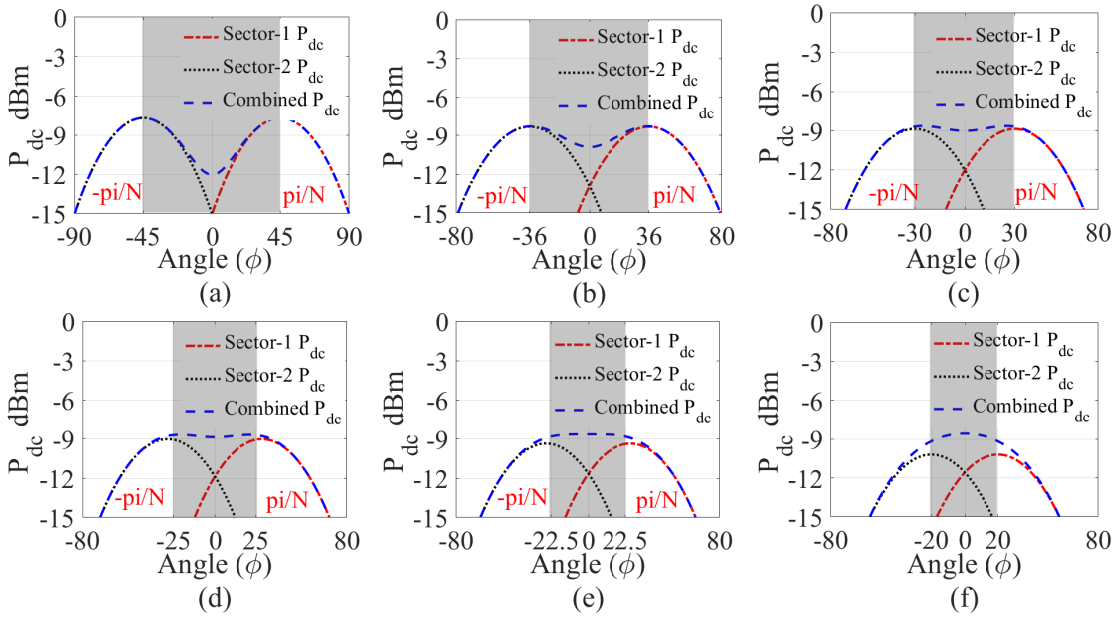

Figure 3.7: Analytical P_{DC} Pattern of WPT system for (a) $N = 4$ (b) $N = 5$ (c) $N = 6$ (d) $N = 7$ (e) $N = 8$, and (f) $N = 9$ sectors each having single patch antenna receiver.

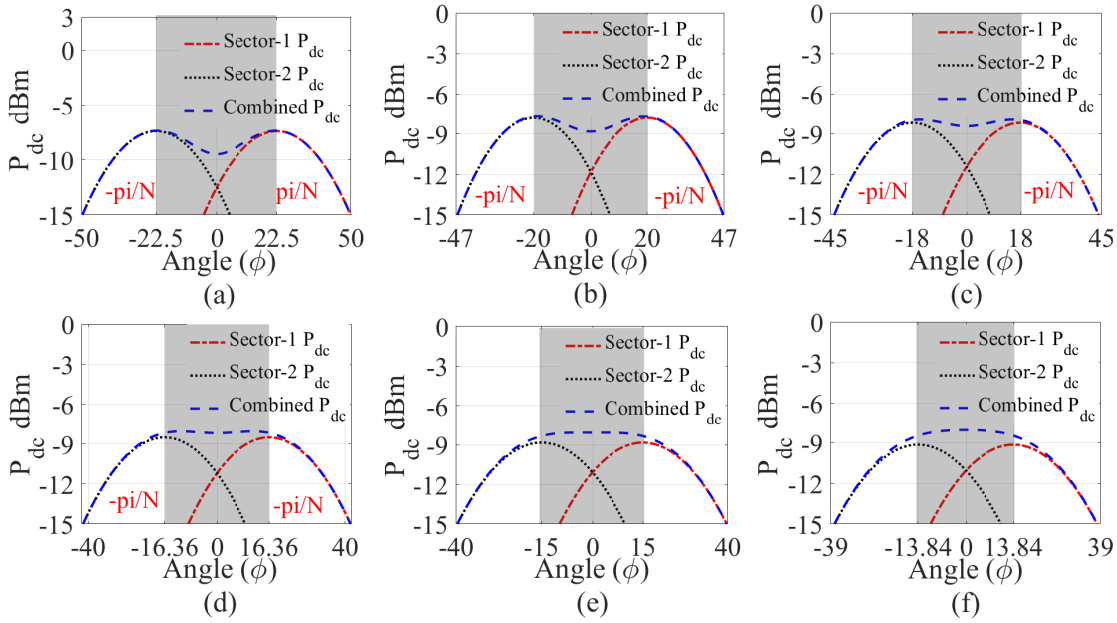

Figure 3.8: Analytical P_{DC} Pattern of WPT system for (a) $N = 8$ (b) $N = 9$ (c) $N = 10$ (d) $N = 11$ (e) $N = 12$, and (f) $N = 13$ sectors each having 2×1 patch antenna array receiver.

patch antenna. Moreover, $N = 12$ is the optimal number of sector for 2×1 conventional patch antenna array. Therefore, the 2×1 WPT system is bulky and causes a higher power loss in DC combining circuits. Therefore, to achieve similar performance to 2×1 WPT system, a new broad-beam high gain antenna is required to reduce the overall size of the WPT system. In addition, the following conditions are observed from the analytical results, to mitigate the azimuthal angular misalignment of the Rx.

- a Wider beam-width antenna can reduce the overall size (lower N) of the WPT system as compared to the conventional patch WPT system.
- The high gain WPT system with the current form factor and beam width (i.e., $N = 8$ equivalent to patch WPT system) can further improve the PCE resulting in an increase in harvested DC power.

The aforementioned conditions can be validated by designing two types of WPT systems. The H1A1 employs a broader beamwidth rectenna system to reduce the system size, whereas H1A2 has a high-gain rectenna system with a beam width similar to the conventional patch rectenna system to collect more RF power to ensure a self-sustaining IoT device without compromising the angular misalignment. A planar rectenna (H1A3) is presented to be easy to install on sensor nodes. A multi-sector rectenna array is presented in section 3.3, which is designed with a new multi-layer broad-beam antenna element.

3.3 H1A1: Broad-beam Multi-sector Rectenna Array Design

The H1A1 WPT system is simulated using Ansys HFSS and Keysight ADS software on a dual sided FR4 substrate ($\epsilon_r = 4.4$, tan$\delta = 0.02$ and thickness 1.565 mm) at 5.8 GHz. The exploded view and dimensional parameters of the H1A1 WPT node is shown in Fig. 3.9. The design evolution of the proposed antenna element and its integration with the rectifier

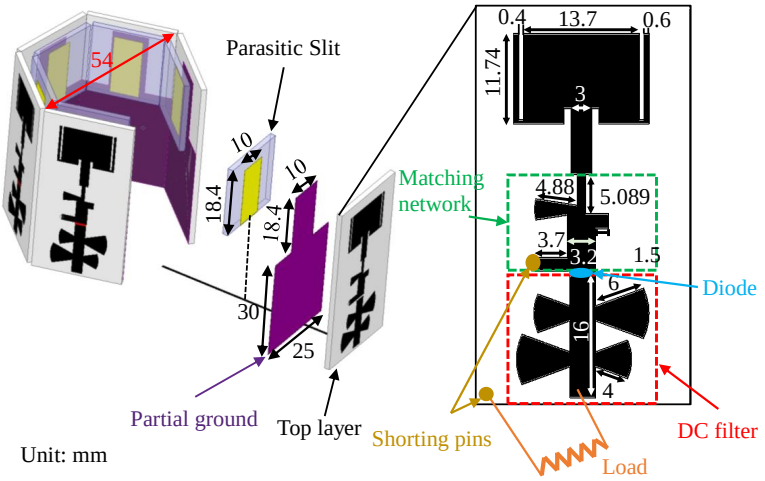

Figure 3.9: Layout of the presented (H1A1) WPT node and exploded view the multi-layer broad-beam antenna element.

circuit is now elaborated.

3.3.1 Evolution of the Multi-layer Broad-beam Antenna Element

The proposed antenna element shown in Fig. 3.9 is evolved from a conventional simple patch antenna having an initial 5 dBi gain and a 3-dB beamwidth of 90° in the azimuth plane. First, the partial ground plane width is optimized to enhance the beamwidth

Table 3.1: Beam width and gain for different sizes of partial ground

	Ground width (mm)	Beamwidth	Gain (dBi)
1	25	90°	5
2	20	104.45°	4.2
3	15	125.56°	4
4	10	136.54°	3.5

as analyzed from the parametric variation result presented in Table 3.1. For instance, the ground plane width (25 mm) of the conventional patch antenna is altered to 10 mm achieving an increased beamwidth of 136.54° but a reduced gain of 3.5 dBi. Essentially, the beamwidth is enhanced at the expense of RF gain, hence, further alteration in the ground plane to achieve larger beamwidth has limited scope. Therefore, next, a third layer is inserted to the structure as a parasitic metallic slit placed 3.4 mm away from the partial ground plane, as depicted in Fig. 3.9. For this, the middle free space present in the multi-sector design is exploited. This results in enhanced antenna gain to 4.6 dBi and reduced beamwidth to 120° which is better than altering only the partial ground plane. In the last, two metallic strips are integrated with the patch on the top layer and optimized to recover the gain to 5 dBi equal to the conventional patch antenna. The final antenna achieves a broad beam of 122° compared to the original value of 90° which supports the reduction of the overall size of the H1A1 WPT system.

3.3.2 Rectenna Design and Integration

The designed antenna is utilized in the rectenna element by integrating with an impedance matching network (IMN) and a half-wave single series (HWSS) diode rectifier to harvest RF power, as shown by the enhanced view of the top layer layout in Fig. 3.9. The HWSS rectifier circuit comprises a low forward voltage Schottky diode (SMS-7630 − 09LF) and a DC filter. The DC low pass filter (DC-LPF) is devised owing to the non-linearity of the RF diode which yields substantial harmonic components. In this design, four radial stubs are tuned to operate as an intercalated fourth-order filter for suppressing the higher-order harmonics to improve the efficiency of the RF rectifier. The impedance of the HWSS circuit is optimized using the LSSP technique in the presence of the DC-LPF. Moreover, an efficient IMN is designed using radial microstrip open and shunt stubs to achieve impedance matching between the antenna and the HWSS circuit, as shown in Fig. 3.9. The antenna and rectifier are matched to 50 Ω by the IMN. The IMN comprises a capacitive radial stub and an inductive rectangular microstrip stub to improve the rectifier matching bandwidth, and the rectangular stub serves as a ground line for the DC component. The rectangular stub is positioned at the diode anode and is based on a thick microstrip line to obtain a high-inductive pattern. The dimensions of the DC-LPF and IMN stubs are optimized jointly to achieve the maximum conversion efficiency. The final dimensions of all the sections of the rectenna element are provided in Fig. 3.9. The optimal number of sectors to mitigate angular misalignment by utilizing the proposed analytical framework

is illustrated.

3.3.3 Multi-sector Design of Rectenna Array

The proposed procedure presented in Section 3.2.6 is now invoked. To constitute Step-1, -2 of the procedure, the simulated P_{rf} and correspondingly evaluated P_{DC} patterns using (3.7) of the proposed rectenna element are plotted in Fig. 3.10. The proposed antenna

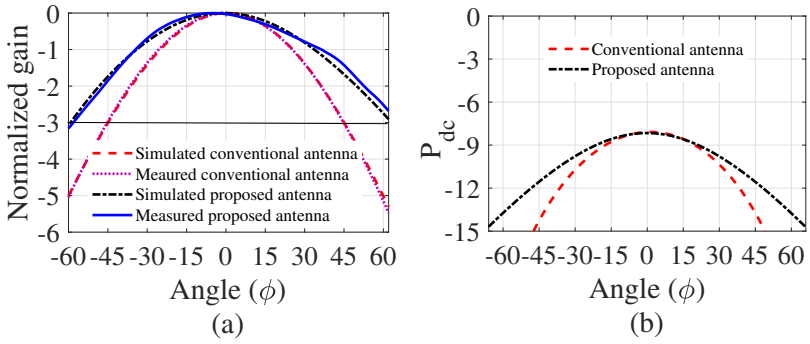

Figure 3.10: (a) Simulated normalized gain and (b) evaluated P_{DC} patterns.

has a symmetric radiation pattern without side-lobes similar to that of the conventional patch included for comparison in Fig. 3.10, hence, Step-4 is satisfied. For Step-5, the

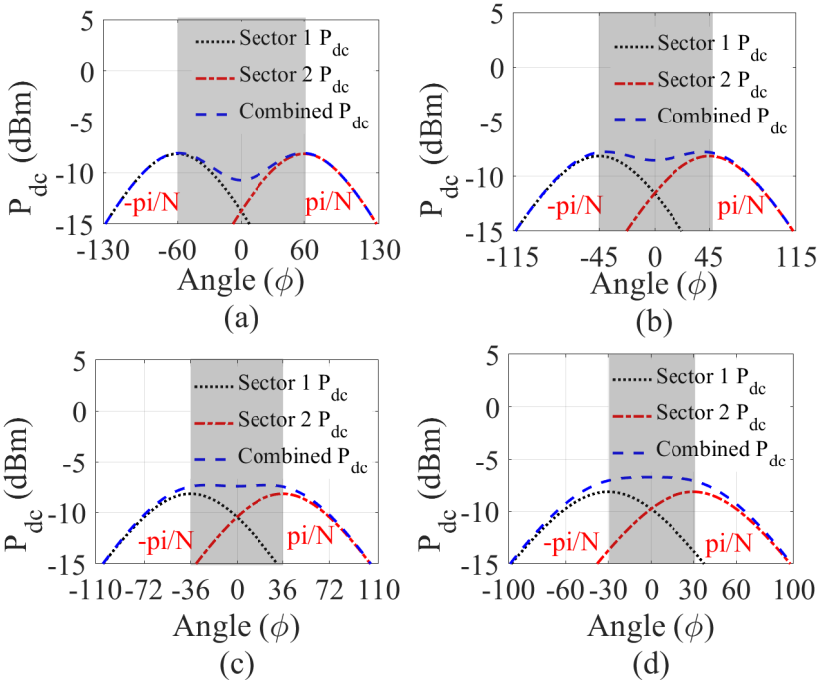

Figure 3.11: Simulated P_{DC} Pattern of the H1A1 WPT system for (a) $N = 3$ (b) $N = 4$ (c) $N = 5$,and (d) $N = 6$ sectors.

proposed antenna is analyzed for various N in Fig. 3.11 to explicitly satisfy the condition $P_{DC}^{opt}(\phi + \frac{\pi}{N}) + P_{DC}^{opt}(\phi - \frac{\pi}{N}) = 1$, $\forall \phi \in \left[\frac{-\pi}{N} \ \frac{\pi}{N}\right]$ for a complete mitigation of the angular misalignment problem. The plots indicate that $N = 6$ almost achieves the uniformity within the highlighted region, whereas the lower and higher values of N do not provide

the omnidirectional P_{DC} pattern. Hence, the H1A1 WPT node consists of $N = 6$ sectors compared to $N = 8$ sectors used in the conventional patch array. This shows that a wide-beam of the proposed antenna reduces the total number of sectors and enables a miniaturized WPT node. The H1A1 design is experimentally verified and performance is compared in subsection 3.3.4.

3.3.4 Experimental Verification and Results

The designs are fabricated and the radiation patterns of the antennas before integration are measured in an anechoic chamber. The measured radiation patterns are included in Fig. 3.10, which corroborating with the simulated patterns. The measured peak gains of the proposed and conventional antennas are 4.8 dBi and 4.89 dBi, respectively, near to the simulated 5 dBi peak gain.

The harvested DC measurements are conducted using the setup of Fig. 3.12 showing the fabricated prototype of the H1A1 multi-sector rectenna array. The proposed rectenna elements are integrated in the azimuth to cover 360° to build three prototypes with $N = 4$, 5, and 6 sectors to verify the simulation results. The DC power received from individual sectors is integrated using series DC combining technique. An optimum load of 2010 Ω is employed to harvest a maximum P_{DC} calculated for a single rectenna. Whereas, for the H1A1 and conventional WPT designs, the optimum loads used are 12060 Ω and 16080 Ω, respectively. In the measurement setup of Fig. 3.12, a Tx antenna having 8.6 dBi gain

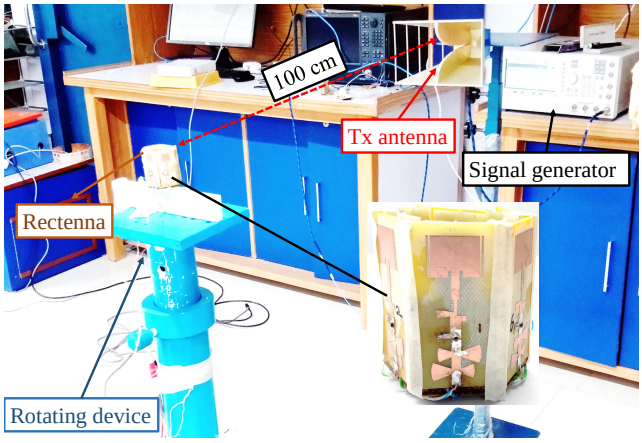

Figure 3.12: The fabricated prototype of the H1A1 WPT node and measurement setup.

is installed at 100 cm distance from the WPT node. The Tx is fed using a RF signal generator (Agilent Technologies E8257D) set at 25 dBm output power level [129]. The maximum power transfer range is limited by the frequency of operation, EIRP of the RF shower, and rectifier circuit sensitivity governed by Schottky diode. For a given WPT system, a higher range can be obtained by allowing higher EIRP values for RF showers as per the application requirements. For instance, in the outdoor application scenarios where biological interventions are less likely as compared to the indoor, EIRP of as high as 53 dBm [130] have also been used. Whereas, for the other applications, exposure is constrained by limiting EIRP value for a maximum allowed SAR, e.g., 1.6 W/Kg from

the FCC guidelines. Initially, a spectrum analyzer is used to measure the maximum RF power received by the proposed antenna. The corresponding harvested DC voltage is measured using Keysight multimeter (U1232A). To measure the angular misalignment performance, the WPT node is affixed on a rotating platform such that the harvested DC voltage is measured for the entire 360° rotation of the node in the azimuth plane in 5° steps. The measured DC patterns of the H1A1 WPT system are shown in Fig. 3.13. The

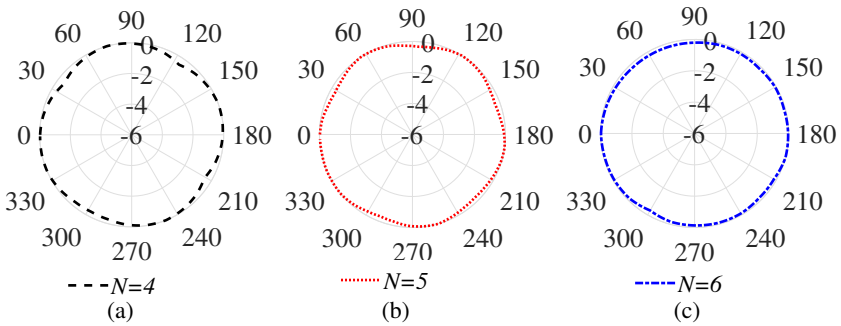

Figure 3.13: Measured P_D patterns of WPT system using proposed antenna for (a) $N = 4$ (b) $N = 5$, and (c) $N = 6$ sectors.

measured plots indicate that the P_D patterns for the H1A1 WPT designs having $N = 4$ and $N = 5$ sectors consist of dips as observed in the simulated results. The measured P_D for $N = 6$ design is uniform at all angles of the node misalignment, as shown in Fig. 3.13 (c), illustrating that $N = 6$ sectors is required to mitigate the angular misalignment problem. The H1A1 WPT node performance is compared with the WPT system fabricated using the conventional patch antenna. The conventional system is measured for designs with $N = 4 - 8$ sectors and the DC patterns are shown in Fig. 3.14. The measured

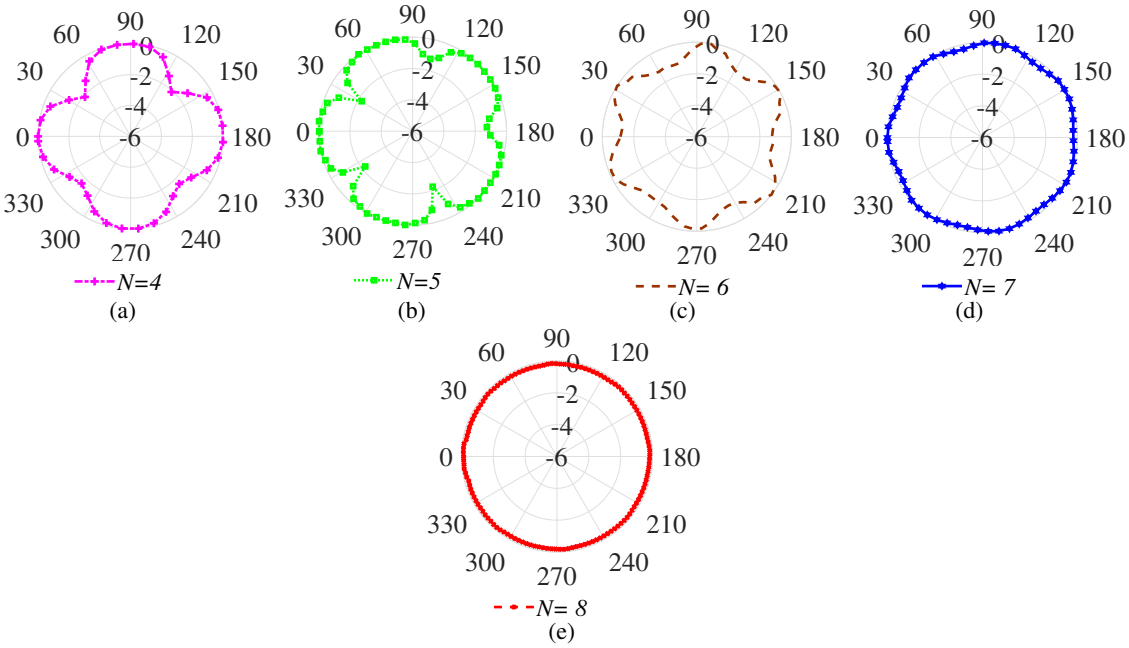

Figure 3.14: Measured P_D of the conventional WPT system with single element for (a) $N = 4$ (b) $N = 5$ (c) $N = 6$ (d) $N = 7$, and (e) $N = 8$ sectors.

results indicate that the conventional WPT system has dips in the P_D patterns for the designs with $N = 4 - 7$. The P_D pattern is uniform for $N = 8$ design, as shown in Fig. 3.14 (e), indicating the optimal sectors required to mitigate the angular misalignment problem by the conventional patch antenna. The measured open DC voltage readings of the conventional and H1A1 WPT systems are 1148 mV and 1252 mV, respectively. The H1A1 WPT system shows 100 mV higher reading than the conventional system due to reduction of DC combining losses in lower number of sectors used. Moreover, the proposed design has 36.5 % reduction in size compared to the conventional design. The results of the H1A1 and conventional WPT systems exhibit a good agreement between the analytical and measurement results validating the applicability of the proposed procedure.

3.3.5 Effects of DC Combining

The DC power combining efficiency is studied for multi-source transmissions in [55] which deals with ambient RF harvesting. Whereas, to emphasize that the proposed work is for dedicated RF energy harvesting applications which only require single-source measurements. Here, a smart DC combining network [44, 131] can be employed to improve overall combining efficiency. Nevertheless, all investigations related to single-source as well as multi-source are carried out for complete characterization of the DC combining losses. For this measurements, the radial multiport WPT systems are serially combined to obtain a single output, as shown in Fig. 3.12. The dedicated multi-source and single-source measurements are performed to analyze RF-DC and DC combining losses. Each sector has an optimal load of 2010 Ω and the series combined array of γ sectors has $\gamma \times 2010$ Ω. The single-source measurements are presented first to determine the dynamic power performance of the H1A1 WPT system.

3.3.6 Single-source Measurements

The single-RF source excites different RF power in each sector rectenna. Therefore, the dynamic input RF power performance of the WPT system is easily characterized using the single-source measurements. The DC power harvested from γ sectors are assumed combined using a smart DC combining circuit illustrated in Fig. 3.15 to improve the overall system efficiency by bypassing the low harvesting $(N - \gamma)$ rectenna elements. For

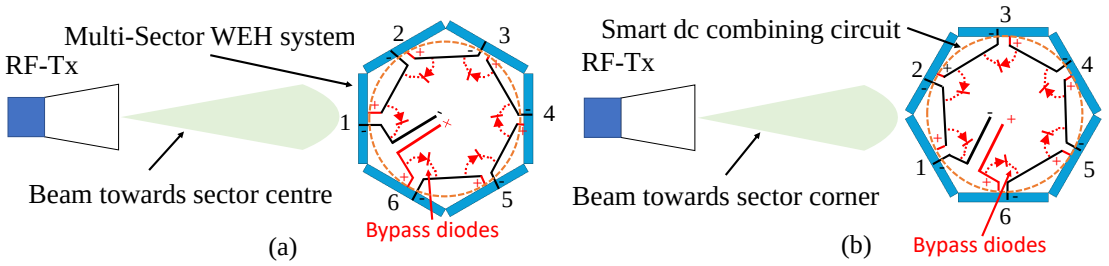

Figure 3.15: Smart power summation network for (a) aligned toward center and (b) corner of the sectors series combining based multiple rectenna elements.

experimental study of the system efficiency, the low harvesting rectennas are shorted out by using an equivalent low loss resistance of the bypass diode.

In addition, since the single-source (RF-Tx) can be aligned towards any orientation of the WPT system, two cases for measurements are considered for this purpose; the Tx aligned to sector-1 or facing the corner of a sector-1-2 as illustrated in Fig. 3.15 (a) and Fig. 3.15 (b), respectively. In the setup of Fig. 3.15 (a), an odd number of sectors facing the Tx are illuminated, whereas, in Fig. 3.15 (b) setup, an even number of sectors are illuminated and combined to measure the efficiency. This is due to the Tx radiation pattern symmetry across the line joining the Tx and the center of the multi-sector WPT system. The measured results of the RF-DC conversion and DC combining efficiencies for both the cases are presented in Table 3.2 and Table 3.3, respectively.

Table 3.2: Measured efficiency with single RF power source aligned with center of the sector

γ	On Rectenna elements	Bypassed Rectenna elements	Input RF power (μW)	Output DC power (μW)	RF-DC efficiency (%)	DC combining efficiency (%)
1	1	2, 3, 4, 5, 6	105.55	70.71	67	100
3	1, 2, 6	3, 4, 5	187.61	100.3	53.46	87.50
5	1, 2, 3, 5, 6	4	202.11	64	31.66	63.7

Table 3.3: Measured efficiency with single RF power source aligned with the corner of the sector

γ	On Rectenna elements	Bypassed Rectenna elements	Input RF power (μW)	Output DC power (μW)	RF-DC efficiency (%)	DC combining efficiency (%)
2	1, 2	3, 4, 5, 6	160.14	104.45	65.22	94.1
4	1, 2, 3, 6	4, 5	193.58	85.86	44.35	86.1
6	1, 2, 3, 4, 5, 6	-	207.08	60.16	29.05	59.89

The results indicate a sharp decrease in RF-DC efficiency from 67% to 29.05% as the number of DC combined rectenna elements increases from one to six. Similarly, the DC combining efficiency decreases from 100% to 59.89%. This steep decrease in efficiency can be attributed to the non-linear characteristic of the rectifier circuit due to the dynamic power received at each sector. Moreover, the output DC powers harvested by combining $\gamma = 2$ and $\gamma = 3$ sectors are equivalent as the WPT node orientation varies. Hence, this can be chosen for the smart DC combining circuit to achieve omnidirectional DC power harvesting, verifying the results obtained through mathematical analysis discussed in Section 3.2.5. The multi-source measurements are discussed in the subsection 3.3.7.

3.3.7 Multi-source Measurements

The multi-source experiment is carried out by arranging all the rectenna elements in a row facing the single RF-Tx source. This equivalent topology is adopted due to the availability of only a single RF source in the laboratory. The same amount of RF power is expected

to be delivered to all the rectenna elements imitating a multi-source system for the radial multi-sector structure.

Table 3.4: Measured efficiency with multi-source experiment

On Sector elements	Input RF power (μW)	Output DC power (μW)	RF-DC efficiency (%)	DC combining efficiency (%)
1	105.55	70.71	67	100
2	105.55	69.96	66.28	100
3	105.55	70.34	66.63	100
4	105.55	71.09	67.34	100
5	105.55	69.96	66.28	100
6	105.55	69.59	65.93	100
1, 2, 3	316.65	193.43	61.08	91.67
1, 2, 3, 4, 5, 6	633.3	358.74	56.64	85.08

The DC combining efficiency is evaluated as the total harvested DC power divided by the sum of the DC power harvested by the individual sectors. The measured RF-DC and DC combining efficiencies are shown in Table 3.4. The RF-DC efficiency of a single element is $\sim$ 66 %, which reduces to 61.08 % and 56.64 % for the series combination of sectors-$1, 2, 3$ and sectors-$1, -$ to 6, respectively. The DC combining the efficiency of $\sim$ 91.67 % is obtained for combining sectors-$1, 2, 3$ which reduces to $\sim$ 85.08 % for combining sectors-$1, -$ to 6. The findings indicate that circuit loss are notable in series combining. Further, it can be observed from the results that the multi-source topology provides better efficiency than a single source. This indicates that multiple RF sources can potentially increase the power density around the WPT system to capture higher DC power. A high-gain WPT system is presented in section 3.4 to capture maximum RF power with the same form factor of conventional design.

3.4 H1A2: High Gain Multi-sector Rectenna Array

The H1A1 design mitigates angular misalignment completely, however, it has a low output DC voltage. Therefore, a high gain, multi-sector H1A2 WPT system is presented to improve the RF capturing capabilities. Each sector of the H1A2 WPT system is composed of a parasitic element enabled antenna, an IMN, a DC-LPF, and a Schottky diode (SMS$-7630-079LF$). The SMS$-7630-079LF$ is adopted due to its low junction capacitance, high cut-off frequency, and excellent RF-DC efficiency at low input RF power levels. The presented rectifier is designed for a received RF power level of -8.1 dBm. The exploded view of complete layout and dimensional parameters of the H1A2 WPT system are shown in Fig. 3.16. The Rectenna design is discussed in section 3.4.1.

3.4.1 Rectenna Design

The presented antenna is a multi-layered structure composed of a parasitic element and two metallic strips. The parasitic element (4mm above the main radiator) enhances the antenna gain (7.1 dBi). The two metallic strips are used to improve impedance matching

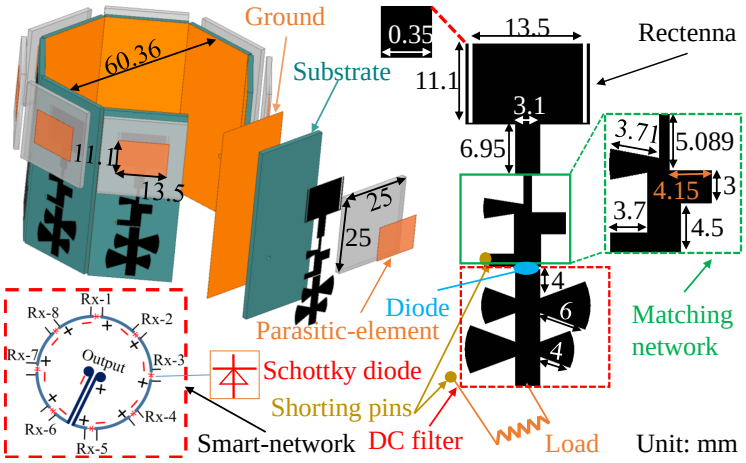

Figure 3.16: Layout of the H1A2 WPT system.

and gain (7.2 dBi) without compromising beamwidth. In addition, the received RF power is DC converted using a rectifier whose load and impedance is optimized using the LSSP technique at 5.8 GHz in the presence of DC-LPF. The DC-LPF is designed using four radial stubs to filter out higher-order harmonics to improve system efficiency. Similarly, IMN is designed using radial and shunt stubs to improve the impedance matching between rectifier and antenna. The dimensional parameters of IMN and DC-LPF are optimized to achieve better impedance matching and enhanced PCE.

3.4.2 Smart-Network

The DC power harvested from each sector is combined using a series DC combining technique to feed the rechargeable battery. The single RF source illuminates only a few sectors non-uniformly in the H1A2 WPT system as depicted in Fig. 3.1. Therefore, the performance of the direct series DC combining is degraded due to unexcited rectennas which do not face the Tx and serve as dead loads [44]. To mitigate the loading effect of the unexcited rectennas, a smart-network with DC combining circuit is employed as illustrated in the bottom inset of Fig. 3.16. For smart-network, Toshiba 1SS384TE85LF diodes having low turn-on voltage of 0.1 V are used. One such diode is connected in shunt to each rectenna output and can bypass the under-performing rectennas which are unexcited and hence provides a low resistance bypass path to the DC. The simulated P_D pattern of the proposed antenna is demonstrated for various N in Fig. 3.17. The results show that $N = 8$ sectors are sufficient to achieve a uniform $P_D(\phi)$ and completely mitigate the angular misalignment.

3.4.3 Fabrication and Measurement

The H1A2 WPT system is fabricated and its performance parameters are measured using the setup shown in Fig. 3.18. The measurement setup of the H1A2 WPT system is discussed in Section 3.3.4. The H1A2 WPT system is placed at 1 m distance from the Tx, and the power received at the rectenna aperture is measured using a spectrum analyzer.

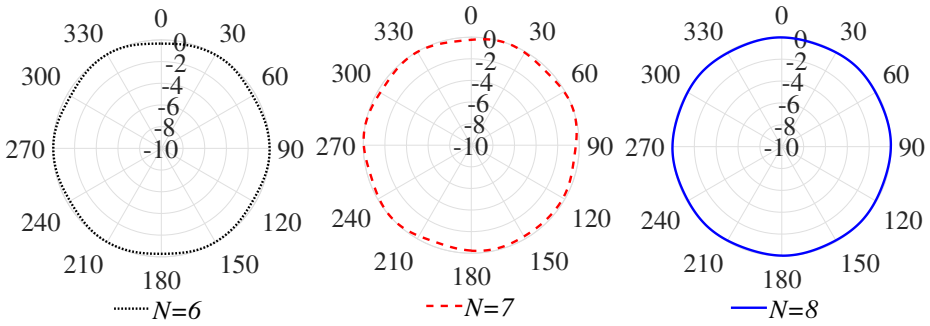

Figure 3.17: Simulated P_D pattern of the H1A2 WPT system for (a) N = 6 (b) N = 7 and (c) N = 8 sectors.

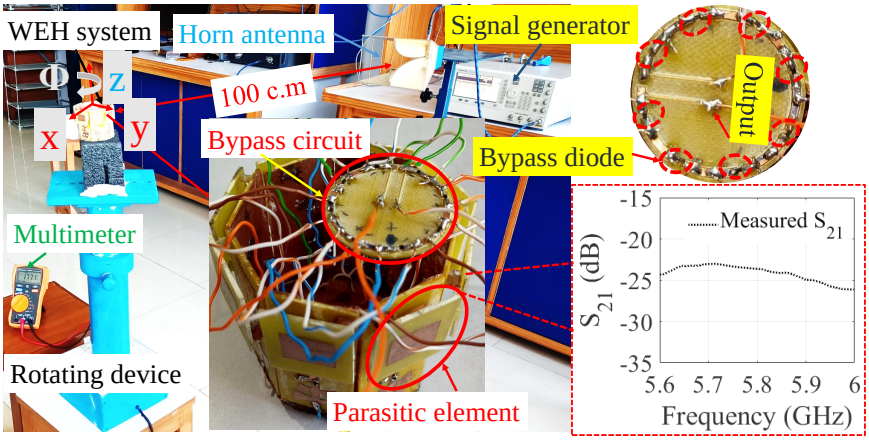

Figure 3.18: Measurement setup of the H1A2 WPT system.

The isolation of 23 dB is achieved between the adjacent sector antenna elements. The H1A2 WPT system is rotated using a turn table to measure its angular misalignment tolerance. The measured DC power plots of the H1A2 WPT system for $N = 7$ and $N = 8$

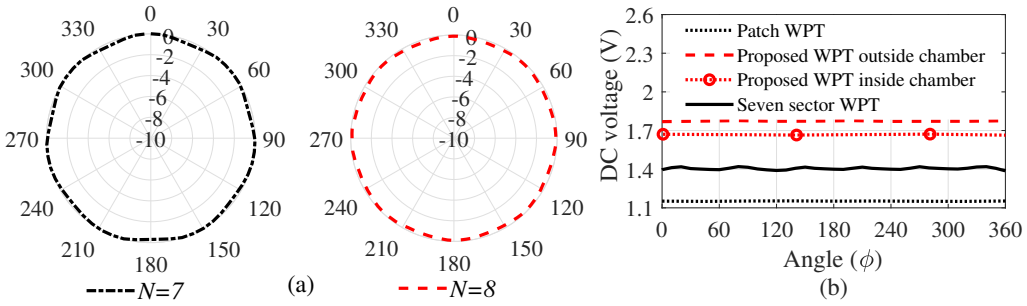

Figure 3.19: (a) Measured P_D pattern with $N = 7 - 8$, (b) measured DC voltage of the H1A2 and patch WPT system.

are illustrated in Fig. 3.19. The average harvested DC voltage for $N = 7$ and $N = 8$ sectors is 1404.4 mV and 1773.3 mV with standard deviation in pattern uniformity of 0.0304 mV and 0.0018 mV, respectively, in outside chamber environment. The results indicate that $N = 8$ is the optimal number of sectors for both WPT systems to achieve the uniform DC power in the azimuth plane. Moreover, the measured open DC voltage of the H1A2 WPT system (1771 mV) is more significant than the patch WPT system (1148 mV), as shown

in Fig. 3.19 (b), since the former has 2.2 dBi more gain in each sector than the latter. In addition, the harvested DC voltage is higher in the outside chamber environment as compared to inside chamber due to multipath effect. The measured DC efficiency of the

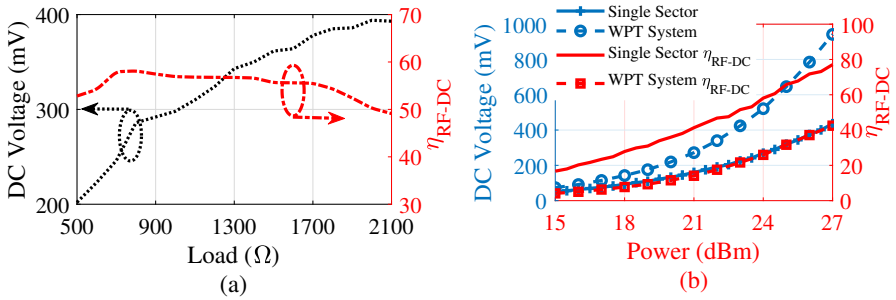

Figure 3.20: (a) Measured η_{RF-DC} versus DC voltage of single element, (b) measured DC voltage versus Tx power.

Table 3.5: Measured DC power of individual rectenna sectors

Elements	1	2	3	4	5	6	7	8
Power (μW)	90.45	24.15	0.5	0.031	0.005	0.031	0.5	24.15

proposed single sector-1 facing the Tx is 58.55 %, which produces 269 mV at its optimal load of 800 Ω as shown in Fig. 3.20 (a). Further, the harvested voltage and efficiency

Table 3.6: Measured data with Tx aligned with center of the sector-1

N	On Rectenna elements	Input RF power (μW)	Output DC power (μW)	RF-DC efficiency (%)	DC combining efficiency (%)	L_{DCc}
1	1	154.48	90.45	58.55	100	0
2	1, 2	212.54	104.73	49.27	91.38	0.0862
3	1, 2, 8	270.6	125.69	46.44	90.58	0.0942
4	1, 2, 3, 8	277.87	108.69	39.11	78.05	0.2195
5	1, 2, 3, 7, 8	285.14	99.64	34.94	71.29	0.2871
6	1, 2, 3, 4, 7, 8	289.87	89.55	30.89	64.06	0.3594
7	1, 2, 3, 4, 6, 7, 8	294.6	82.88	28.13	59.27	0.4073
8	1, 2, 3, 4, 5, 6, 7, 8	298.97	77.55	25.93	55.46	0.4454

for individual and various combinations of the sectors are measured for different power levels are shown in Fig. 3.20 (b). The efficiency of the complete WPT system is increased with the increment of P_{tx}. Moreover, the efficiency of $N = 8$ sectors is 25.93 % for above mentioned P_{tx} level at its optimal load of 3500 Ω. The measured DC power of the individual sectors constituting the H1A2 WPT system while the sector-1 is facing the Tx are presented in Table 3.5, indicating insignificant contributions by the backside sectors (element-3 to -7). Further, for various numbers of DC combined sectors N, the measured DC combining efficiency and $L_{DCc}(N)$ are listed in Table 3.6. The H1A1 and H1A2 designs have 3-D geometries, therefore a planar WPT H1A3 is investigated in the subsequent section.

3.5 H1A3: Planar design to mitigate azimuthal angular misalignment

The H1A1 and H1A2 designs mitigate angular misalignment, however, they have 3-D geometries, which have limited applicability in IoT applications. Therefore, to address this issue, a novel planar H1A3 WPT system is designed and optimized using commercial softwares including Ansys HFSS and Keysight ADS.

3.5.1 Simulation

The design is realized on a traditional dual-sided PCB of FR4 substrate having 1.565 mm thickness (dielectric constant $\epsilon_r = 4.4$ and loss tangent $\tan\delta = 0.02$) at an operating frequency of 5.8 GHz. A single high gain directional rectenna is unable to harvest energy from a wide azimuth coverage. Moreover, the orientation estimation can not be implemented with one received sample acquired from a single antenna element. Therefore, to improve WPT coverage, orientation resolution, and accuracy, a 2-D radial array H1A3 WPT system is proposed, as shown in Fig. 3.21. The antenna array comprises N= 8 sectors of scoop-shaped rectenna element with horizontal polarization and end-fire radiation pattern in the azimuth plane. Over the top, the module consists of a protective

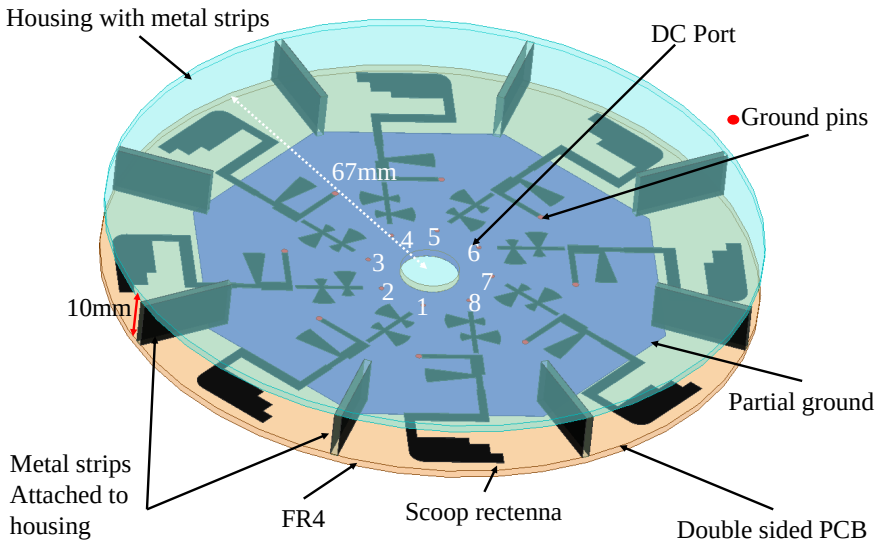

Figure 3.21: The proposed dual-purpose rectenna array sensor module layout.

housing with 8 metal strips as an integral part of the design, which provides 10 mm separation to create spacing for SMDs, circuit modules, and the device controls as well as improves the directivity of the radiating antenna array elements. The entire system is co-simulated and optimized by accounting the effect of the housing on the rectenna performance. Each rectenna comprises a compact scoop-shaped antenna with a partial ground plane, a matching circuit, a Schottky diode (HSMS 7630-079LF), and a DC-LPF. The complete layout with dimensional parameters of the proposed rectenna element is

depicted in Fig. 3.22. The antenna collects RF energy and converts it into DC output

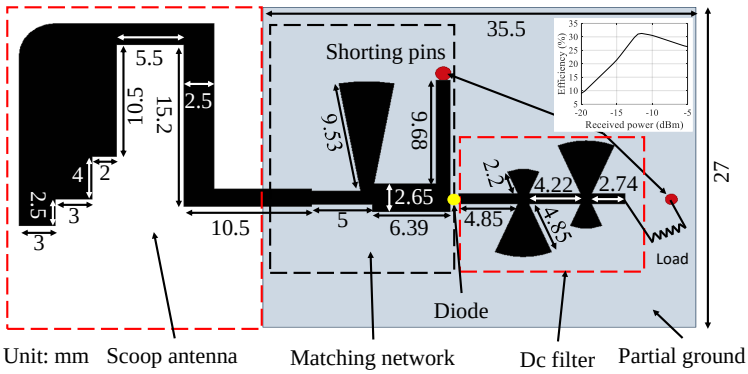

Figure 3.22: The proposed rectenna element with compact scoop-shaped antenna.

through the rectifier circuit, which is used to recharge a battery and estimate sensor node orientation. The performance of the proposed scoop-shaped antenna is optimized in terms of size, impedance matching, and radiation characteristics as desired for WPT and localization application. Furthermore, the matching network is implemented using a radial and a short circuit stub, and the other four radial stubs are integrated to implement a low-pass filter in order to filter out higher-order harmonics. The rectenna elements are terminated with DC ports as shown in Fig. 3.21 from which the received DC signals can be joined together for WPT using an appropriate DC combining technique to feed the battery and also further processed for orientation estimation using a computing device. To demonstrate the performance of orientation estimation, a Minimum Mean Square Error (MMSE) based scheme is implemented. Let the DC voltage, $V_i(\phi)$, is expected to appear at the DC port-i $\forall i \in [1, N]$ when the sensor node has orientation ϕ as defined in Fig. 3.23. The complete $V_i(\phi)$ $\forall \phi \in [0, 2\pi], i \in [1, N]$ profile represents the expected data which can be obtained by simulation and experimental calibrations and saved for reference to be used by any localization algorithm. Once the sensor node has actual orientation ϕ_k, the measured voltages, $V_i'(\phi_k)$, appear in real-time at the DC port-i $\forall i \in [1, N]$. The MSE, E_ϕ, between measured $V'(\phi_k)$ and the reference profile $V_i(\phi)$ is evaluated $\forall \phi \in [0, 2\pi]$ as

$$E_\phi = \frac{1}{N} \sum_{n=1}^{N} \left[V_i(\phi) - V_i'(\phi_k) \right]^2 \tag{3.23}$$

Using E_ϕ, the estimated orientation, ϕ_k', is determined by invoking MMSE as

$$\phi_k' = \arg_{\phi} [\min \; E_\phi] \tag{3.24}$$

and the error in orientation estimation is $\Delta\phi_k = |\phi_k - \phi_k'|$ with average error $\overline{\Delta\phi}$ evaluated as

$$\overline{\Delta\phi} = \frac{1}{M} \sum_{k=1}^{M} \Delta\phi_k \tag{3.25}$$

for M testing orientations taken in the measurement. For brevity, only the experimental results are presented to validate the claims of the proposed design.

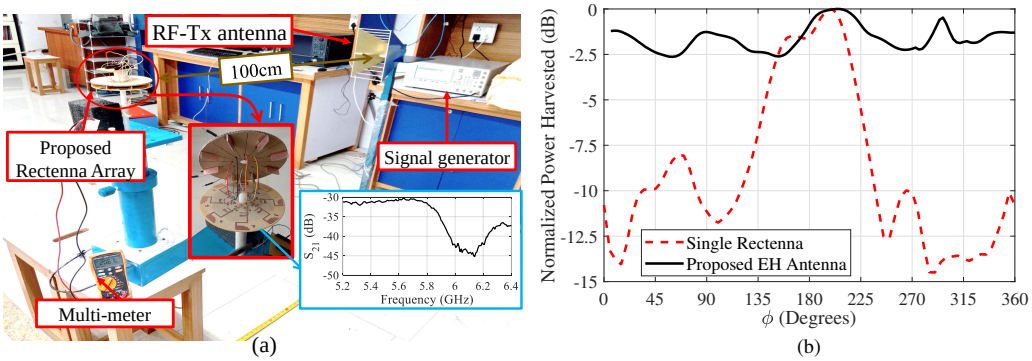

Figure 3.23: (a) Measurement setup and (b) received power of the presented H1A3 WPT system

The measurement setup is demonstrated in Fig. 3.23(a), which has all components as explained earlier in Section 3.3.4. The fabricated prototype of the proposed H1A3 WPT system with DC assembly is shown in the inset of Fig. 3.23(a). The proposed scoop-shaped antenna shows a measured gain of 7 dBi in the anechoic chamber and isolation $>$ 30 dB is achieved between the two adjacent antenna elements. The RF to DC conversion efficiency of the system is 31.22 % for an optimal load of 2010 Ω when the RF power of -12 dBm is received by the antenna.

3.5.2 Energy Harvesting Performance

The node is rotated in $0° - 360°$ with a step of $5°$ in the ϕ direction using an automated positioner. The comparison of power harvested by the presented H1A3 WPT system is shown in Fig. 3.23(b) with a single rectenna element. The results indicate that a high variation exists in power harvested by the single rectenna element due to its directional pattern, whereas the proposed rectenna array shows better stability in harvested power with change in ϕ. This demonstrates the capability of the proposed design to mitigate the orientation misalignment problem.

3.5.3 Orientation Estimation Performance

Using the same setup of Fig. 3.23(a), first, the voltage profile $V_i(\phi)$ is experimentally calibrated for all the orientations of the sensor node and saved for MMSE based orientation estimation. The node is rotated very precisely for $0° - 360°$ in ϕ using the automated positioner. The $V_1(\phi)$ to $V_8(\phi)$ profiles of the rectenna elements are shown in Fig. 3.24 (a), which correspond to their azimuth DC voltage patterns and demonstrate the eight beams formed to cover the entire 360°. The node is rotated in $0° - 360°$ with a step of $5°$ for various ϕ_k to observe $M = 73$ testing orientations. The measured voltage readings $V_1'(\phi_k)$ to $V_8'(\phi_k)$ from rectennas (Rect-1 to Rect-8) are shown in Fig. 3.24(b). Further, using (3.23-3.25) the orientation of the node is estimated and the average estimation error $\overline{\Delta\phi}$ is

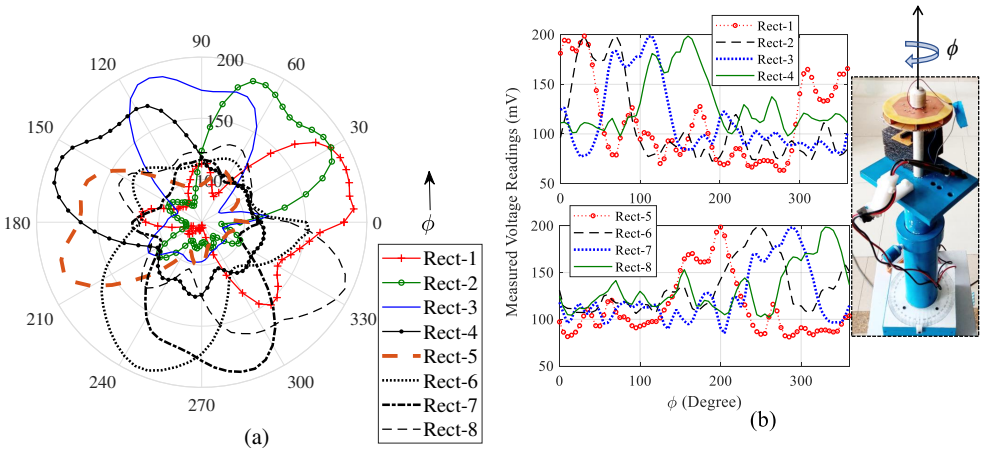

Figure 3.24: Experimentally calibrated DC voltage pattern of each rectenna and (b) voltage measurement readings taken from all rectennas

evaluated. The actual and predicted values of the orientations are plotted in Fig. 3.25(a), and estimation errors $\Delta\phi$ varying from $-4°$ to $3°$ are observed as shown in Fig. 3.25 (b). The $\overline{\Delta\phi} = 1.0822°$ with standard deviation of $0.9242°$ is observed. The results indicate good orientation estimation accuracy using the proposed design.

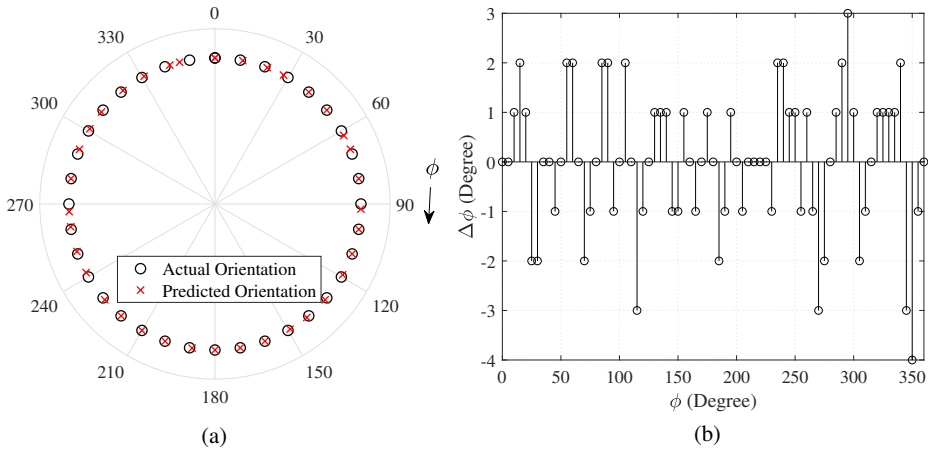

Figure 3.25: (a) Actual and predicted orientation of the sensor nodes and (b) orientation estimation error for various test samples.

3.6 Comparison with State-of-The-Art

The comparison with the state-of-the-art WPT systems are shown in Table 3.7, which generate multiple beams to enhance the coverage and harvest power in a wide area. For instance, two beams [35, 42], four beams [28, 53], six beams [44] and twelve beams [54] multi-port designs reported in the literature to enhance the spatial coverage. However, large dimensions make them unsuitable for deployment at sensor nodes. Furthermore, all the existing designs have star-shaped DC patterns persisting in the angular misalignment problem and using multiple SMD components to design integrated systems, which renders them due to complex and cost-inefficient. In contrast, the integrated design proposed

Table 3.7: comparison with state-of-the-art

	Frequency (GHz)	Beams	Sectors	port	size ($\lambda_0 \times \lambda_0$)	Beam mechanism	Mitigate angular misalignment	η_{rf-DC} (%)
[28]	2.4	4	4	4	$2.37\lambda_0 \times 0.68\lambda_0$	butler matrix	No	45 at −5 dBm
[53]	2.45	4	4	4	$0.82\lambda_0 \times 1.96\lambda_0$	butler matrix	No	42.4 at -10 dBm
[35]	2.3 – 2.63	2	2	2	$0.40\lambda_0 \times 1.57\lambda_0$	simple	No	45 at -10 dBm
[42]	2.45	2	1	2	$1.85\lambda_0 \times 3.08\lambda_0$	simple	No	42 at −10 dBm
[44]	28	6	1	6	$5.13\lambda_0 \times 8.12\lambda_0$	Rotman Lens	No	-
[54]	2.45	Omni	6	6	$1.31\lambda_0 \times 1.31\lambda_0$	complex	Yes	-
[55]	1.7 – 1.8 2.1 – 2.7	Omni	12	12	$1.18\lambda_0 \times 1.18\lambda_0$ (2.45 GHz)	complex	Yes	∼ 47 at -10 dBm (2.45 GHz)
H1A1	5.8	Omni	6	6	$1.04\lambda_0 \times 1.04\lambda_0$	simple	Yes	∼ 67 at -10 dBm
H1A2	5.8	Omni	8	8	$1.23\lambda_0 \times 1.23\lambda_0$	simple	Yes	∼ 51.2 at -10 dBm
H1A3	5.8	Omni	8	8	$2.59\lambda_0 \times 2.59\lambda_0$	simple	Yes	∼ 31.22 at -10 dBm

in [55] also shows good angular tolerance, however, this employs 12 sectors to mitigate angular misalignment with the compromise of high DC combining losses. Further, the proposed designs (H1A1, H1A2 and H1A3) offer better η_{rf-DC} (%) compared to the reported designs with completely mitigating angular misalignment.

3.7 Summary

In this chapter, an analytical framework to address the angular misalignment problem in WPT systems (H1) is proposed. The omnidirectional DC power ($P_D(\phi)$) pattern is taken as the design objective to solve for the DC power pattern ($P_{dc}(\phi)$) of individual sectors. The solution provides four constraints over $P_{DC}(\phi)$ to determine the optimal number of sectors (N) required to achieve the design objective. The presented framework is analytically validated using the conventional patch rectenna (discussed in section 2.3) and provides $N = 8$ as the optimal solution for the conventional patch rectenna to mitigate the angular misalignment. Later, this analysis is applied to the proposed WPT rectennas (H1A1, H1A2, and H1A3) to obtain the optimal number of sectors to mitigate the angular misalignment. The analysis provides $N = 6$ (H1A1), $N = 8$ (H1A2), and $N = 8$ (H1A3) as the optimal solution for the compact WPT rectenna, high power harvesting rectenna, and a planar scoop rectenna array rectenna, respectively. A new multilayered broad-beam rectenna is presented with a 35.6 % wider beamwidth than the conventional patch rectenna (discussed in section 2.3) without compromising RF gain. The H1A1 WPT system designed using the proposed rectenna requires $N = 6$ sectors, resulting in 36.5 % size reduction as compared to the conventional WPT system. The DC combining losses of the different number of sectors (γ, detailed discussion in section 3.3.6, and 3.3.7) of the proposed WPT system is measured for single and multisource. The single source provides RF-DC efficiency of 65.22 % and 53.46 % for $\gamma = 2$ and 3, respectively. Further, a novel high gain WPT system (H1A2) is designed to achieve uniform harvesting capability

across 360° of the azimuth plane, with a 51.2 % increase in harvesting capability over the conventional WPT system. Although the H1A1 and H1A2 WPT systems completely mitigate angular misalignment with a 3D footprint, their large size renders them unsuitable for IoT applications. Therefore, a novel octahedral radial H1A3 WPT system is presented at 5.8 GHz for orientation sensing IoT nodes. The radial WPT system offers better tolerance for the angular misalignment problem and orientation sensing capability of the IoT sensor nodes. The eight rectenna elements provide eight samples for orientation estimation with good accuracy of $\sim 1^{\circ}$ average error. The measurement and analytical results support the applicability of the proposed framework, making it a viable choice for designing a multi-sector WPT system free of azimuthal angular misalignment. Moreover, the proposed designs are suitable for mitigating azimuthal angular misalignment; however, they have a large footprint and limited harvesting capacity in tilted and arbitrarily positioned IoT nodes. Therefore, to address this problem, a 3D-spherical coverage WPT system is analyzed along with miniaturization in Chapter 4.

Chapter 4

3D-Spherical DC Coverage Rectenna System

4.1 Introduction

The previous chapter proposed a mathematical framework for harvesting uniform RF power in the azimuth plane by mitigating azimuthal angular misalignment. However, IoT sensor nodes can be placed in any arbitrary orientation and position in smart indoor applications. Additionally, for dedicated wireless power transmission, the RF power transmitter (Tx) can be mounted anywhere on the ceiling or side walls, as shown in Fig. 4.1. Therefore, RF power harvested by a sensor node is a function of its orientation with respect

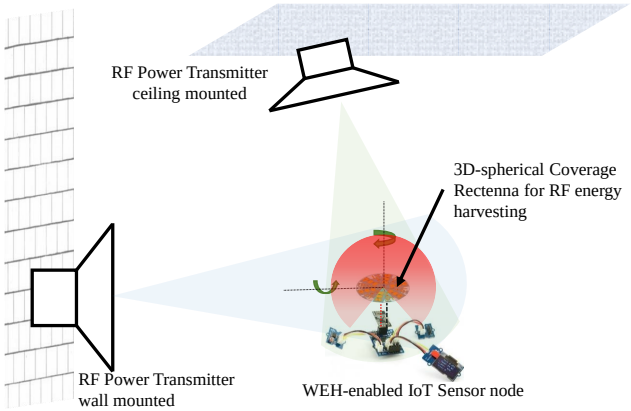

Figure 4.1: Dedicated WPT scenario and the need of 3D-spherical coverage WPT system for indoor application.

to the Tx. To reduce this dependency, H2B1, and H2B2 novel planar integrated rectenna array are presented with 3D-spherical coverage.

4.2 H2: A WPT system with 3D-Spherical coverage

The performance of the WPT system reduces when the WPT node rotates with respect to the Tx antenna in the azimuth and elevation planes, as discussed in Chapter 1, subsection 1.1.1. This can be addressed by optimizing DC power patterns in elevation and azimuth planes with 3D spherical coverage. The main content of this chapter are the following:

- The presented work is the first attempt to achieve the desired 3D-spherical coverage using a 2-D planar (two-layer PCB-based) design with a simple and integrated

compact array structure which is easily realizable as compared to the BFN.

- The direct impedance matching of the antenna elements and rectifying diodes is incorporated along with easily realizable parallel combining of rectenna elements to achieve a fully integrated design.
- The bore-sight antenna work as dc low-pass filter under the rectification process.
- Multiple rectenna elements are amalgamated using a simple and easily realizable parallel dc combining circuit, making it cost-effective for IoT sensor nodes.

The detailed discussion on the presented H2B1 is discussed in Section 4.3.

4.3 H2B1: A Design for 3D-spherical Coverage

4.3.1 Design Layout

The H2B1 WPT system is designed on a dual-sided copper cladded FR4 substrate (dielectric loss, $\epsilon_r = 4.4$, and loss tangent $\tan\delta = 0.02$) using commercial ANSYS HFSS and Keysight ADS software at 5.8 GHz. The PCB layout of the presented H2B1

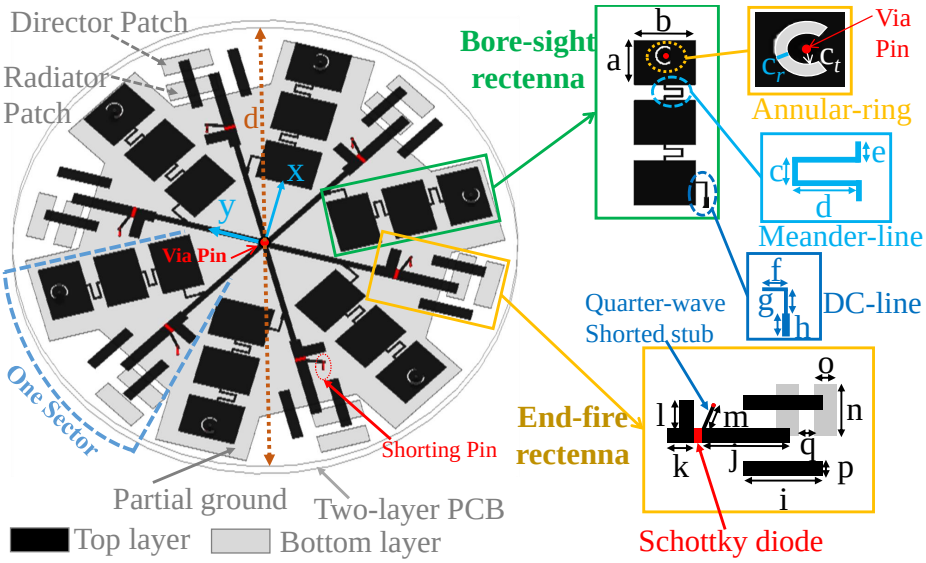

Figure 4.2: Design layout of the presented H2B1 WPT system.

WPT system is elaborated in Fig. 4.2 and the corresponding dimensional parameters are denoted. The H2B1 WPT system comprises of six sectors, and each sector has a pair of one end-fire and one bore-sight antenna each integrated with a shunt Schottky diode (SMS-7630-079LF) and connected together with a DC-line (RF-choke), as depicted in Fig. 4.2. The presented end-fire rectenna has 57° and 87° DC beamwidth in the azimuth and the elevation plane, respectively. The wider beamwidth provides a flat DC pattern in the azimuth for six sectors. Moreover, the bore-sight rectenna has a 15° beam tilt away from the elevation axis (z-axis) and towards the radially outward direction, which enhances the elevation plane coverage and provides nearly the full 3D-Spherical coverage

in cooperation with the end-fire elements. The enlarged bottom view of the ground plane

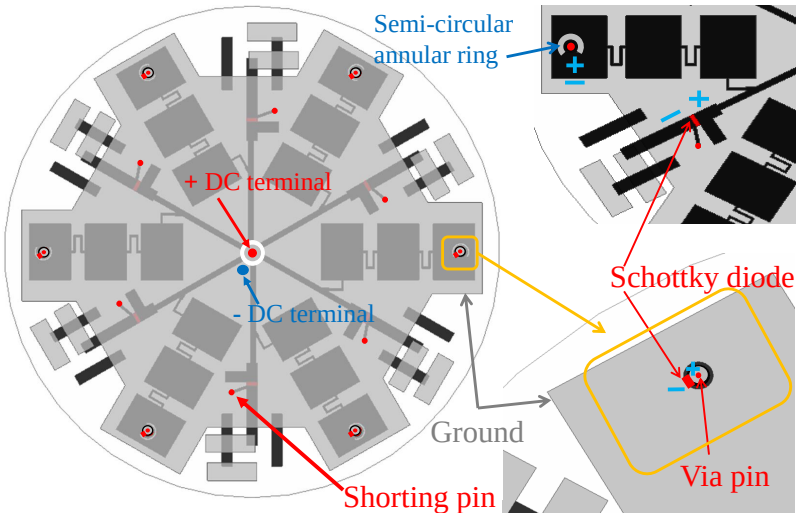

Figure 4.3: Enlarged view of bottom layer of the presented H2B1 WPT system.

of the H2B1 WPT system with detailed DC connections is provided in Fig. 4.3. The Schottky diodes are utilized for designing the half-wave rectifier using shunt topology for RF-DC conversion. The mentioned Schottky diode is adopted due to its low junction capacitance, high cut-off frequency, and excellent power threshold efficiency at a low input RF power range. The values of corresponding dimensional parameters defined for a single sector in Fig. 4.2 are provided in Table. 4.1.

Table 4.1: Dimensional parameters of the presented rectenna system.

Parameters	a	b	c	d	e	f	g	h	i	j	k	l	m	n	o	p	q	c_r	c_t	d
Dimensions (mm)	11.8	16	2.5	4.5	1.25	3	4	2	15	16.26	5.5	6	5.4	14	5	3	3	0.5	4	130

4.3.2 Direct Matching and Integration with Rectifier

The design topology of direct conjugate matched end-fire and bore-sight rectennas utilizes two different diode placement schemes presented in Fig. 4.4(b)-(c) so that a fully integrated rectenna in a single PCB is realized with miniaturization. In the scheme of Fig. 4.4(b), a quarter-wave shorted stub provides DC connection (DC terminal) to the end-fire rectenna. This is followed by a DC-LPF imitated by the 3×1 bore-sight element to reduce the number of components. Similarly, in the scheme of Fig. 4.4(c), the same bore-sight element works itself as a DC-LPF and a DC-line is fused to provide DC connection to the element. A detailed description of implemented layouts of both the topology is provided later in Section 4.3.3. To begin the implementation, first the impedance of the Schottky diode is calculated by simulations at 5.8 GHz using the LSSP and harmonic balance (HB) technique in Keysight ADS software. The input impedance of the Schottky diode ($Z_d = 25.03 - j93.96\ \Omega$) is evaluated at -10 dBm input power level and simulated optimal output load of 900 Ω. The design evolution of the presented integrated rectenna is discussed subsequently.

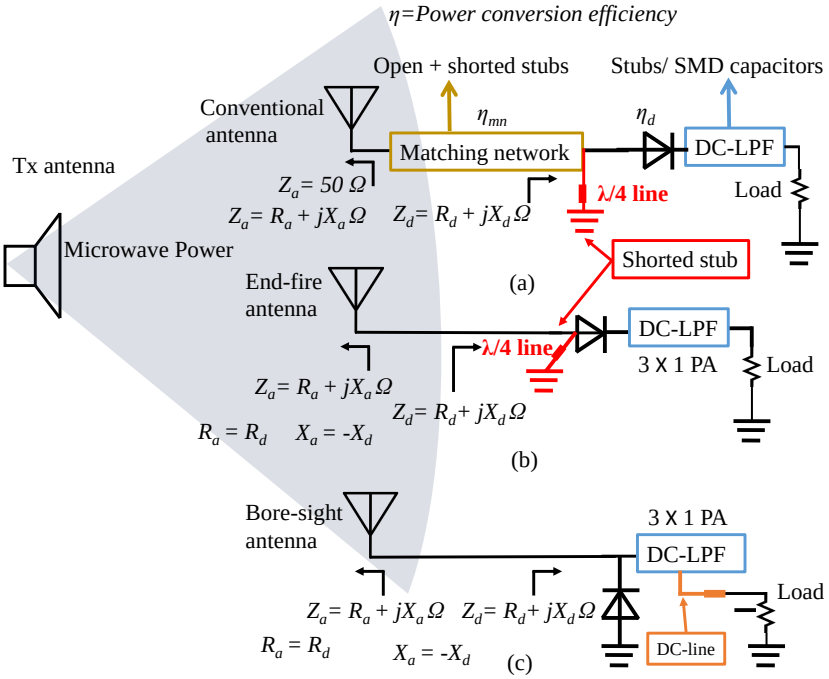

Figure 4.4: (a) Conventional rectenna with the IMN (50 Ω, $R_a + jX_a$ Ω). (b) end-fire rectenna without IMN and (c) bore-sight rectenna without IMN.

4.3.3 End-fire Rectenna Design

The end-fire rectennas reported in the literature [35] have a bulky size with a narrow beam pattern. Hence, a large number of sectors are required to mitigate the angular misalignment, which increases overall system size, circuit complexity, and losses. To achieve miniaturization along with a wide-beam DC pattern, a new end-fire rectenna element is designed and shown in Fig. 4.5. The presented design is inspired from a

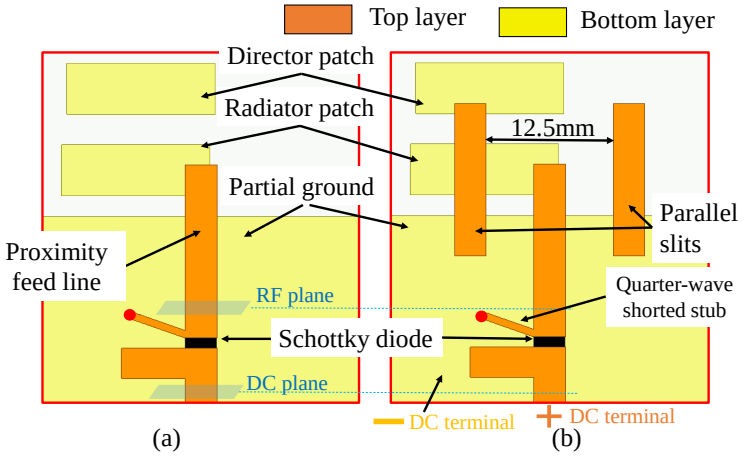

Figure 4.5: Evolution of the presented end-fire rectenna element (a) initial design without parallel slits (b) final design with parallel slits.

uniplanar end-fire microstrip antenna [132], however, this having complex feeding structure which is unsuitable for rectenna application. In contrast, the presented end-fire antenna

is a planar design with proximity feed excitation and utilizes dual-sides of the substrate for easy integration to be a rectenna element.

The performance of the end-fire radiator is analyzed in terms of impedance matching, gain, and 3-dB RF beamwidth. Initially, the end-fire rectenna element comprises a radiator patch and a director patch along with partial ground, all on the bottom layer, which is excited by a proximity feed line on the top layer, as depicted in Fig. 4.5 (a). The optimized initial design achieves RF gain of 4.8 dBi with 3-dB RF beamwidths of 70° and 120° in azimuth and elevation planes, respectively. However, the input impedance of the initial design is $Z_a = 40.83 + j73.25\ \Omega$ which is not conjugate matched with the Schottky diode impedance Z_d. To improve the RF-DC performance, two slits parallel to the proximity feed line are introduced on the top layer as shown in Fig. 4.5 (b) and their dimensions along with separation from the feed line are optimized to achieve conjugate matching. The comparison of impedance variations simulated at the RF plane for the designs, with and without slits, is presented in Fig. 4.6. The optimized impedance of the presented

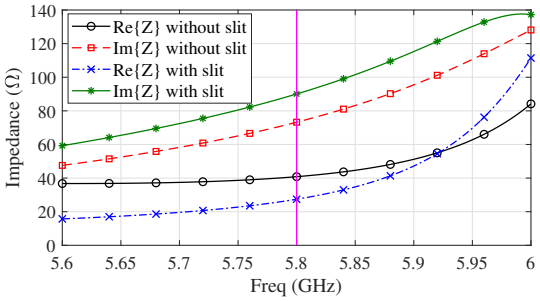

Figure 4.6: Conjugate matching of the end-fire antenna element with Z_d.

end-fire antenna is $Z_a = 25.83 + j90.89\ \Omega$, which is close to $\overline{Z_d}$. Though, the elevation RF beamwidth is a bit compromised to 117.06°, however, a better beamwidth in the azimuth (84.86°) along with an improved gain to 5.1 dBi is achieved as compared to the design without slits. The simulated RF patterns of the end-fire antenna are plotted in Fig. 4.7 (a).

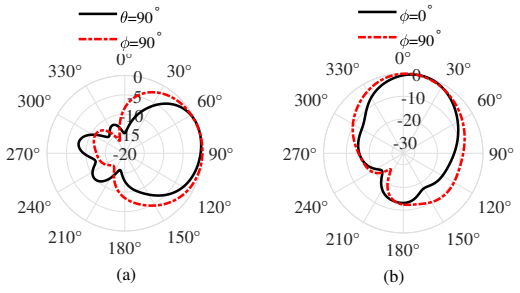

Figure 4.7: RF patterns of the presented (a) end-fire and (b) bore-sight antennas.

For the RF-DC rectification, the topology presented in Fig. 4.4 (b) in implemented for the end-fire element. Following this, a Schottky diode is mounted along the proximity feed-line and terminated to the DC connection line (+ive DC terminal) on the top layer, as depicted in Fig. 4.5 (b). A quarter-wave shorted stub is employed to connect the diode with the

partial ground at the bottom layer which functions as the -ive DC terminal. This stub is RF-open at the diode connection, thus, provides direct DC path to the ground. Further along the DC path of the end-fire rectenna element, the bore-sight element of the same sector is connected through DC-line, as shown in the inset of Fig. 4.3, which works as shunt capacitance imitating the DC-LPF to reject the higher-order harmonics. The bore-sight element is a 3×1 rectangular patch array (PA) antenna as described in detail in the subsequent section. The PA antenna has the inherent property of a low pass filter [133], removing the higher-order harmonics and improving the power conversion efficiency.

The presented end-fire rectenna element provides a wide simulated DC 3-dB beamwidth in the azimuth (57°) and elevation (87°) planes. Furthermore, the simulated DC patterns for the end-fire elements of all six-sectors are evaluated and plotted in Fig. 4.8 (a) for 360° azimuth angles. The result indicate that the overlapped DC patterns of the adjacent elements can nearly achieve a flat total DC pattern in the azimuth plane.

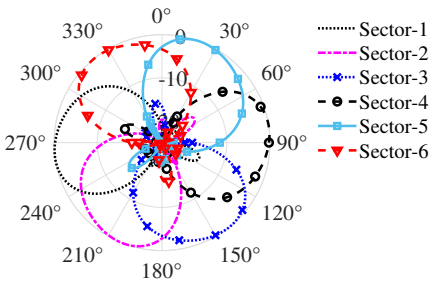

Figure 4.8: Simulated overlapped DC patterns of the end-fire rectennas in azimuth $\theta = 90°$ plane.

4.3.4 Bore-sight Rectenna Design

As a bore-sight element of a sector, a series-fed 3×1 rectangular patch array (PA) antenna is designed using meandered U-shaped feed lines to minimize the total size, as depicted in the inset of Fig. 4.2. The lengths of the meandered series feeds are optimized to provide a gradual phase shift between the patch elements. This enables the generation of tilted beam towards the feed point which is the radially outward direction in the elevation plane. This tilted-beam characteristic offers broader DC coverage in the upper hemispherical space in coordination with the other PA rectenna elements of other sectors. The simulated RF pattern of the presented bore-sight element is presented in Fig. 4.7 (b) indicating a beam-tilt of 15° with maximum gain of 6.4 dBi. The simualted 3-dB RF beamwidth coverage in the two orthogonal elevation cuts are 50.78° and 81.17°, respectively.

For rectification, the topology presented in Fig. 4.4 (c) is adopted in the bore-sight element. To implement an integrated rectifier circuit, initially a Schottky diode is affixed between the patch and the ground plane through a via pin, as depicted in Fig. 4.3. This approach is adopted in [133] for direct conjugate matching of a single patch antenna by discovering an optimal port location where the antenna impedance is close to $\overline{Z_d}$. However, this approach is not always applicable since the desired port impedance is not always achievable

on any arbitrary antenna structure. For instance, this method is unable to achieve a conjugate Z_d in the presented PA antenna while all the port locations have been tried in the optimization. This happens due to the low value of inductive reactance offered by the series-fed PA antenna structure. Thus, a different approach is applied in the presented PA rectenna design. First, by direct placement of diode, the best possible impedance of the antenna is achieved as $Z_a = 17.6 + j42.5\ \Omega$ not as such suitable for the conjugate matching with Z_d. In the next step, a semi-circular C-slot (annular ring) is cut in the patch element around the feeding point to enhance the inductive impedance and further optimized to achieve the desired impedance as $Z_a = 28.49 + j93.92\ \Omega$. The significance of the use of annular ring to achieve the desired impedance is demonstrated by the plots in Fig. 4.9. Additionally, since the patch antenna has an intrinsic low pass filter characteristic,

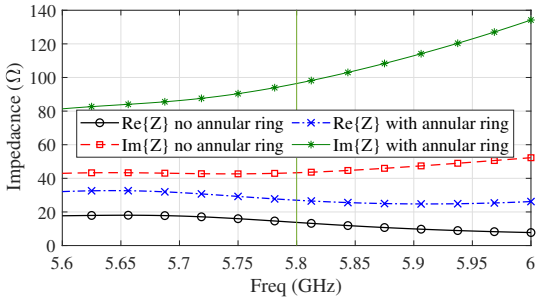

Figure 4.9: Conjugate matching of bore-sight PA antenna with Z_d.

hence, it assists in realizing a fully integrated rectification operation by imitating itself as the DC-LPF in the topology presented in Fig. 4.4 (c). The simulated DC patterns of the two opposite bore-sight rectenna elements (from Sector-1 and Sector-4) are plotted in Fig. 4.10 (a) depicting a better elevation coverage due to tilted beams. Moreover,

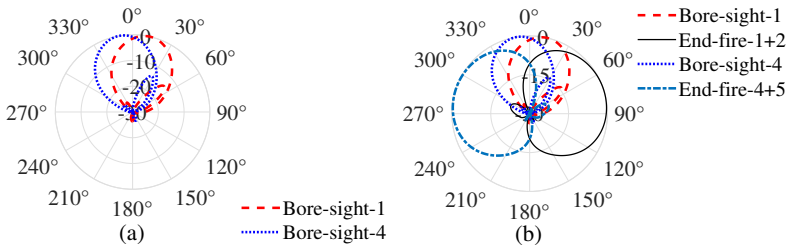

Figure 4.10: Simulated overlapped DC patterns of the opposite sectors (a) bore-sight rectennas (b) end-fire and bore-sight rectennas in the $\phi = 0°$ plane.

the elevation coverage is further enhanced by the end-fire rectennas together with the bore-sight elements and overall a better coverage in the entire 3D-spherical region can be obtained. This is demonstrated by plotting the simulated DC patterns of the opposite sectors in the elevation plane as shown in Fig. 4.10 (b).

4.3.5 Integration of Sectors and Rectenna Combining

The mutual coupling between both the radiators of a sector is analysed in Fig. 4.11 indicating an isolation of 56 dB achieved between the adjacent elements. This indicates

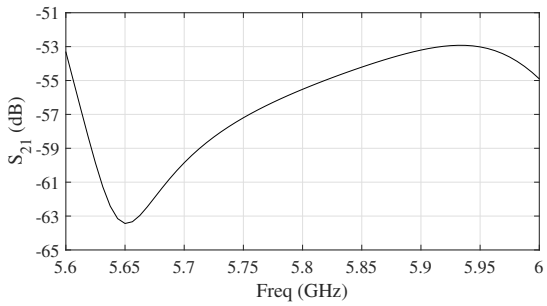

Figure 4.11: Mutual coupling between the adjacent rectenna elements.

that the end-fire and bore-sight radiators can operate independently without altering the characteristics of each other. The pair of rectenna elements are connected in parallel with a DC-line within the sector and the DC output of each sector is further combined using parallel combining technique on the PCB top layer as shown in Fig. 4.2. This parallel DC combining offers low connection losses as compared to the series combining technique [134, 135]. Moreover, bypassing circuit [44] across the non-active rectenna elements is not required since the corresponding rectifying diodes become reverse biased, which results the dc combining circuit as simple and easily realizable. The DC output is extracted from the center of the structure through output pin at the bottom as shown in Fig. 4.3 which, as a DC source, can be directly mounted on the IoT node for further utilization.

4.3.6 Experimental Validation of the H2B1 Design

The presented H2B1 is fabricated in the laboratory using a MITS PCB prototyping machine and the developed prototype with SMD assembly is shown in Fig. 4.12. The RF-DC efficiency and DC pattern measurements are carried out to validate the

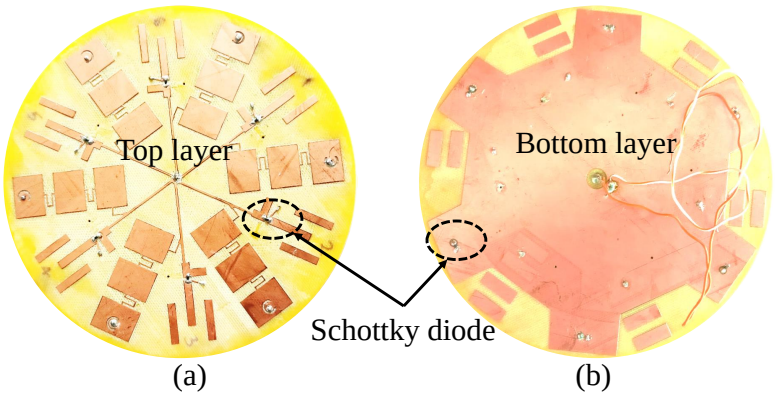

Figure 4.12: Fabricated prototype of the presented H2B1 (a) top, (b) bottom view.

performance under the laboratory setup.

4.3.7 Measurement Setup

The RF power is generated using a signal generator having maximum RF output of 25 dBm. The generated RF signal is fed into an 8.6 dBi gain horn antenna (Tx) using an RF cable having 3 dB loss. For the measurements a maximum of 25 dBm RF power is considered due to the unavailability of RF power amplifier in the laboratory. The presented H2B1 is affixed on an automated turn table at 1 m distance away from the Tx antenna as shown in Fig. 4.13. The received power at the rectenna aperture is measured

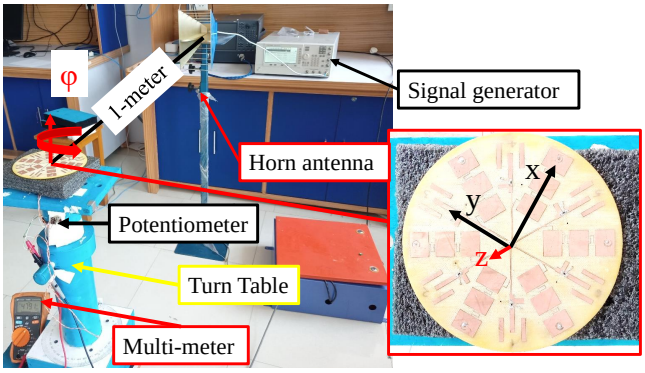

Figure 4.13: Measurement setup for harvested DC pattern in $\theta = 90°$ plane of the presented H2B1 using horizontally polarized Tx.

using the Keysight N9951A spectrum analyzer and the harvested DC voltage is measured using the Keysight U1232A multi-meter. For the H2B1 placed horizontally in the xoy ($\theta = 90°$) plane, the E-field polarization of the end-fire rectenna is along angular direction, whereas, it is along radial direction for the PA rectenna. This implies that harvested voltage in $\theta = 90°$ plane is only contributed by the end-fire rectenna elements. Therefore, voltage measurement in the $\theta = 90°$ plane is carried out by mounting the Tx in horizontal polarization as depicted in Fig. 4.13. In contrast, the total harvested voltage in the elevation plane is the combination of the voltage harvested by the end-fire as well as the PA rectenna elements. Thus, both horizontal and vertical orientations of the Tx are utilized for voltage measurements in the elevation plane ($\phi = 0°$ and $\phi = 30°$). The measurement setup with vertically polarized Tx is illustrated in Fig. 4.14 where the H2B1 is placed vertically for elevation pattern measurements.
Although, the measurements can be performed by using a circularly polarized Tx antenna. However, due to resource constraints in the laboratory, the measurement for both the polarization are carried out separately.

4.3.8 RF-DC Efficiency versus Load Measurement

The harvested DC voltage is measured across the potentiometer (500 Ω – 1.5 $k\Omega$) to determine the optimal load and the RF-DC conversion efficiency (η_{RF-DC}). The rectified dc power (P_{dc}) is measurement procedure is given in section 2.1.2.
The realised gain of the rectenna cannot be measured using a standard 50 Ω port because the antenna is fully integrated with the rectifier circuit. The realized gain and the

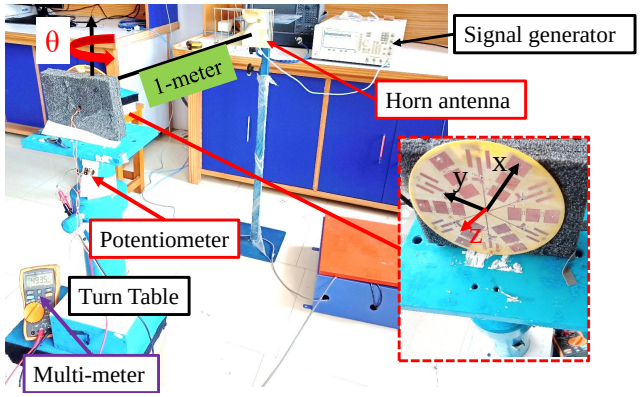

Figure 4.14: Measurement setup for harvested DC pattern in $\phi = 0°$ and $\phi = 30°$ plane of the H2B1 using a vertically and horizontally polarized Tx.

impedance matching efficiency of the complete rectenna are obtained by simulations using the Ansys HFSS and ADS jointly.

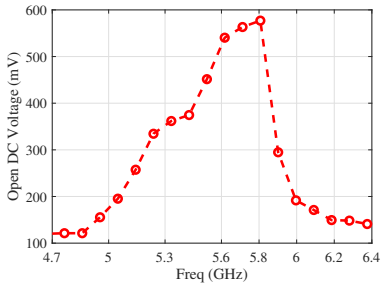

Figure 4.15: Open DC voltage of the presented H2B1 WPT system.

Moreover, S-parameter measurement is not possible in the fully integrated WPT system having only DC output port. Therefore, the operating frequency of the presented WPT system is investigated by measuring the open DC voltage versus signal frequency in Fig. 4.15. The maximum DC voltage is observed at 5.8 GHz. This measurement is conducted for both the individual rectenna elements separately. The harvested DC voltage and evaluated η_{RF-DC} are plotted against varying load in Fig. 4.16 (a) and (b) respectively for the end-fire and the PA rectennas. The results indicate that a maximum η_{RF-DC} of

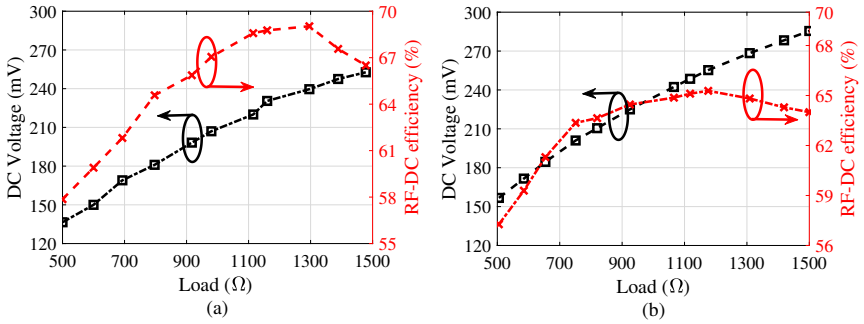

Figure 4.16: RF-DC conversion efficiency and harvested voltage versus output load for (a) end-fire rectenna, and (b) bore-sight PA rectenna.

69.1% is achieved at $\sim 1280\ \Omega$ for the end-fire rectenna, whereas, the PA rectenna has the

maximum efficiency of 65.28% for an output load value 1176 Ω. The RF-DC efficiency and

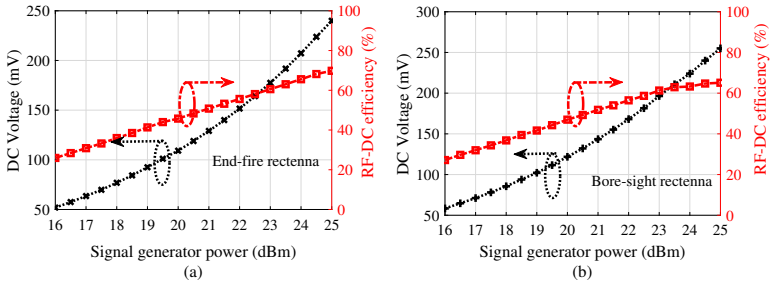

Figure 4.17: RF-DC conversion efficiency and harvested voltage versus Signal generator power for (a) end-fire rectenna, and (b) bore-sight PA rectenna.

harvested voltage of end-fire and bore-sight rectennas are measured for varying transmitted power shown in Fig. 4.17 (a) and (b). In the presence of output load, the former harvest $\sim$ 240 mV at 1280 Ω load, whereas the latter harvests $\sim$ 255 mV at the 1176 Ω load. Moreover, for an open DC measurement, the end-fire and bore-sight rectennas harvest maximum open output DC voltage of 515 mV and 580 mV, respectively.

4.3.9 DC Pattern Measurements

The harvested DC voltage pattern of the H2B1 is measured by rotating the turn table with a step size of 5°. At first, the DC patterns of the individual end-fire and bore-sight PA rectennas are measured separately and results are plotted in Fig. 4.18 and Fig. 4.19, respectively. The results show good agreement between the simulated and measured

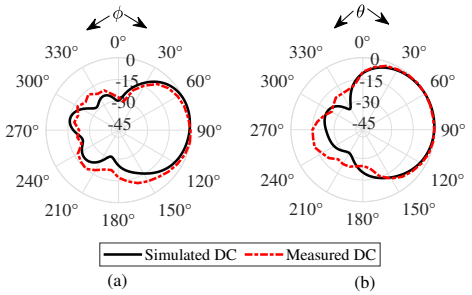

Figure 4.18: Normalized simulated and measured DC patterns of the end-fire rectenna element in (a) azimuth $\theta = 90°$ and (b) elevation plane.

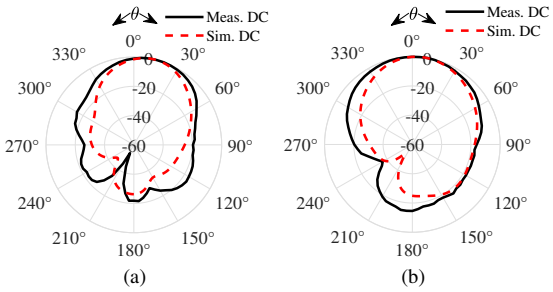

Figure 4.19: Normalized simulated and measured DC patterns of the bore-sight rectenna element in the elevation planes (a) $\phi = 0°$ and (b) $\phi = 90°$.

values particularly around the beam maxima region. The DC patterns of the H2B1 are measured using the setups illustrated in Fig. 4.13 and Fig. 4.14 using horizontally and vertically polarized Tx antennas. For horizontally polarized Tx, the measured DC pattern in $\theta = 90°$ plane is nearly omnidirectional as shown in Fig. 4.20(a), depicting good angular misalignment tolerance achieved by end-fire rectenna array elements in the azimuth. The measured DC patterns in $\phi = 0°$ and $\phi = 30°$ elevation planes for horizontally polarized Tx is directional having a 3 dB beamwidth of $\sim 78°$ in the bore-sight direction as demonstrated in Fig. 4.20 (b) and Fig. 4.20 (c), respectively. This is due to the cross-polarized alignment of the Tx with the end-fire elements while a co-polarized alignment exist with the bore-sight elements, thus, end-fire elements are unable to harvest from the cross-polarized Tx in a planar design.

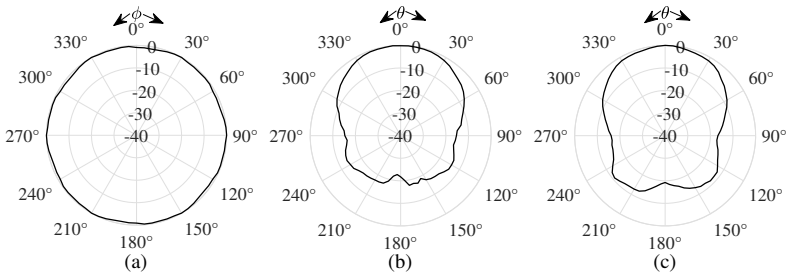

Figure 4.20: Normalized DC voltage patterns in (a) $\theta = 90°$, (b) $\phi = 0°$, and (c) $\phi = 30°$ planes for horizontally polarized Tx

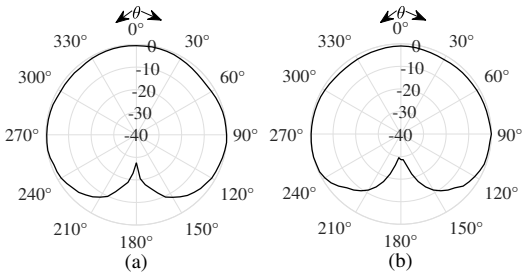

Figure 4.21: Normalized DC voltage patterns in (a) $\phi = 0°$, and (b) $\phi = 30°$ planes for vertically polarized Tx

Similarly, for the vertically polarized Tx, the dc patterns are illustrated in Fig. 4.21 where both, the end-fire as well as the bore-sight, elements harvest the RF originating from the vertically polarized Tx. Fig. 4.21 (a) plotted for $\phi = 0°$ and $\phi = 30°$ plane offer a uniform coverage in the 3D-spherical region. The measured results indicate that the presented H2B1 achieves good tolerance against the orientation misalignment with respect to the Tx. However, this design has large dimensions, making it limited design for small IoT applications. Therefore, a compact, high-performance WPT system is designed in the section 4.4.

4.4 H2B2: A compact design for 3D-spherical Coverage.

The presented H2B2 WPT system is designed on a dual-sided 35 μm copper cladded FR4 substrate having 1.5 mm thickness with dielectric constant $\epsilon_r = 4.4$ and loss tangent

$\tan\delta = 0.02$ using Ansys HFSS and ADS software at 5.2 GHz. The enlarged view of the top and bottom layer of the presented H2B2 WPT system is shown in Fig. 4.22 (a), (b) and dimensional parameters are mentioned in Table. 4.2. The presented H2B2 WPT system design comprises eight radially placed End-Fire Rectennas (EFRs) in Region-1 and one Bore-Sight Rectenna (BSR) placed at the center in Region-2 as marked in Fig. 4.22.

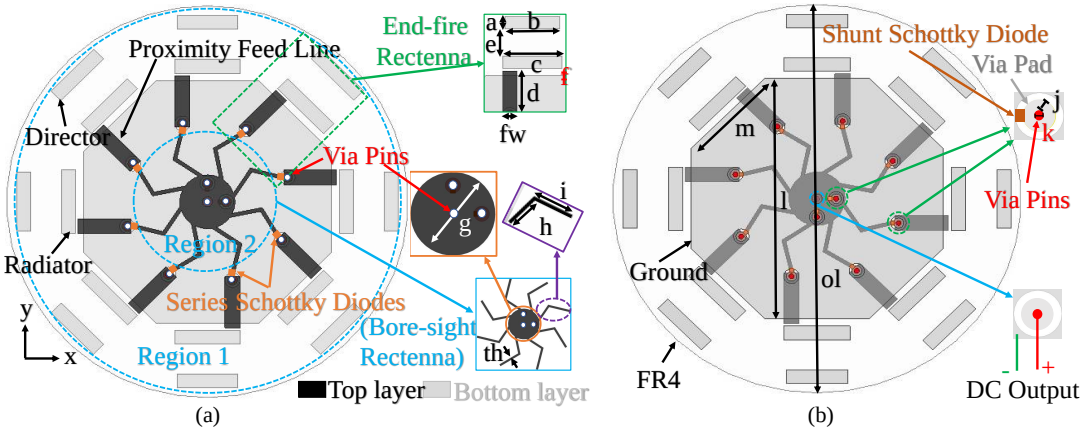

Figure 4.22: Layout of the presented H2B2 WPT system.

Table 4.2: Dimensional parameters of the proposed rectenna

Parameters	a	b	c	d	e	f	fw	g	h	i	th	j	k	l	m	ol
Dimensions (mm)	2.8	12	13	10.5	6.2	1.5	3	11	6.09	5.28	0.3	1	0.25	46.2	19.13	74

Each EFR-antenna of Region-1 comprises a single proximity feed line, a radiator, a director, and a reflector ground plane. The evolution of the proposed EFR-antenna is influenced by uniplanar microstrip EFR-antennas [132, 136], however, these designs have narrow beam-width and feature complex feeding arrangements, making them unsuitable for WPT applications. Therefore, a novel proximity feeding simple structure is designed to achieve an end-fire beam pattern and easy integration with a shunt-series Schottky diode for RF-DC conversion. In addition, the EFR-antenna achieved high isolation of 44 dB and 35 dB between adjacent and radially opposite elements, as demonstrated in the mutual coupling plots of Fig. 4.23. The optimized EFR-antenna element offers 5 dBi gain with

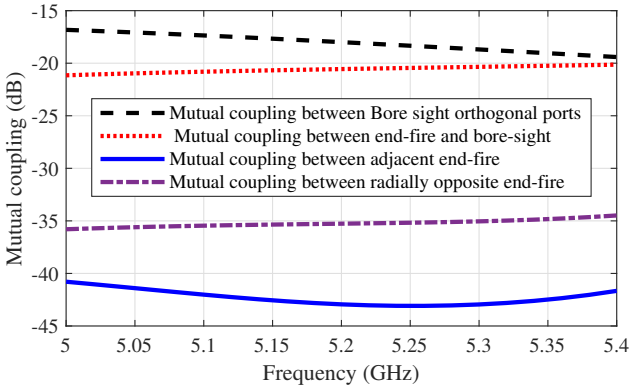

Figure 4.23: Mutual coupling between different ports of the proposed rectenna.

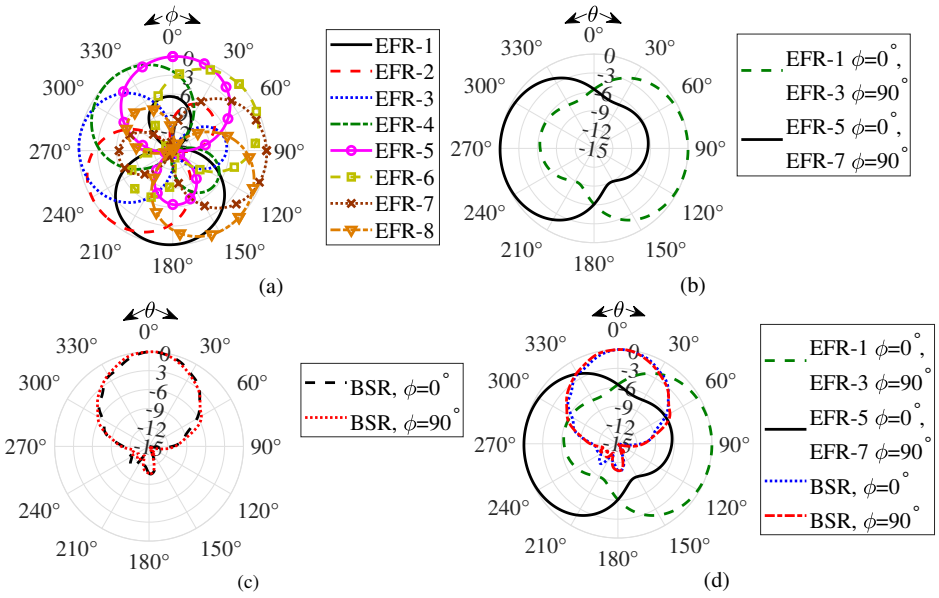

Figure 4.24: RF radiation pattern for (a) eight EFR-antenna elements showing azimuth patterns, (b) radially opposite EFR-antenna elements showing elevation patterns, (c) BSR-antenna elevation pattern, and (d) two radially opposite EFR-antenna with BSR-antenna showing elevation plane patterns.

3-dB RF beamwidth of 92.8° in the azimuth and 137.4° in the elevation plane, as illustrated by the simulated RF patterns plotted in Fig. 4.24 (a) and Fig. 4.24 (b), respectively. The overlapped azimuth RF coverage of EFR elements in Fig. 4.24 (a) provides intuition for overall flat coverage, however, the DC coverage is essentially investigated to validate the actually achieved uniformity post DC-combining. In Region-2 of the proposed design, a novel multi-arms circular patch is designed as the BSR-antenna also imitating as DC combiner circuit. This antenna has eight arms connected with a central patch which are optimized to provide wider beam-width in the elevation plane. In addition, the eight-arms working as DC-lines provide easy integration with the EFR elements using a series Schottky diode achieving an isolation of 21 dB (Fig. 4.23). Further, dual linear polarization in the *xoy* plane is achieved on the patch by optimizing the two orthogonal ports each having independent rectification and having good isolation of 17 dB. The BSR-antenna has RF gain similar to the EFR-antenna element with 3-dB RF beamwidth of 78° in $\phi = 0°$ and 80° in $\phi = 90°$ elevation plane as shown in Fig. 4.24 (c). To analyze the elevation coverage forming, the simulated combined RF pattern of two radially opposite EFR-antenna and BSR-antenna plotted in Fig. 4.24 (d) illustrates that enhanced 3D spherical coverage can be achieved by combining the EFR and BSR elements. A further description of direct impedance matching, integration of rectenna elements, and their equivalent circuit is provided in the subsection 4.4.1.

4.4.1 Direct Matching and Rectifier Integration

The maximum RF-DC conversion efficiency is achieved by designing an antenna at input impedance equal to the complex conjugate of the Schottky diode impedance. Therefore,

conventionally in rectenna designs, distributed impedance matching network (IMN) is utilized for transforming rectifier input impedance to the receiver antenna input impedance (50 Ω) [34], and a DC-low pass filter (DC-LPF) is employed for eliminating higher-order harmonics. However, the distributed IMN and DC-LPF circuits cause insertion losses and hinder rectenna miniaturization. Therefore, an integrated rectenna with direct conjugate matching with the Schottky diode is introduced [133] for single element to overcome the immediately mentioned problems.

For designing an integrated rectenna array system, direct matching requires a new judicious approach and topology for joint integration of matching + rectification + DC combining. First, the LSSP and harmonic balance (HB) technique in Keysight ADS software are utilized to evaluate the impedance of the Schottky diode at 5.2 GHz. The rectifier circuit input impedance Z_d is evaluated for both the EFR-antenna and BSR-antenna. The evaluated input impedance at -10 dBm input power level and output load of 1100 Ω is $Z_d = 15.625 - j57.964$ Ω for EFR-antenna and $Z_d = 24.004 - j91.66$ Ω for BSR-antenna. The desired input impedance equal to $\overline{Z}_d$ for conjugate matching is achieved by optimizing feed location where the rectifying diodes are mounted and design parameters for the EFR and BSR antennas.

The proposed topology for integration of the EFR-antenna and BSR-antenna elements with Schottky diodes is illustrated in Fig. 4.25. The EFR-antenna is conjugate impedance

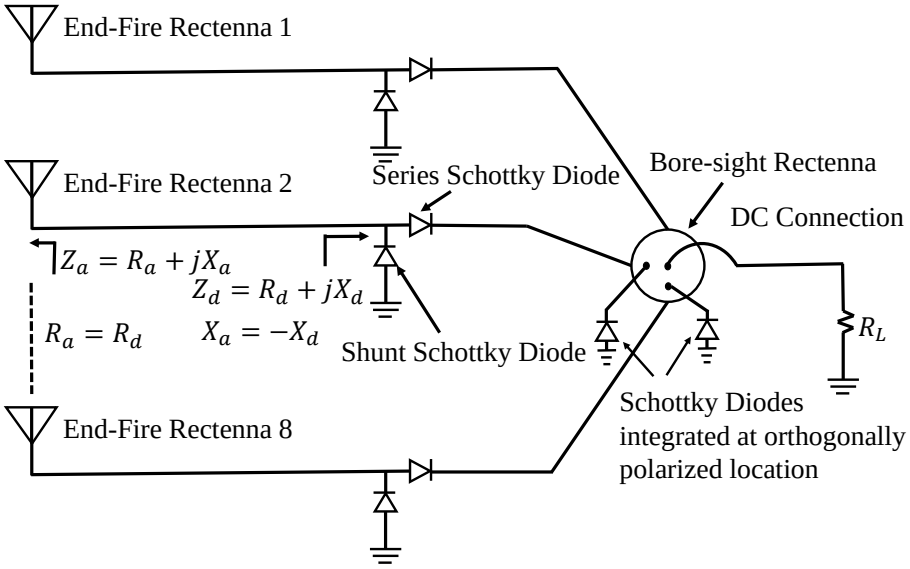

Figure 4.25: Proposed topology for integrated WPT system without IMN and DC-LPF.

matched with the shunt and series diode to harvest DC power. Similarly, the BSR-antenna is conjugate matched with two orthogonally positioned shunt Schottky diodes to harvest DC power from any orientation in the xoy plane. Further, the integrated EFR and BSR have inherent low pass filter [133], therefore, it obliges to realize a completely integrated rectenna circuit by mimicking itself as the DC-LPF in the topology presented in Fig. 4.25. Moreover, as shown in Fig. 4.25, the proposed BSR-antenna element in Region-2 through its multi-arms imitates the inherent DC combiner circuit to evolve a completely integrated

RF-DC system. The proposed system DC output emanates from the BSR center point, because this has evidently low voltage potential. Therefore, this point can be picked as the one DC terminal through via pin without impairing impedance matching and radiation pattern performance of the presented H2B2 WPT system. On the other hand, the common ground plane acts as the second DC terminal as shown in Fig. 4.22. To explain the working principle and integration approach of the proposed design, an equivalent circuit is illustrated in Fig. 4.26. The circuit diagram demonstrates that direct connection of the

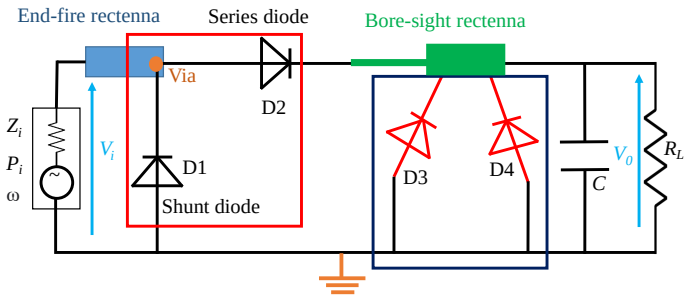

Figure 4.26: Equivalent circuit of the presented H2B2 WPT system.

EFR and the BSR in RF domain is not feasible as it results in increased mutual coupling between both the antenna elements. Moreover, it changes the electrical length of the antennas, causing impedance mismatch and radiation pattern distortion, which results in lower RF-DC conversion efficiency. To address the above-mentioned issue, an RF choke is recommended [137] using a high-value inductor (in place of D2 series diode). Although, an inductor can block RF power and provides DC connection without affecting the antenna electrical length. However, it increases circuit losses [2] and cannot stop the DC current backflow during the negative half cycle of RF signal [107] thus unable to provide a complete RF isolation between Region-1 and Region-2.

Therefore, to facilitate a proper DC connection between the EFR and BSR elements, series Schottky diodes are used in the proposed design, which provides high isolation and limits the backflow of DC current during the negative cycle of RF signal. In the topology implemented in Fig. 4.25 with the circuit illustrated in Fig. 4.26, the shunt diode (D1) becomes reverse biased (open) during the positive half cycle of the RF signal impinging from the endfire direction, and passes the DC current from the series diode (D2) which is forward biased. While during the negative half-cycle, D1 is forward biased whereas D2 is reverse biased, which prevents the back flow of the DC into the EFR. This connection of the two diodes D1 and D2 is complementing each other and can contribute to overall voltage enhancement [138, 139] for the EFR. Further, the Schottky diodes D3 and D4 are shunt connected with the BSR to provide rectified DC output from two orthogonal polarisation during the positive half cycle of the RF signal impinging from the broadside direction. The DC output collected from the center of the BSR is fed to the load R_L.

4.4.2 Simulated DC Pattern Results

The simulated harvested DC pattern of the EFR and BSR post rectification are depicted in Fig. 4.27. The simulated DC pattern is compared to the simulated RF pattern, and actual performance is used as a reference to illustate the combined rectenna performance. This is evaluated using co-simulation technique using Ansys HFSS, and keysight ADS with considering circuit losses. The EFR has 3-dB DC beamwidth of 67° in the azimuth plane. Therefore, the radial combination of eight EFR elements can achieve uniform DC

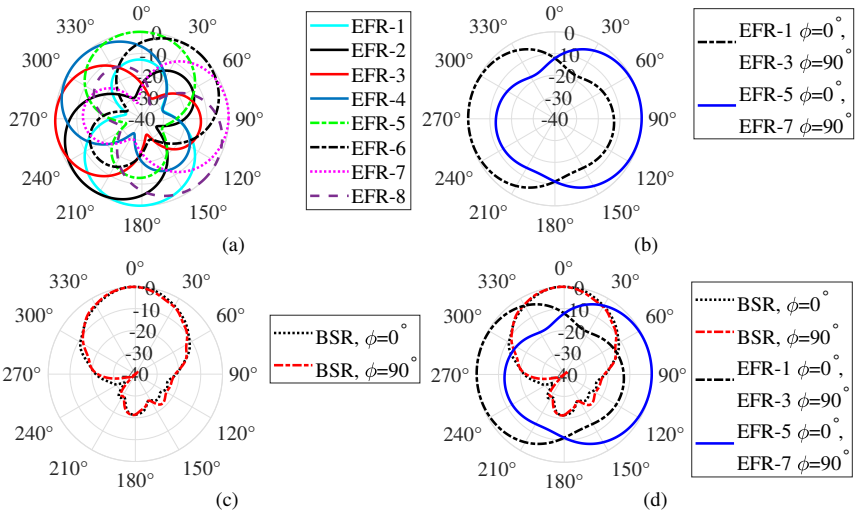

Figure 4.27: Simulated DC patterns for (a) eight EFR elements to cover azimuth plane, (b) elevation plane pattern of EFR (c) BSR in elevation plane, and (d) two radially opposite EFR with BSR to cover elevation plane.

beam coverage in the entire azimuth plane, as illustrated in Fig. 4.27 (a). In addition, this offers a good 3-dB DC beamwidth coverage (118°) in the elevation plane, as shown in Fig. 4.27 (b). The simulated DC patterns for BSR in the elevation plane have a 3-dB beamwidth of 54° as shown in Fig. 4.27 (c), which in coordination with the EFR elements, are expected to enhance the uniformity in 3-D spherical coverage, as demonstrated in Fig. 4.27 (d). The measurement results to validate the presented H2B2 WPT system are presented in section 4.4.3.

4.4.3 Fabricated Prototype

The presented H2B2 WPT system is fabricated on the FR4 substrate using the MITS PCB prototype machine to validate simulation results. The final fabricated prototype with mounted diodes is shown in Fig. 4.28. The RF-DC conversion efficiency and DC voltage pattern measurements are carried out in an anechoic chamber. The measurement of RF characteristics, such as S_{11}, impedance, and RF radiation pattern, of a single antenna, consisted in the fully assembled integrated rectenna, is not possible. However, to determine the performance of the presented H2B2 WPT system, a measurement of harvested open DC voltage is performed. The measurement setup employs a signal generator to emanate 25 dBm of RF power through an 8.6 dBi gain horn antenna (Tx), where 1 dB cable

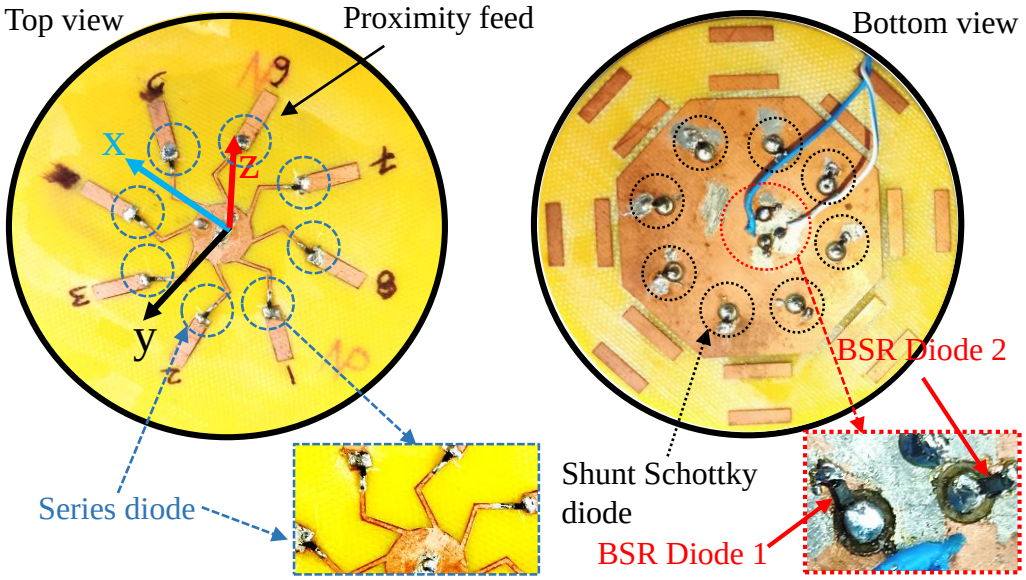

Figure 4.28: Fabricated prototype of the presented H2B2 WPT system.

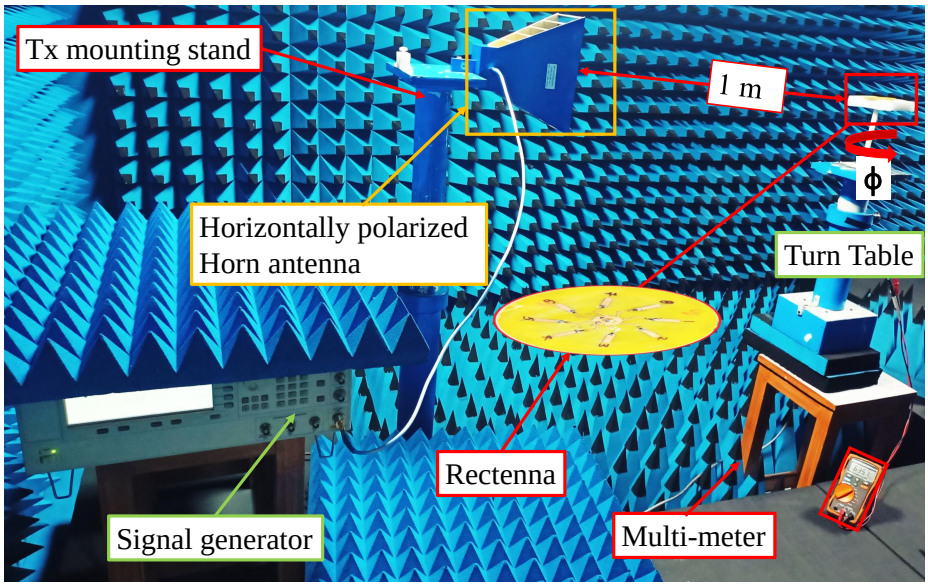

Figure 4.29: Measurement setup for harvested DC pattern in $\theta = 90°$ plane of presented H2B2 WPT system.

losses is considered. The rectenna is mounted on a rotating turn table positioned at 1 m distance from the Tx, as illustrated in Fig. 4.30. The harvested output DC voltage (V_{dc}) is measured using a Keysight U1232A multimeter across the optimal load. The 3D coverage performance of the proposed rectenna is determined by measuring DC power patterns in the azimuth ($\theta = 90°$) and elevation planes ($\phi = 0°$ and $90°$). The dc pattern measurement in $\theta = 90°$ plane is done by placing Tx in horizontal polarization as shown in Fig. 4.29 whereas for $\phi = 0°$ and $\phi = 90°$ planes the dc patterns are measured individually for both vertical as well as horizontal polarized Tx as depicted in Fig. 4.30 and Fig. 4.31, respectively. A circular polarized Tx can be employed for the measurements, however, the proposed measurement scheme is adopted due to resource constraints in the laboratory.

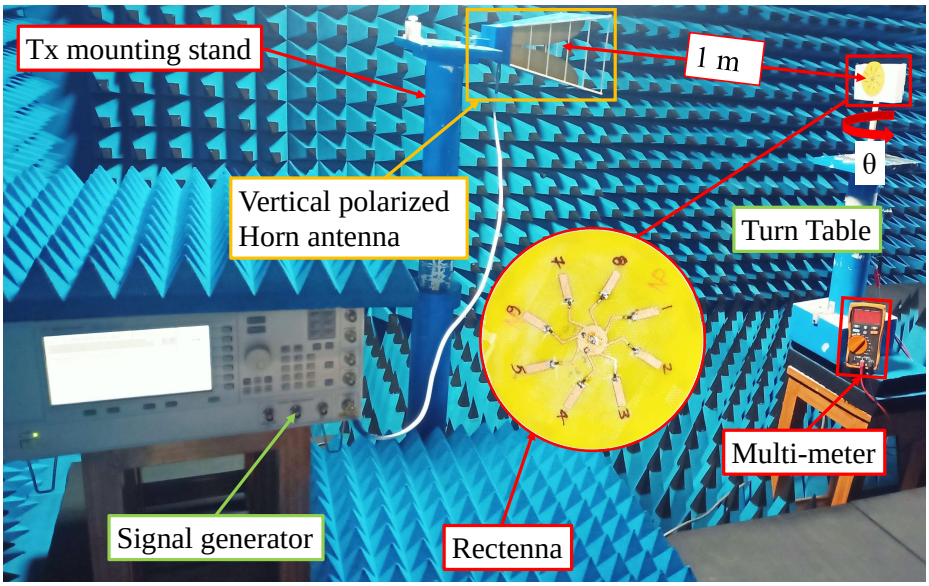

Figure 4.30: Measurement setup with vertical polarized Tx antenna.

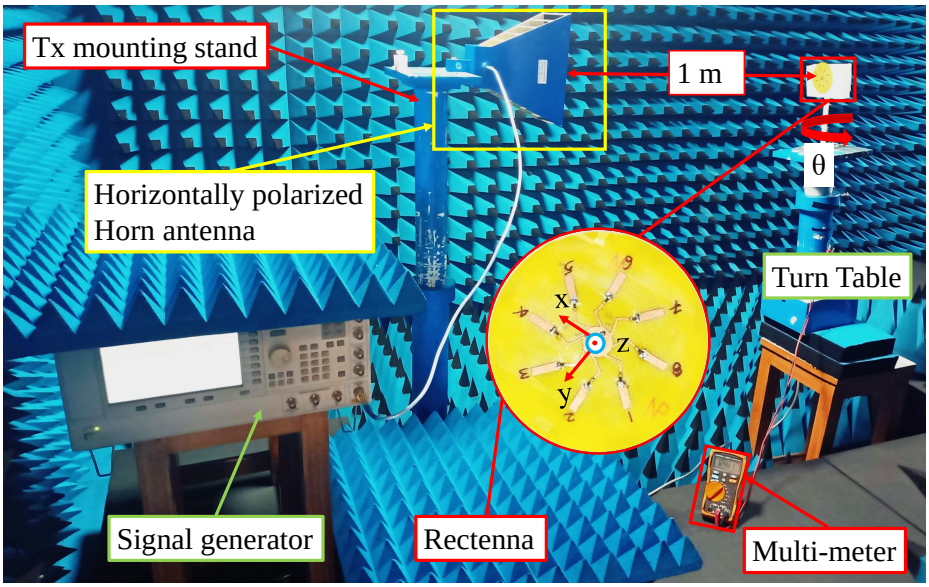

Figure 4.31: Measurement setup with horizontal polarized Tx antenna.

The measured DC power pattern of the presented H2B2 WPT system in $\theta = 90°$ using horizontal polarized Tx is depicted in Fig. 4.32 (a), which is in good agreement with the simulated DC power pattern illustrated in Fig. 4.27 (a) showing uniformity. Further, DC patterns measured in $\phi = 0°$ and $90°$ planes using horizontal and vertical polarized Tx are shown in Fig. 4.32 (b) and Fig. 4.32 (c), respectively. The DC patterns measured using horizontal polarized Tx will correspond to the BSR patterns in the elevation planes since the EFR elements are in cross-polarization. The measured 3 dB DC pattern beamwidth is 85° and 94° in $\phi = 0°$ and $90°$ planes, respectively. The vertical Tx measurement setup offers a hybrid DC pattern, which is the combination of the DC power harvested by the EFR and the BSR. The measured DC pattern illustrated in Fig. 4.32 (c) show that coverage of 200° is achieved in the elevation plane, which is in good agreement with the

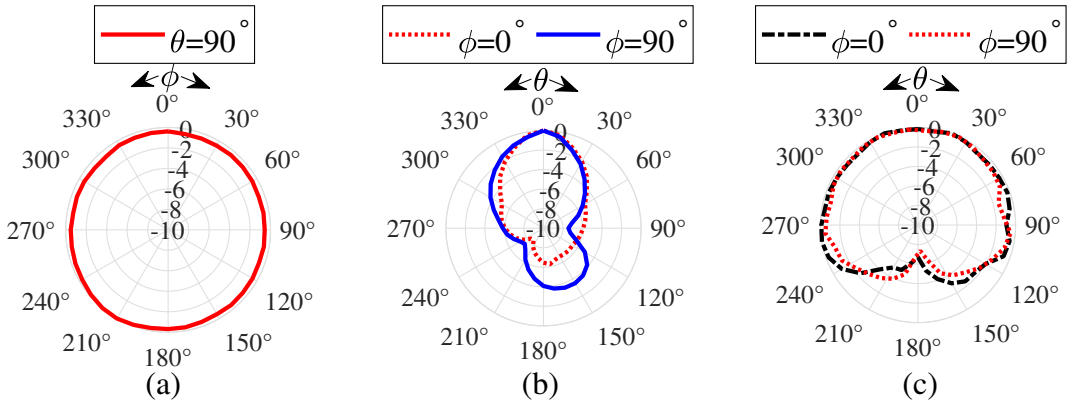

Figure 4.32: Normalized (a) measured DC pattern in $\theta = 90°$ plane, (b) $\phi = 0°$, and 90° planes for horizontally polarized Tx, and (c) $\phi = 0°$ and 90° planes for vertically polarized Tx

simulated DC patterns.

4.4.4 RF-DC efficiency

The RF-DC conversion efficiency (η_{RF-DC}) of both the EFR and BSR is evaluated separately using a variable potentiometer (600 Ω – 2600 Ω) and plotted in Fig. 4.33. The

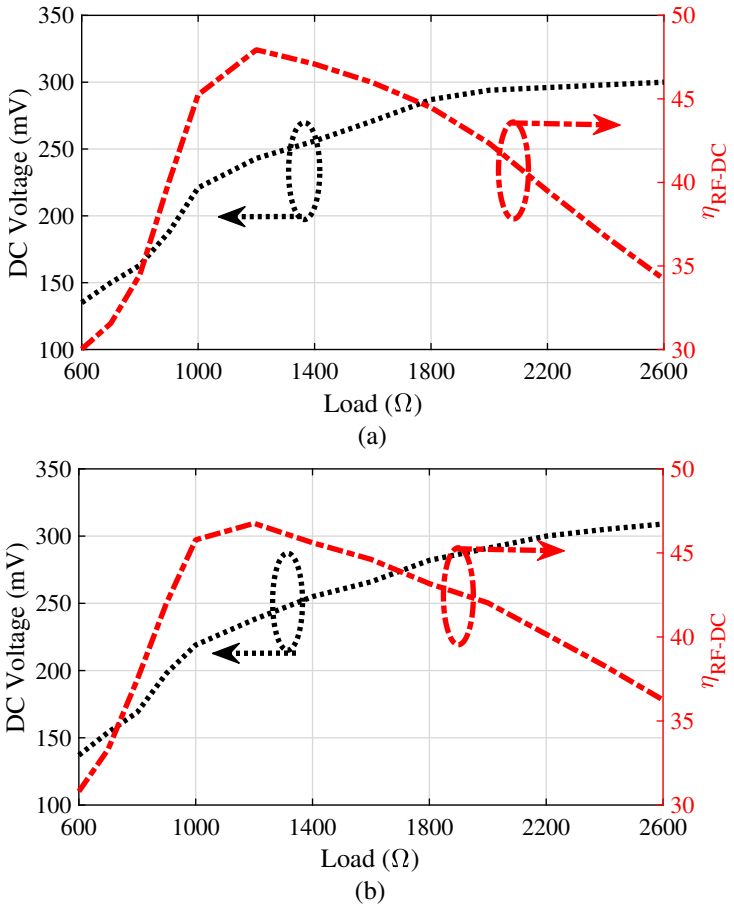

Figure 4.33: Measured efficiency and harvested dc voltage with respect to output load for (a) EFR, and (b) BSR.

maximum η_{RF-DC} obtained for the EFR is 48.47% with the optimal load of 1150 Ω, and 47.32% is achieved for the BSR with an optimal load of 1200 Ω. Moreover, the maximum harvested open DC voltage of 600 mV is achieved for the presented H2B2 WPT system.The proposed EFR and BSR systems receive RF power level of -9.75 dBm to -10 dBm. The proposed end-fire and bore-sight rectenna element performance is analyzed in the presence of load. The end-fire rectenna offer ∼ 243 mV at 1150 Ω and bore-sight radiator provides ∼ 238 mV at the 1200 Ω optimal load. The harvested DC power is sufficient to recharge low-power IoT devices used in smart home monitoring and automation applications. Moreover, the presented H2B2 WPT system can also be employed to recharge sensor nodes in industrial applications such as gas, liquid, smoke, and air pollution detection systems placed at any arbitrary location or orientation with respect to the Tx.

4.5 Performance Comparison with Prior Arts

The performance of the state-of-the-art 3D coverage rectennas with the proposed 3D coverage rectenna are shown in Table. 4.3. To achieve spherical coverage, in [28] a 3-D

Table 4.3: comparison with state-of-the-art designs for 3D-Spherical DC Coverage

	Frequency (GHz)	Beams	Sectors	port	size (mm^3)	Beam mechanism	Uniform 3D Coverage	η_{rf-dc} (%)
[28]	2.45	20	5	20	130 × 130 × 290	butler matrix	No	45 at −5 dBm
[140]	3.3 − 5.9	Omni	10	4	152 × 152 × 69.724	Complex	No	−−
H2B1	5.8	Omni	6	12	130 × 130 × 1.56	simple	Yes	69.1% (End-fire) 65.28% (Bore-sight)
H2B2	5.2	Omni	8	10	74 × 74 × 1.57	simple	Yes	∼ 47 − 49 at −10 dBm

structure five sector rectenna array is proposed with each sector generating 4 beams in elevation plane utilizing a 4 port BFN. Although the elevation coverage is enhanced, there is no beam along the axial direction. In addition, BFN is a bulky structure and hence unsuitable for miniaturized sensor nodes. Further, the harvested dc pattern in the azimuth plane is not uniform and hence does not mitigate the angular misalignment problem. In [140], a multi-element 3-D design with omnidirectional pattern in azimuth plane and elevation beams is presented to harvest RF power from the ambient and dedicated sources. The omnidirectional beams capture ambient RF energy whereas the bore-sight components capture RF power from dedicated source to satisfy high-power requirements. However, because of the high design complexity it is inappropriate for small IoT nodes. Moreover, a complete system with rectifier circuits is not implemented, hence no realistic RF-DC efficiency and DC power measurements are conducted. The radiation patterns show more than 5 dB decrease in RF power in the overlapping region of elevation and azimuth beams which confirms that 3-D spherical coverage can not be achieved using this design. The presented H2B1, and H2B2 WPT systems provides uniform DC coverage in the azimuth and elevation plane with high efficiency as compared to the state-of-the-art designs. Furthermore, the H2B1 WPT system is 180.257 % and 60.1 % miniaturized in terms

of volume compared to the designs presented in [28] and [140], respectively, making it suitable for deployment at space-constrained IoT sensor nodes.

4.6 Summary

This chapter presents, two novel planar 3D spherical coverage rectenna array for wireless energy harvesting applications. The H2B1 WPT system proposed fully integrated design with no requirement for a matching network and DC-low pass filters, which reduce insertion losses and system size as compared to conventional rectenna designs. Each sector of the proposed rectenna array comprises an end-fire element and a bore-sight 3×1 series fed patch array element. The antenna elements are integrated with the Schottky diode through the metallic via in the ground plane, and an annular ring is introduced in the patch antenna to achieve conjugate matching. The end-fire rectenna element offers 5.1 dBi gain with a simulated broader DC beam width of 57° and 87° in the azimuth and elevation plane, respectively. The end-fire rectenna provides an essentially flat DC power pattern in entire 360° with a 69.14% RF-DC conversion efficiency at an optimal load of 1280 Ω. The 3×1 series fed patch array has a 6.4 dBi gain, 65.28 % RF-DC efficiency at 1176 Ω load, and a 15° tilt from the boresight direction in radially outward direction. The later design (H2B2) proposed, a novel planar eight-sector 3D spherical coverage rectenna array for wireless energy harvesting applications. The proposed system is a fully integrated low-profile design that eliminates the need for a matching network and DC-low pass filter. This results in reduced insertion losses and a smaller footprint as compared to the conventional rectenna systems. The proposed rectenna array has an end-fire element in each sector, and a bore-sight element is placed at the center. The end-fire rectenna element has a gain of 5 dBi and a simulated harvested DC pattern beam width of 67° and 118° in the azimuth and elevation planes, respectively. Therefore, the combination of 8 end-fire sectors offers an omnidirectional DC pattern in the azimuth plane, and each element provides 48.47 % RF-DC efficiency at 1150 Ω. Further, the novel bore-sight element proffers 54° DC beam coverage in the elevation plane and achieve 47.32 % RF-DC efficiency at 1200 Ω output load. Additionally, the proposed WPT rectenna elements offer better 3-D spherical coverage for charging sensor nodes with arbitrary orientations in the smart environment. However, the proposed system does not fulfill the diverse power requirements. Therefore, a scalable WPT system with 3D-spherical coverage is presented in Chapter 5 to fulfill the diverse power requirements.

Chapter 5

On Demand and Scalable Rectenna System

5.1 Introduction

The previous chapter presented a 3D-spherical coverage RF power harvesting system, which provides uniform power harvesting in dual planes. However, various nodes may have diverse power requirements and size constraints for different application scenarios. Therefore, this chapter presents a plug-in type rectenna unit cell to fulfill the dynamic power requirements by offering an on-demand and scalable rectenna WPT system. The WPT-enabled nodes (Rx) convert the RF power into DC power using a rectenna module [141], which is sensitive to Rx orientation and RF power density. This necessitates an innovative design with polarization-insensitive [56, 57, 58] and dynamic power harvesting [59] capabilities along with miniaturization [142, 123]. To target these requirements, a few scalable and orientation-insensitive WPT systems are reported in literature with multi-port [60], multi-beam [45], differential fed [61], and meta-material antennas [64]. For instance, in the application scenario exemplified in Fig. 5.1, the RF

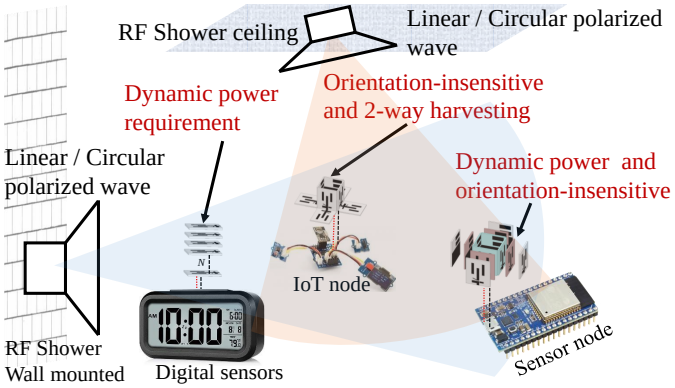

Figure 5.1: Application scenario of the scalable plug-in WPT system.

showers can be mounted on wall and ceiling with linearly or circularly polarized Tx antennas. Here, some sensors and IoT nodes demand different battery capacity with size constraints and some nodes have varying orientations whereas the others are exposed to horizontal as well as vertical impinging RF waves. Hence, a diverse RF battery requirements exist. Foremost, the available designs lack that kind of scalability feature which allows the WPT systems to easily adapt to these requirements. The immediately mentioned requirements motivated the presented work and a plug-in type rectenna module is demonstrated with following significant contributions:

- The H3C1 rectenna act as a unit cell for a scalable RF battery capable of adopting different geometrical formations according to the application scenario requirements,
- A novel integrated end-fire rectenna is presented with a compact footprint and high gain with better rectification capabilities,
- The plug-in rectenna module meets the orientation-insensitive and dynamic power harvesting requirements by incorporating different geometrical shapes.

5.2 H3C1: Plug-in Type Integrated Rectenna Cell Design

The H3C1 rectenna cell is presented for 5.8 GHz WPT system using the commercial ANSYS HFSS-2020-R1 on a double-sided low-cost FR4 substrate ($\epsilon_r = 4.4$, $\tan\delta = 0.002$) having 1.565 mm thickness and 35 μm copper deposition. The H3C1 rectenna layout is illustrated in Fig. 5.2 where the design comprises a novel high gain end-fire antenna, a quarter-wave stub, a Schottky diode ($SMS-7630-079LF$), and an SMD capacitor. The

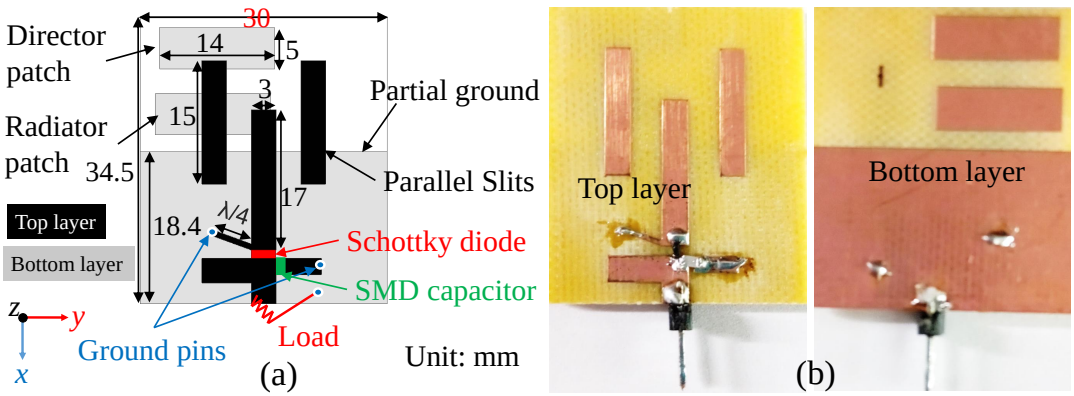

Figure 5.2: (a) Layout of presented H3C1 plug-in rectenna cell (b) Fabricated prototype.

conventional rectenna designs employ a matching network (MN) [34] and a DC low pass filter (LPF) to achieve maximum power transfer from a 50 Ω matched antenna to the rectifier. However, distributed MN and LPF circuits contribute more to insertion loss as well as unfavourable for rectenna miniaturization. Therefore, the integrated rectenna having direct conjugate matching with rectifying diode instead of matching using loops and stubs minimizes insertion loss and complements miniaturization. To design an integrated rectenna, first the impedance of the Schottky diode is evaluated at 5.8 GHz using LSSP technique for input power of -10 dBm and 850 Ω load and noted as $Z_d = 26.93 - j92.84$ Ω. Further, a novel high gain end-fire antenna is designed to achieve conjugate matching with Z_d. A quarter-wave shorted stub is imposed at antenna port and diode junction for transforming the ground conductor to one DC terminal besides rejecting higher order harmonics to improve the PCE. A 100 pF shunt SMD capacitor is placed at the output terminal for DC power storage and filtering. The presented design is inspired from [143, 144, 145, 146], which are end-fire microstrip antennas. However, their intricate feeding systems make these designs unsuitable for rectenna application. In contrast, the presented

end-fire antenna is designed with a proximity feed line enabling easy integration as a rectenna element, as illustrated in Fig. 5.2 (a). The antenna bottom layer has a radiator and a director patch elements with a partial ground to direct the beam in the end-fire direction. The upper layer has two parallel slits to achieve the desired directional radiation characteristics and matching. The presented H3C1 WPT rectenna cell is fabricated using MITS PCB prototyping machine and the prototype is shown in Fig. 5.2 (b). The antenna

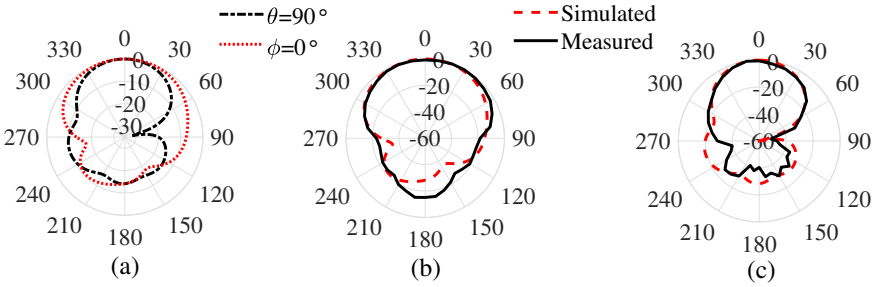

Figure 5.3: (a) xy ($\theta = 90°$) and xz ($\phi = 0°$) RF patterns of the presented antenna. Normalized harvested DC power pattern in (b) xy and (c) xz plane.

has a high gain (5.4 dBi), wide half-power beamwidth of 113° in xz-plane and a 66° beamwidth in xy-plane of RF patterns depicted in Fig. 5.3 (a). The rectenna cell is simulated (measured) for DC power patterns to show a wide DC half-power beamwidth 84° (86°) in the xz-plane and 42° (40°) in xy-plane are plotted in Fig. 5.3 (b)-(c), respectively. The simulated and measured patterns are in good agreement.

5.2.1 Scalable Assembly of the presented H3C1 WPT rectenna Cells

A number of rectenna cells can be plugged-in to form various geometrical arrangements for RF battery based on the requirements. Here, three different assemblies are presented in Fig. 5.4, which achieves 1) dynamic power harvesting using a linear-stacking battery, 2) orientation-insensitive dynamic power harvesting using a cuboid-stacking battery, and 3) two-way energy harvesting from horizontal as well as vertical waves along with orientation-insensitive operation using a combined-cuboid battery. A series DC combining technique is adopted to assemble the outputs of the cells. The performance is experimentally verified next.

5.2.2 Fabrication and Experiments

The presented H3C1 WPT rectenna cell and the composed sacalable assemblies are measured for WPT performance using the setup shown in Fig. 5.5, which includes an Agilent RF signal generator E8257D set to transmit 25 dBm signal at 5.8 GHz through a Tx horn antenna (linearly polarized) with 8.6 dBi gain imitating a wall mounted RF shower. Furthermore, the RF wave power density impinging on the presented H3C1 WPT rectenna aperture is 0.217 W/m^2. The WPT system is mounted 1 m away from the Tx on an automated turn table for DC pattern measurements using a Keysight U1232A multimeter. Firstly, the DC voltage across the varying load is measured as shown in

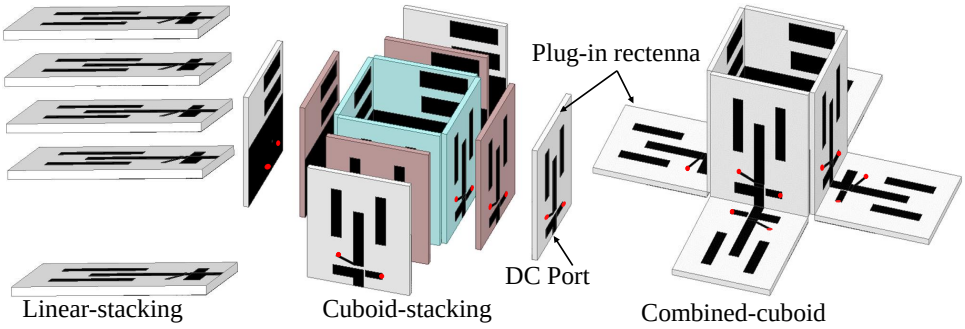

Figure 5.4: Assembly of the plug-in rectenna modules for scalable WPT system.

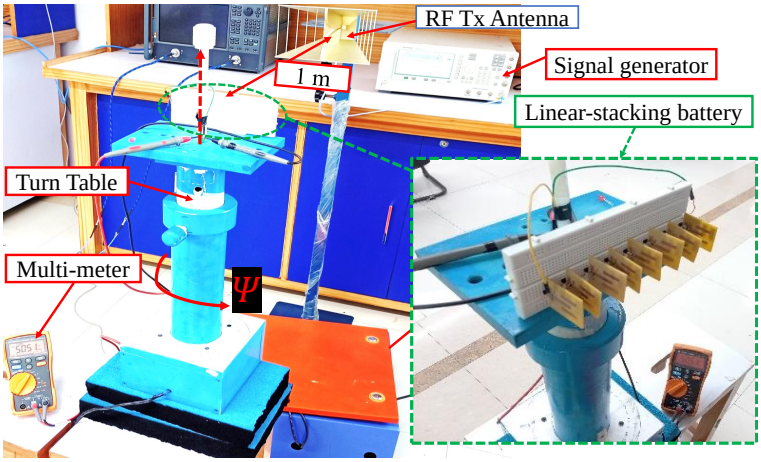

Figure 5.5: Setup for DC pattern measurements and linear-stacking under test.

Fig. 5.6 (a), showing rectenna efficiency of 71% at the optimal load of 700 Ω for a single rectenna cell. The corresponding measured DC power patterns of a single rectenna cell

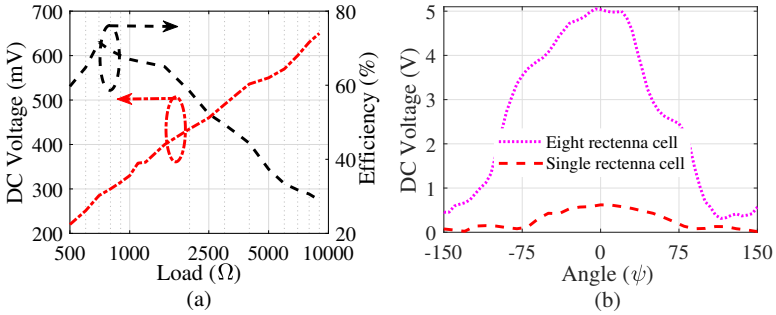

Figure 5.6: Measured (a) DC voltage and efficiency versus load for single rectenna (b) DC pattern of linear-stacking assembly.

are discussed earlier in Fig. 5.3 (b)-(c).

5.2.3 Linear-stacking Measurements

Multiple plug-in rectenna cells are assembled and connected through a breadboard for measuring the performance of the linear-stacking battery whose prototype is shown in the inset of Fig. 5.5. The stacked assembly of up to 8-cells is measured for the dc open-circuit voltage. The results are listed in Table 5.1 for increasing number of rectenna cells to demonstrate the dynamic harvesting capability. The results indicate that a single cell

Table 5.1: Linear-stacking for dynamic harvesting with increasing cells

Stacked rectennas	1	2	3	4	5	6	7	8
DC Voltage (mV)	660	1300	1826	2489	3240	3901	4489	5051

has 660 mV output which gradually increases to 5051 mV for 8-cells stacking. A little low additive scaling in harvested DC for increasing number of cells can be attributed to connection losses. The angular harvesting performance of the linear-stacking battery is measured by rotating the turn table in azimuth ψ with 5° steps and the measured DC patterns are plotted in Fig. 5.6 (b) for single cell and 8-cells assembly showing that the presented approach can meet the scaled power requirements of various nodes.

5.2.4 Cuboid-stacking and Combined-cuboid Measurements

Since the cuboid-stacking and combined-cuboid harvest from vertical waves, the measurement setup facilitating this is shown in Fig. 5.7 (a)-(b) which uses a planer array

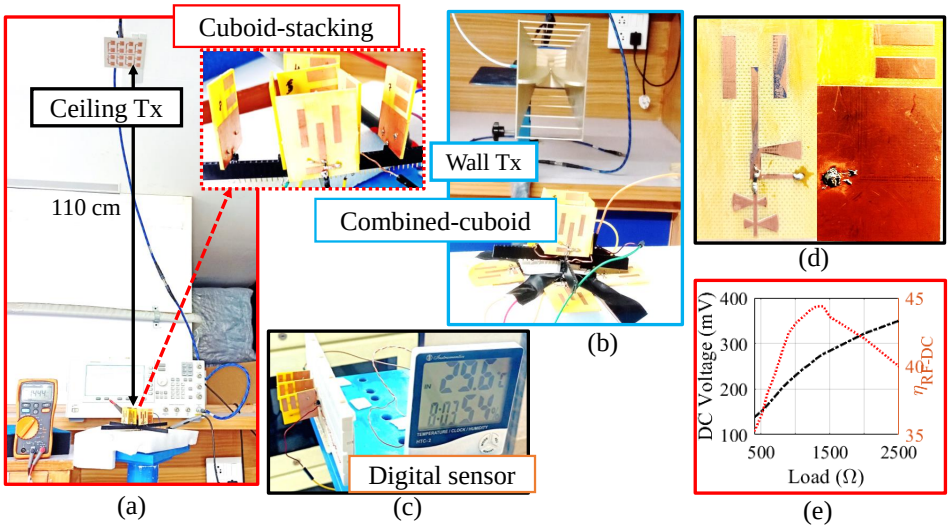

Figure 5.7: Measurement setup for (a) cuboid-stacking (b) combined-cuboid. (c) Real demonstration by powering a digital sensor (d) Fabricated prototype with matching network (e) RF-DC efficiency with matching network.

(linearly polarized) with 8.6 dBi gain as Tx imitating a ceiling mounted RF shower besides the original horn Tx on wall. The cuboid-stacking can harvest from only ceiling RF shower whereas combined-cuboid harvests from the both. The angular harvesting performance is measured and polarization mismatching due to orientation of the node is expected. However, the results depicted in Fig. 5.8 (a) displaying the measured DC patterns indicate that these assemblies have good tolerance for orientation misalignment and polarization mismatch. Moreover, the combined-cuboid is able to harvest energy from vertical as well as horizontal source with good angular coverage. A real application is also demonstrated in Fig. 5.7 (c) by powering a digital sensor with temperature and pressure monitoring in real scenario. The digital sensor is powered directly from the presented linear-stacking where 3-cells of the presented H3C1 WPT rectenna are sufficient for battery-less operation.

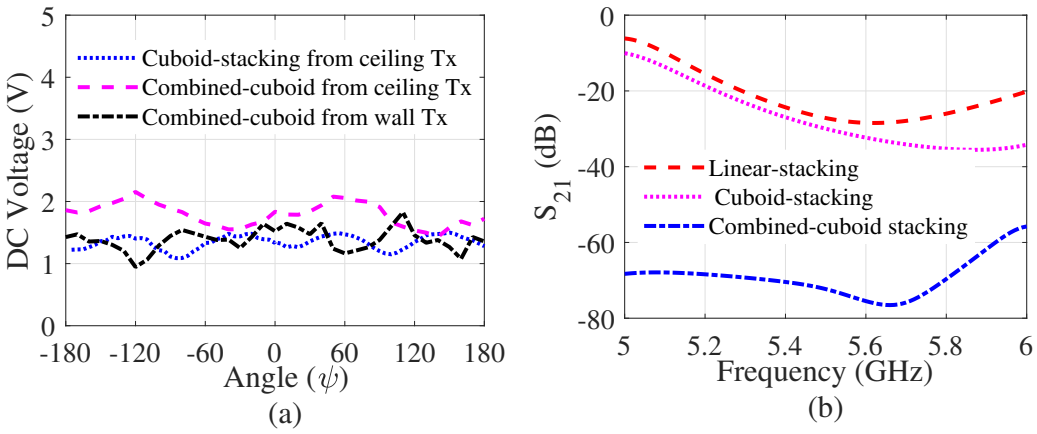

Figure 5.8: (a) Cuboid-stacking, and combined-cuboid batteries assembled from the presented H3C1 WPT rectenna cell (b) mutual coupling.

The mutual coupling effects are also under limits as presented in Fig. 5.8 (b) where the isolation between the adjacent antenna elements is 26 dB in the linear-stacking for a 10 mm inter-element distance, the same is 35 dB and 65 dB in the cuboid-stacking and the combined-cuboid, respectively. To showcase efficiency improvement by utilizing integrated rectenna design, the presented antenna with 50Ω input impedance is also designed. The 50Ω antenna has an RF gain of 5 dBi which is equivalent to the corresponding integrated design. Fig. 5.7(d) shows the fabricated prototype with the matching network and filter circuit [34] The rectenna with matching network harvests 267mV with an optimal load of 1300Ω and achieves RF-DC efficiency of 44.20%, as shown in Fig. 5.7 (e). This validates the benefit of utilizing the integrated topology of the rectenna design.

5.3 Summary

A novel integrated miniaturized H3C1 plug-in rectenna cell having end-fire pattern is presented for orientation-insensitive dynamic power harvesting capability at IoT sensor nodes. The presented H3C1 WPT rectenna cell has a high RF gain of 5.4 dBi with wide RF 3-dB beamwidth of 113° and 66° in two orthogonal planes, respectively. This results in corresponding DC beamwidth of 86° and 40°. The scalable linear-stacking battery formed by eight rectenna cells harvest 5051 mV against 660 mV harvested by a single cell which exhibits dynamic harvesting capability. Similarly, the cuboid and combined-cuboid stackings show good tolerance against orientation and polarization mismatching along with dynamic power harvesting. The low mutual coupling of ≤ -26 dB between adjacent rectennas allows for compact stacking structures suitable for size-constrained IoT sensor nodes. Hence, the presented plug-in strategy enhances harvested DC power and mitigates polarization and orientation mismatch problems in WPT systems. Furthermore, the WPT technology provides contactless power transfer to address power issues in sensor nodes, RFIDs, and medical devices. Therefore, to demonstrate an application scenario of true IoT, some WPT-enabled RFID tags are presented in Chapter 6.

Chapter 6

WPT-enabled IoT Application

6.1 Introduction

The previous chapter discussed spatial 3D-DC patterns to improve coverage and address power constraints in WPT applications. In this chapter, WPT-enabled designs for RFID applications are presented to address power issues with low reading range in WPT systems. Additionally, new techniques are introduced to design RFID tags for surface tolerance applications with a compact size and long reading range. The performance of RFID tags is intrinsically degraded when attached to different dielectric materials due to impedance mismatching with the tag chip [147]. Therefore, in applications such as liquid inventory, the tag design process must take into account the permittivity of water [148]. A compact, long-range, and flexible tag is preferred to easily attach to naturally curved bottles. This is achieved using an efficient conjugate impedance matching technique to match the tag antenna impedance with the RFID chip.

6.2 H4D1: A Surface-Tolerant, Robust, Miniaturized and Long-range WPT System

The schematic model of the presented H4D1 UHF RFID tag antenna for tracking water-filled bottles in commercial industry applications is shown in Fig. 6.1. Each carton

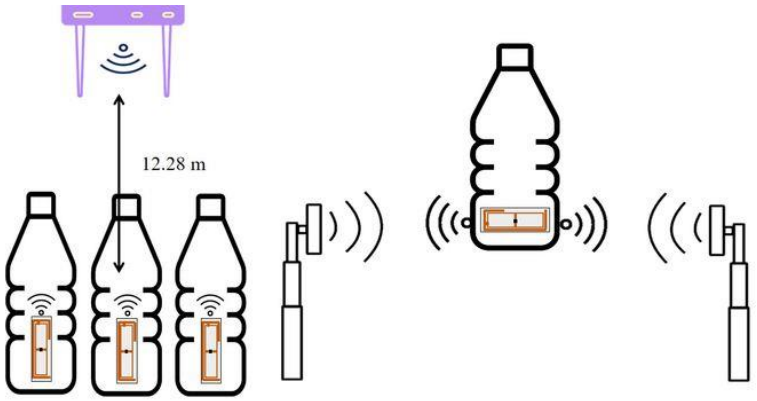

Figure 6.1: Schematic model of the presented H4D1 UHF RFID tag for water bottle applications in industry.

box in the warehouses is filled with M × N closely packed water bottles, and each bottle is labeled with an RFID tag. Therefore, a bore-sight radiation pattern is not desired for

this specific application as the bore-sight affects the tag performance negatively due to mutual coupling with unlikely read tags. Hence, a bi-directional antenna is required to overcome the mentioned issue.

6.2.1 Observation and problems in conventional designs

For the evolution of the presented H4D1 design, tags with conventional impedance matching techniques were investigated and printed on a single-sided polyester substrate (a label) having $\epsilon_r = 3.2$, $\tan\delta = 0.002$, and thickness 0.1 mm with copper ink deposition of 10 microns using commercial electromagnetic software Ansys HFSS. The conventional tags were simulated over High-Density Poly Ethylene (HDPE) bottle of 1mm thickness [147] filled with water, as illustrated in Fig. 6.2. This assumed a dielectric constant and electrical conductivity of water (H_2O) respectively as $\epsilon_r = 81$ and $\sigma = 0.01$ S/m. Their

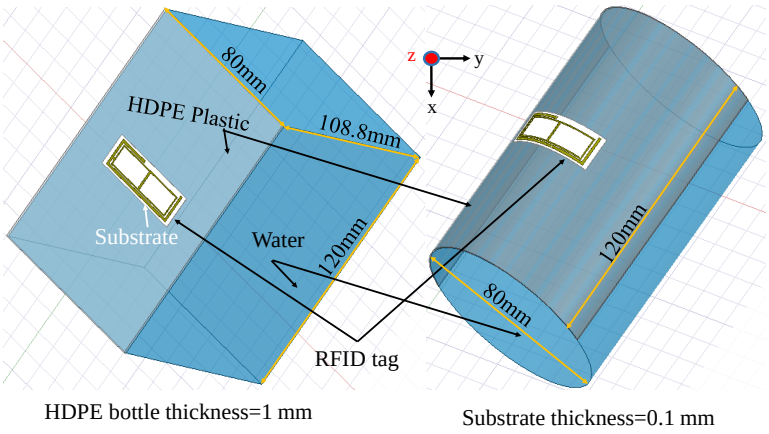

Figure 6.2: Simulation layout of the presented H4D1 tag antenna (left) on a container and (right) on a water bottle.

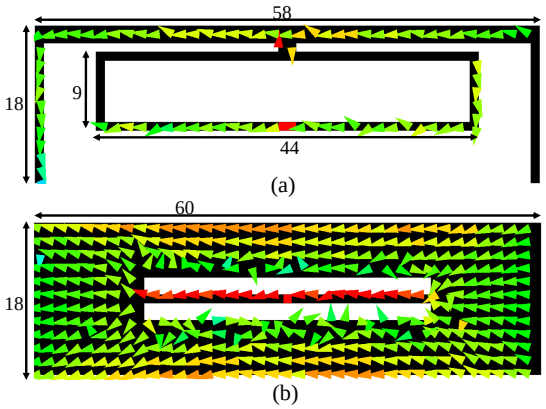

Figure 6.3: Current distributions for (a) T-matching, (b) Nested H-shaped slot with water bottle

.

corresponding current distributions with water are presented in Fig. 6.3. The results using T-matching techniques are illustrated in Fig. 6.3 (a), which show non-uniform currents in

the presence of water. On the other hand, the nested H-shaped slot technique of Fig. 6.3 (b) showed more balanced current distributions with relatively larger dimensions and low gain. To corroborate this in regard to their input reactance, the immediately outlined techniques were simulated at 866 MHz, and their corresponding impedances are presented in Table 6.1. It is noted that the reactance of the T-matching and nested H-shaped slot

Table 6.1: Impedance for the Different Techniques

Techniques	With water bottle (η_r)	Gain (dBi)
T-Matching	62.17 + j237.50 (12 %)	-5.5
Nested H-shaped slot	14 + j120.57 (19 %)	-2.1

vary significantly in the presence of water from the chip impedance ($Z_c = 38.83 + j153.30$). In addition, similar results are obtained from conventional reported T-matching [149, 150] and nested H-shaped slot designs [151, 152, 153, 148, 154] where the reading range of the tags was constrained in the presence of water. The T-matching technique reported a limited bandwidth, and the impedance of the tag antenna varied significantly in the presence of water. Similarly, the nested slot technique has large size radiators and the radiation efficiency (η_r) of both tags was constrained in the presence of water. The following problems are observed in the conventional UHF RFID tags:

- The impedance changes significantly in the presence of water, therefore, to design an efficient tag antenna, it must be impedance tolerant.
- The efficiency is reduced in the presence of water, therefore, an efficient tag antenna is desired.

Following the immediately mentioned observations, a novel UHF RFID tag antenna is presented, and its performance in the presence of water is discussed in the next subsection.

6.2.2 Design

The dimensions of the presented H4D1 tag antenna is shown in Fig. 6.4. The tag antenna

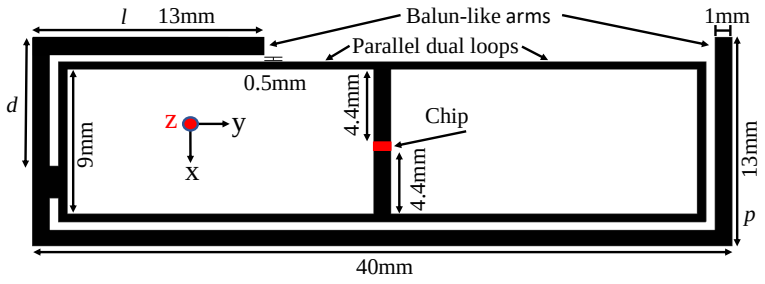

Figure 6.4: Dimensions of the presented H4D1 tag antenna.

comprises a radiating element using unbalanced strips made of balun-like arms, and these arms were wrapped around the tag's body (the parallel dual-loops) to minimize the overall size of the tag. The unbalanced strips led to an optimum design with reasonably good

impedance matching, current density, and long read range. The parallel dual-loops were used for their relatively good reactive impedance matching on high permittivity (water) compared to other conventional methods; this is achieved by a widespread magnetic field (H-field) distribution in the near-field which is less affected in the presence of water. The design evolution is presented next.

6.2.3 Design evolution

The initial antenna element was designed using the parallel dual-loops to obtain a wider bandwidth and relatively good impedance matching on high permittivity (water) in the desired UHF RFID band, as shown in Fig. 6.5. The dual loops were simulated following the

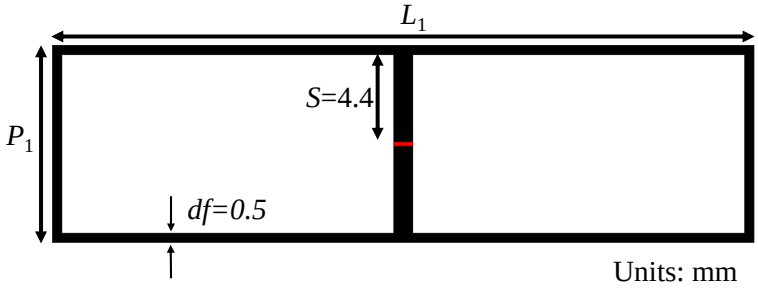

Figure 6.5: Dimensions of the loop antenna.

procedure of Fig. 6.2; an input impedance of (22.12 + j136.69) is obtained. The parametric analysis for this is reported later Section 6.2.6. To satisfy the second condition, in which η_r is to be improved, the radiating arms (unbalanced strips) of the presented H4D1 tag antenna were targeted for compactness and, thus, carefully wrapped around the dual-loops to minimize the adverse effects of the water. This is in contradiction with conventional approaches where large-size radiators are common.

It is noted that the reactance of the T-matching and nested H-shaped slot vary significantly in the presence of water, whereas the parallel dual-loops with reactance 136.69 Ω offered relatively good conjugate matching with the chip's reactance (−154.31 Ω) when attached to the water bottle. Furthermore, the η_r of the reported designs was ∼ 12 %, whereas the presented H4D1 tag antenna was 27 % in the presence of water. The folded, unbalanced strips of balun-like arms wrapped around the parallel dual-loops are presented next.

6.2.4 Effect of Unbalanced Strips

The effect of the unbalanced strips was observed by evaluating the current distributions shown in Fig. 6.6. The differential mode/common mode (DM/CM) was defined by means of the current distribution along the tag antenna. Whereas in the dual-loops a DM was present due to the opposite currents flowing at every point in the loops, in the unbalanced strips a CM was triggered from currents flowing in an even direction. The effect with the water bottle, depicted in Fig. 6.6 (a), demonstrated that the currents in the unbalanced

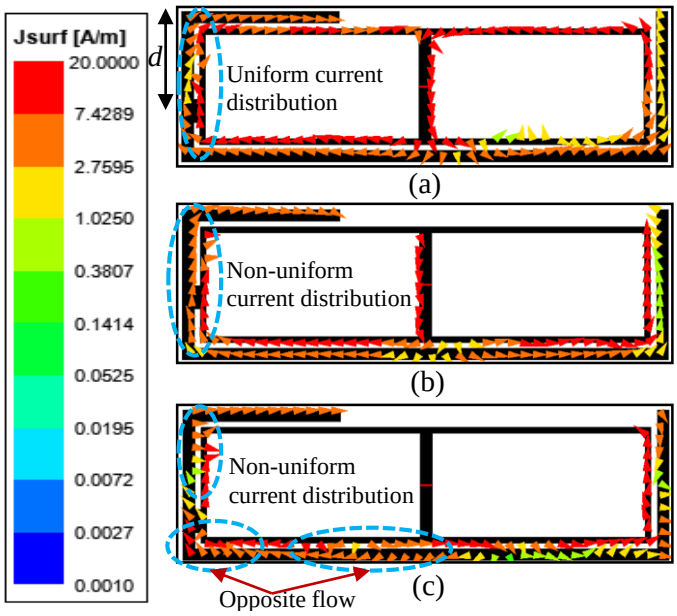

Figure 6.6: Current distributions (a) with water bottle for $d = 7.6$ mm (b) $d = 6.6$ mm and (c) $d = 8.6$ mm.

strips flowed constructively with the dual-loops. This is because the presented H4D1 tag antenna (unbalanced strips connected to parallel dual-loops) serves as an impedance transforming balun, enabling a DM current in the dual-loops and a CM in the unbalanced strips depending on design parameters. To corroborate this, the current distribution of the tag for various lengths of d (defined in Fig. 6.4) are shown in Fig. 6.6 (a-c), where d defines the location of the joint between the unbalanced strips and the dual-loops. For $d = 6.6$ mm, the current magnitude distribution in the dual-loops was non-uniform (Fig. 6.6 (b)), similarly, for $d = 8.6$ mm Fig. 6.6 (c), the DM current distribution existed in the dual loops. However, when $d = 7.6$ mm (Fig 6.6 (a)), desired current distributions in the dual-loops and the unbalanced strips were found, corroborating the impedance transformer balun-like behavior. The following input impedances, $38.83 + j153.30$, $36.44 + j154.80$, and $29.62 + j159.76$, were observed for $d = 6.6$ mm, 7.6 mm, and 8.6 mm, respectively, proving that out-of-phase currents in the unbalanced strips (balun-like arms) affected the impedance matching of the tag positively.

6.2.5 Simulated Results

The presented H4D1 tag antenna was simulated to evaluate its input impedance $Z_a = R_a + jX_a$, gain $G_r(\phi, \theta)$, and read range performance by following the procedure of Fig. 6.2. The read range, d, was calculated theoretically using Friss equation as

$$d = \frac{\lambda}{4\pi}\sqrt{\frac{P_t G_t(\phi,\theta) G_r(\phi,\theta)\tau P_m}{P_{th}}} \tag{6.1}$$

where P_t is the transmitter power, G_t is the gain of the transmitter antenna, P_{th} is the chip sensitivity (-22.5 dBm), and P_m is the polarization mismatch efficiency ($P_m = 0.5$ for

the circularly polarized transmitter antenna). Here, τ is the power transmission coefficient and can be calculated as

$$\tau = \frac{4R_c R_a}{|Z_c + Z_a|^2}, 0 \leq \tau \leq 1 \tag{6.2}$$

where $Z_c = R_c - jX_c$ is the chip impedance. For the conjugate matching, a 1.13 pF capacitance with a parallel resistance of 0.7 kΩ was assumed for the chip. The impedance matching between the tag antenna and chip was estimated using (2), and the simulated input impedance of the presented H4D1 tag antenna with and without a water bottle is illustrated in Fig. 6.7. Since the antenna was tailored for water applications, it is observed

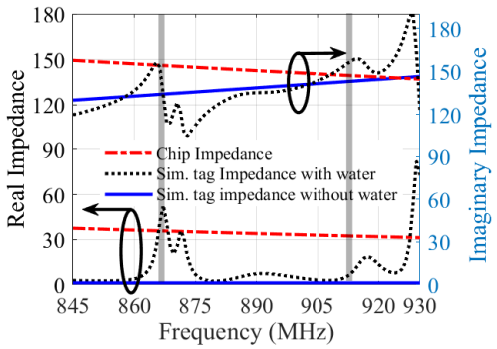

Figure 6.7: Impedance of the presented H4D1 tag antenna with and without water bottle.

that the impedance of the presented H4D1 tag antenna (with water) is well matched to the chip impedance in ETSI and FCC bands. However, this is not the case when the water is not present. That is a compromised 25 % efficiency.

6.2.6 Parametric analysis

A parametric study of the unbalanced strips was carried out by varying l and p at 866 MHz to maximize the reading range. The thickness of the water bottle was 1 mm, and the length of l and p were varied in $1 - 20$ mm and $1 - 15$ mm range, respectively. The maximum reading range of $\sim$ 13.33 m is shown in Fig. 6.8 when $l = p = 13$ mm, which corresponds to a simulated gain of 0.2 dBi. Furthermore, the parametric study of the dual loops (P_1 and L_1 in Fig. 5) was conducted to analyze the effects of its dimension on the impedance matching, results are shown in Table 6.2. The P_1 and L_1 were chosen 10 and 37, respectively, based on the impedance matching, since other dimensions exhibit significant reactance, which fluctuates more during the integration of unbalanced strips.

6.2.7 Effect of bottle thickness

The presented H4D1 tag antenna was attached to HDPE plastic bottles of different thicknesses ($0.3 - 1.5$mm) to investigate the impact of bottle thickness on the reading range. The result indicates a maximum reading range of 14.30 m achieved for 1.5 mm bottle thickness and a minimum reading range of 10.19 m for 0.3 mm. This is shown in Table 6.3.

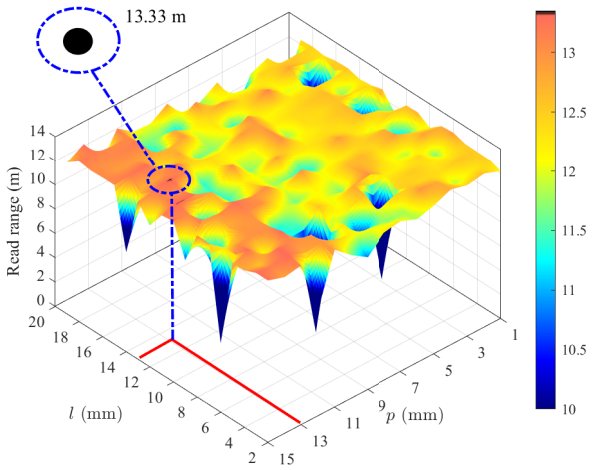

Figure 6.8: Parametric study of the unbalanced strips at 866MHz for tag on water-filled HDPE bottle.

Table 6.2: Parametric study of dual loop impedance at 866MHz for tag on water-filled bottle.

S.N.	P_1 (mm)	L_1 (mm)	Impedance (Ω)
1.	9	36	$15.24 + j160.12$
2.	9	37	$3.34 + j123.01$
3.	9	38	$31.39 + j150.09$
4.	10	36	$24.87 + j153.26$
5.	10	37	$22.12 + j136.69$
6.	10	38	$29.31 + j160.26$
7.	11	36	$24.62 + j184.98$
8.	12	37	$43.87 + j169.47$
9.	13	38	$49.65 + j185.12$

6.2.8 Effect of bottle volume

The presented H4D1 tag antenna was also investigated for bottles of different volumes filled with water. Table 6.4 shows the effect for the different cases. Although a compromise performance can be observed for unrealistically small bottle volumes (3. and 4.), more prominent results are observed for realistic cases (1. and 2.).

6.2.9 Effect of different graded bottle

The presented H4D1 tag antenna performance was also evaluated for bottles made from various plastic materials HDPE, PET, PVC, Polypropylene (PP), and LDPE. Bottle thicknesses of 1mm were considered for this analysis. Table 6.5 shows reasonable impedance matching results on various plastic materials with only a slight variation in the reading range.

6.2.10 Performance of the presented H4D1 tag antenna with frequency

Although the presented H4D1 tag antenna was tailored for the 866MHz and 915MHz frequency bands, Table 6.6 shows its behavior for several frequency bands. A maximum

Table 6.3: Performance of the presented H4D1 tag on different thicknesses of the water bottle.

S.N.	Bottle-thickness (mm)	Impedance (Ω)	Gain (dBi)	Reading Range (m)
1.	0.3	82.88 + j233.34	0.2	10.19
2.	0.4	54.80 + j183.40	0.5	12.84
3.	0.5	48.56 + j181.66	0.1	12.39
4.	0.7	45.92 + j162.7	0.3	13.31
5.	1	36.44 + j154.8	0.2	13.33
6.	1.2	46.56 + j155.52	0.1	13.06
7.	1.5	39.93 + j144.13	0.9	14.30

Table 6.4: Performance of the presented H4D1 tag antenna for various water bottle volumes.

S.N.	Volume-water-filled bottle (mm^3)	Impedance (Ω)	Gain (dBi)	Reading Range (m)
1.	120 × 80 × 108.8	36.44 + j154.8	0.2	13.33
2.	200 × 100 × 120	5.71 + j145.88	0	8.79
3.	80 × 50 × 100	1.92 + j125.60	−5.7	2.36
4.	75 × 50 × 50	2.58 + j136.69	−5.3	3.22

reading range of 13.33 m is achieved in the ETSI band (866MHz) and a read range of 4.22 m in the lower FCC band (902MHz).

6.2.11 Magnetic field distribution and bending tolerance

The magnetic field (H-field) distribution of the presented H4D1 tag antenna was also simulated and is illustrated in Fig. 6.9. The H-field was observed in a plane 1 mm away

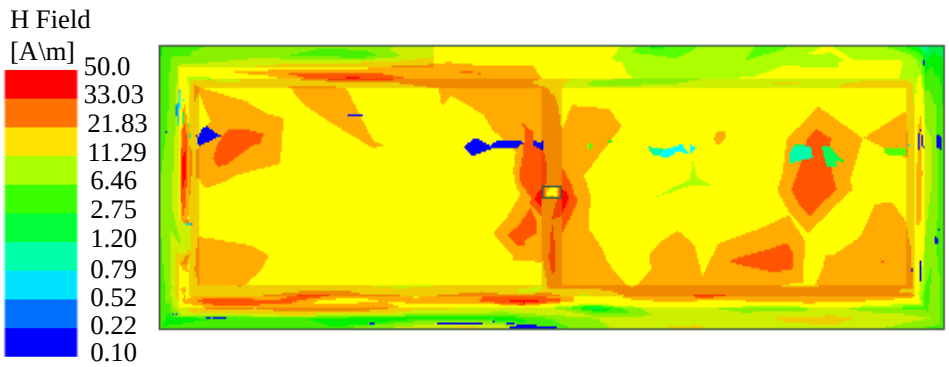

Figure 6.9: H-field distribution of the presented H4D1 tag antenna.

from the tag. It is apparent from Fig. 6.9 that the H-field intensity is higher within the dual-loop area. It was witnessed that a large dual-loop led to wide H-field distribution and that, compared to other conventional methods, significantly improved the read range. The bending tolerance of the presented H4D1 tag antenna used as a label was evaluated when affixed on bottles of various shapes.

This tag antenna was placed longitudinal or across the length of the water bottle, as shown in Fig. 6.10 (a). Naturally, the bending was prominent for the latter. Therefore, the read

Table 6.5: Performance of the presented H4D1 tag antenna on the different grades of the water bottle.

S.N.	Material	Impedance (Ω)	Gain (dBi)	Reading Range (m)
1.	HDPE	$36.44 + j154.8$	0.2	13.33
2.	PET	$46.52 + j165.26$	0.6	13.72
3.	PVC	$38.6 + j159$	0.59	13.90
4.	Polypropylene (PP)	$33.72 + j138.91$	0.5	13.46
5.	LDPE	$36.81 + j156$	0.2	13.32

Table 6.6: Performance of the presented H4D1 tag antenna for in various frequency standards.

S.N.	Frequency MHz	Frequency allocated	Impedance (Ω)	Gain (dBi)	Reading Range (m)
1.	866	Europe/ India	$36.44 + j154.8$	0.2	13.33
2.	902	American	$1.93 + j137.86$	-1.9	4.22
3.	908.5	Korea	$2.79 + j145.30$	-1.4	5.59
4.	915	FCC/ American	$13.26 + j158.79$	0.3	11.92
5.	928	American	$41.15 + j186.06$	-2.4	9.11

range for different bendings was simulated using the model depicted in Fig. 6.10 (b), where the bending radius is denoted as r. Note that $r = \infty$ represents a flat surface, whereas lower values of r represent a higher bending corresponding to water bottles of smaller size. The simulated read range of the presented H4D1 tag antenna on water bottles of different r is shown in Table 6.7. A maximum read range of 13.33 m and 5.8 m was found for

Table 6.7: Bending tolerance of the presented H4D1 tag on the water bottle

Radius r of bottle (mm)	∞	35	30	25	20	15
Read Range (m)	13.33	12.43	10.3	10.1	6.8	5.8

$r = \infty$ and $r = 15$ mm, respectively. Additionally, results revealed that for a typical water bottle of 50 cl having $r = 35$ mm, the presented H4D1 tag antenna attained a read range of 12.43 m, which is an acceptable bending tolerance.

6.2.12 Mutual coupling

Mutual coupling can cause a change in the input impedance of tag antennas, resulting in significantly reduced power transfer to the chip. Therefore, especially in systems where several RFID tag antennas must coexist, the mutual coupling should be assessed in order to validate the design. Fig. 6.11 shows the simulation setup, considers two neighbor models and evaluates the mutual coupling effect by stimulating both tags simultaneously. The response is given in Fig. 6.12 and shows a -30dB coupling effect between tags which is reasonable for stockpiling applications.

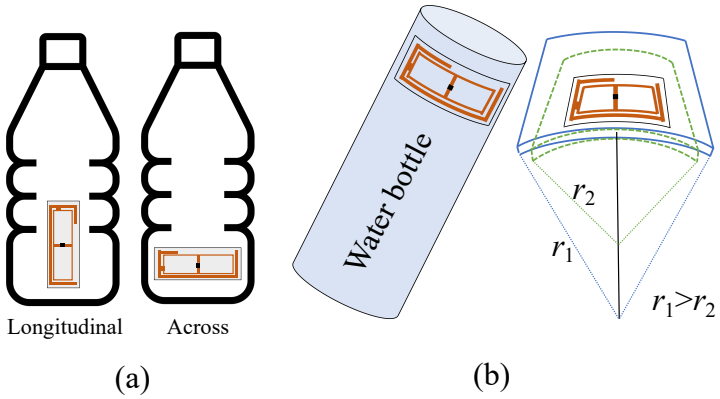

Figure 6.10: The presented H4D1 tag (a) affixed on water bottle (b) bending tolerance simulation model for different bottle sizes.

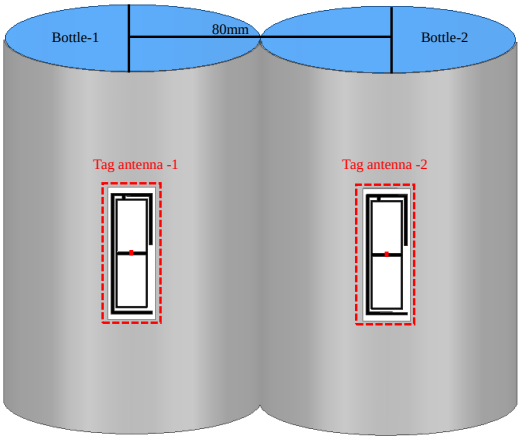

Figure 6.11: Simulation of two neighboring presented H4D1 tag antennas.

6.2.13 Fabrication and Measurement

The presented H4D1 tag antenna was fabricated, as shown in Fig. 6.13 (a), by a screen printing process, which involved a transfer of copper ink onto a single-sided polyester (typical label of a bottle of water) whose material properties were earlier detailed in Section 2.1. The tag antenna (used as a label) was then affixed on a water bottle. The measurement setup is shown in Fig. 6.13 (b), which includes a 9 dBi transmitter horn antenna fed with an RF signal generator (Agilent Technologies) and a Keysight N9915A handheld spectrum analyzer (SA) connected to the presented H4D1 tag antenna for measuring received power. A matching circuit was employed for the experiments when connected to the Spectrum Analyzer (SA); the associated insertion loss (IL) was accounted for. The measurement is accurate enough since the SA is a narrow band with a lower noise floor and better dynamic range, so its sensitivity is better than traditional power meters. The signal generator was set at 27 dBm, and the received signal strength was measured using the SA. The measurements were performed for the ETSI (866 MHz) and the FCC (915 MHz) bands. It was witnessed that the presented H4D1 tag antenna had better signal strength compared to the literature. The maximum received signal strength reported in the

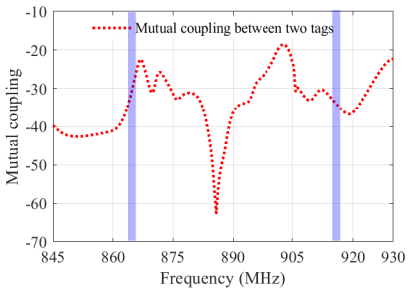

Figure 6.12: Mutual coupling between two neighboring presented H4D1 tag antennas.

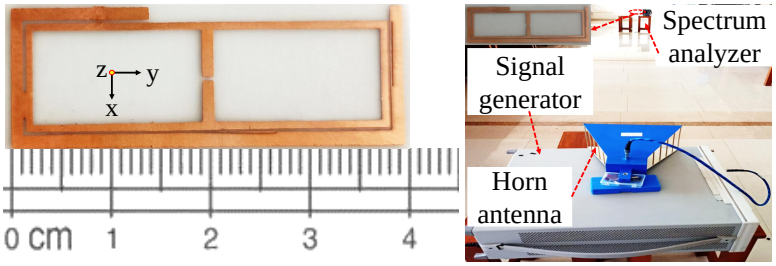

Figure 6.13: (a) Fabricated and (b) measurement setup of the presented H4D1 tag antenna.

literature is −50 dBm, compared to the presented H4D1 tag of −19 dBm; both measured 12 m away from the transmitter using the ETSI band. The presented H4D1 tag antenna was affixed to the water bottle for realistic measurements and moved carefully closer to the transmitter until a minimum of −19 dBm at 866 MHz and −20 dBm at 915 MHz was attained, which led to a read range of 12.28 m and 11.13 m for the ETSI and FCC bands respectively.

6.2.14 Impedance Measurement

A two-port S-parameter approach [155] is used to calculate the input impedance of the tag antenna, which transforms the S-parameter into Z-parameters. The tag antenna is regarded as a two-port network in this approach, and the differential impedance is calculated using (3). Two semi-rigid coaxial cables and a Keysight PNA-L were required to perform the S-parameter measurements.

$$Z_t = \frac{2\ Z_0(1 - S_{11}S_{22}) + (S_{12}S_{21}) - S_{12} - S_{21}}{(1 - S_{11})(1 - S_{22}) - S_{12}S_{21}} \tag{6.3}$$

The Vector Network Analyser (VNA) was carefully calibrated to obtain accurate S-parameters, and the effects of the semi-rigid coaxial cables were compensated using the port extension technique. The measured and simulated impedance of the presented H4D1 tag antenna with a water bottle at 866 MHz and 915 MHz are listed in Table 6.8. The theoretical chip impedance 35.58 − j154.31 Ω at 866 MHz and 32.28 − j146.83 Ω at 915MHz, is also provided for reference. The simulated and measured findings indicate similar trends, however, certain inconsistencies between the simulated and measured results were due to the manufacturing tolerances and some variation in water and HDPE

Table 6.8: Measured and Simulated impedance of the presented H4D1 tag antenna.

Frequency (MHz)	Measured	Simulated
866	23.17 + j137.03 Ω	36.44 + j154.8 Ω
915	20.5 + j136.07 Ω	13.26 + j158.79 Ω

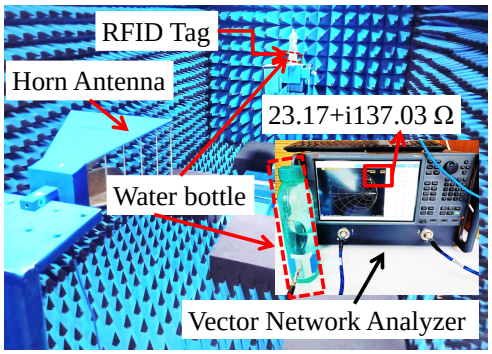

Figure 6.14: Measurement setup of the presented H4D1 tag antenna with water bottle.

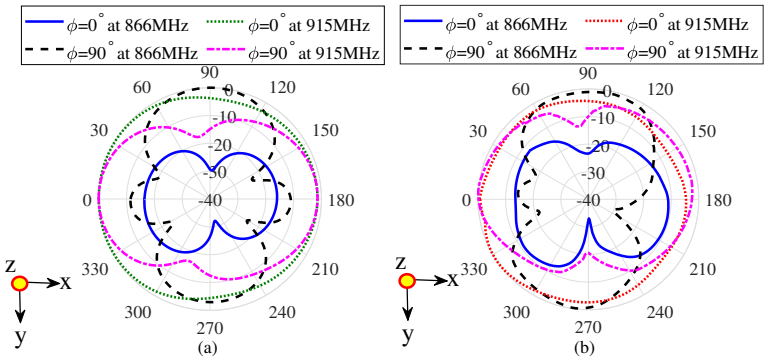

Figure 6.15: (a) Simulated and (b) measured radiation patterns of the presented H4D1 tag on water-filled HDPE bottle.

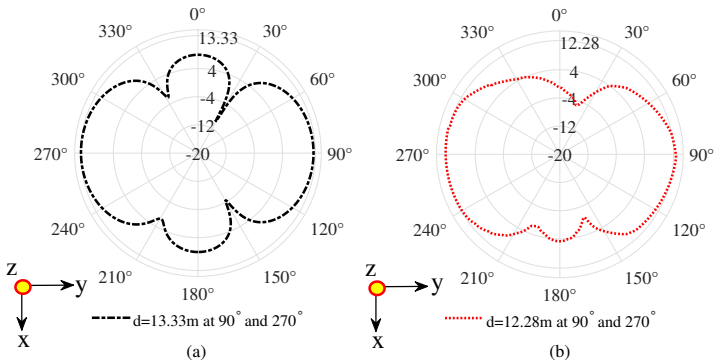

Figure 6.16: (a) Simulated and (b) measured read range patterns of the presented H4D1 tag on water-filled HDPE bottle.

bottle properties, which led to a slight deviation of the measured input impedance of the fabricated tag antenna from simulations.

6.2.15 Radiation Pattern Measurement

The radiation patterns of the presented H4D1 tag antenna (with water bottle) were measured in an anechoic chamber, Fig. 6.14, and the results shown in Fig. 6.15. The bidirectional patterns, more apparent at 866 MHz, are perceived as positive for bottling lines applications where a reduction of the mutual coupling [156] among tagged water bottles in closely stacked or piled packing is expected in the bottled water industry. The maximum measured gain of the presented H4D1 tag antenna (with water bottle) was 0.05 dBi and −0.6 dBi at 866 MHz and 915 MHz, respectively. Although the presented H4D1 tag antenna was specifically designed for the 866 MHz band, results are shown additionally at 915 MHz to demonstrate its performance in the FCC band. Further, the reading range of the presented H4D1 tag antenna measured at various angles (0° to 360°) was evaluated and is presented in Fig. 6.16. The simulated result is also included in the figure and show reasonable agreement between both, Fig. 6.16 (a) and (b). Because the read range patterns are more bidirectional like, this is attractive for water inventory in industrial applications such as a conveyor belt and stockpiling where mutual coupling minimal effect (0° and 180°) is preferred.

6.3 Various other robust, flexible, biodegradable WPT-enabled IoT tags

A WPT-enabled ultra-high frequency (UHF) RFID tag antenna using nonuniform meandered lines for the textile industry is presented in Fig. 6.16 (a). The presented WPT-enabled UHF RFID tag antenna offers relatively low cost, wideband, compactness, and good conjugate matching in the presence of its robust housing with a good dipole-like read range. Results show an antenna with a wide bandwidth of 900 MHz and a long read range of 10.2 m, making it a potential candidate for retail garments in the textile industry. However, the presented tag antenna is designed on FR4 substrate, which is not easily attached to textiles. Therefore, a fully bendable UHF RFID tag antenna is presented in Fig. 6.16(b), which can be easily attached to clothing using adhesive. This is aimed at being embedded in retail garments for long-life cycles. Moreover, the presented bendable UHF RFID tag antenna results show a wide bandwidth of 900 MHz and a long read range of 10.1 m, making it a potential candidate for retail garments in bendable applications of the textile industry. Moreover, the presented bendable cloth tag antenna is designed on polyamide material, which is not biodegradable. Therefore, a biodegradable and cost-effective passive UHF RFID tag antenna for short-life cycle IoT applications is presented in Fig. 6.16 (c). The biodegradability and cost-effectivity are given by inking bioresorbable copper-based paint on a bioresorbable cellulose-based substrate. Results showed 130MHz bandwidth and a long read range of 10.2m-12.7m when attached to several host objects of materials typically encountered in IoT applications. Hence, reasonably to be regarded as multi-platform tolerant. Further, to enhance the reading range, WPT-enabled RFID tags are designed at 5.8 GHz, shown in Fig. 6.16 (d).

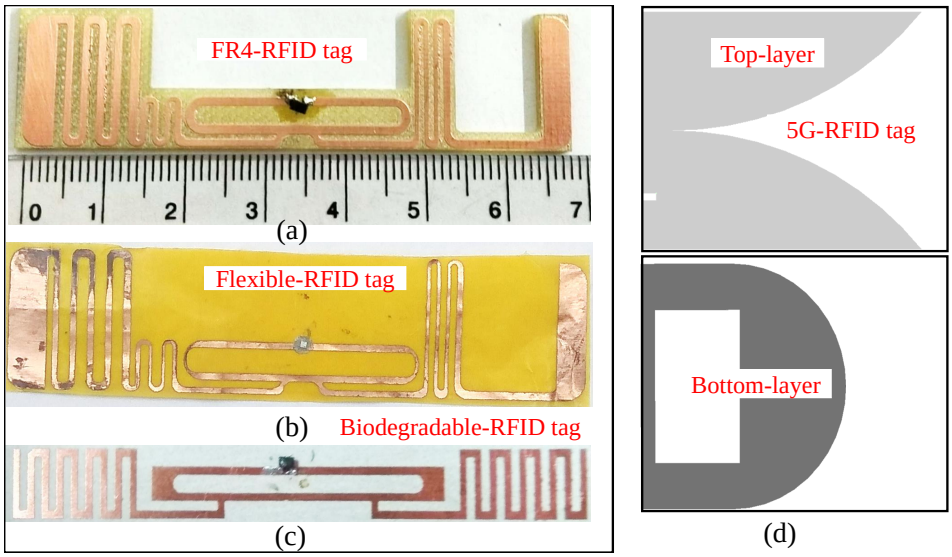

Figure 6.17: Various WPT-enabled IoT tags.

This RFID tag antenna is designed with multi-band features, making them suitable for various upper and lower wifi band applications. This RFID tag is designed with a compact Vivaldi-like antenna with a completely modified ground plane. These WPT-enabled RFID tags harvest more RF waves and provides to chip for one bit data transmission with long reading range.

6.4 Summary

In this chapter, WPT-enabled RFID tag antennas are evaluated for multi-platform applications. The reported tag antenna performance is degraded when attached to different dielectric materials. To address this issue, two techniques are followed in this chapter. Dual loops with folded lines and non-uniform meander line techniques. The non-uniform meander line technique is designed for low-dielectric materials, whereas the folded loop technique is designed explicitly for high-dielectric materials. The measured results showed that, presented RFID tag antenna harvest more RF power and re-transmitted to long distance.

Chapter 7

Conclusion and Future Works

7.1 Conclusion

In conclusion, this thesis aimed to design efficient wireless power transfer (WPT) rectennas to harvest maximum DC power and improve power conversion efficiency (PCE). The literature survey of the state-of-the-art rectennas is discussed in Chapter 1. The background design theory and basic fundamentals of the WPT rectenna are discussed in Chapter 2. The literature designs are found to suffer from low PCE in the WPT systems due to various design problems. Therefore, the authors made four significant contributions to wireless power transfer in this thesis, which are outlined in the following sub-sections:

7.1.1 Chapter 2

Chapter 2 presented a rectenna system utilizing a conventional patch antenna. The chapter also introduced a radial stub-enabled matching network and a higher-order low-pass filter. In addition, combining techniques for rectenna arrays are introduced to mitigate angular misalignment, providing an optimal method for mitigating this issue.

7.1.2 Chapter 3

Chapter 3 presented an analytical framework to mitigate angular misalignment by imposing specific conditions on the DC power pattern. Based on this framework, three antennas with omnidirectional capabilities in the azimuth plane are developed to improve PCE. The first two designs offer 3D geometries, which have limited applications. A dual-purpose WPT system with orientation estimation capabilities is designed to address this issue. The simulation and measurement results corroborate with each other at 5.8 GHz.

7.1.3 Chapter 4

Chapter 4 presented two novel fully integrated planar multi-sector rectenna arrays designed to achieve nearly uniform 3D spherical DC coverage. To achieve orientation-insensitive azimuth and elevation plane coverage, the first antenna utilizes six boresight and endfire antennas with inherent DC combining. Additionally, direct conjugate matching of the antenna and rectifier circuit with integrated operation is applied to realize a fully integrated design. This reduces insertion losses and achieves the desired 3D coverage and miniaturization, making it suitable for deployment at space-constrained IoT sensor

nodes for orientation-oblivious wireless powering. The second antenna design also achieves orientation-insensitive azimuth and elevation plane coverage. This presented rectenna features eight radially arranged end-fire (EFR) elements and a bore-sight (BSR) element with multi-arms for inherent DC combining, utilized at the center with orthogonally polarized ports. Further, direct conjugate matching of the antenna and rectifier circuit with integrated operation is applied to realize a fully integrated design.

7.1.4 Chapter 5

Chapter 5 presented a multi-cell linear, boxed, and combined stacking for a scalable plug-in-type WPT system at 5.8 GHz. The presented design scheme enables dynamic power harvesting and polarization-insensitive operation. A novel end-fire integrated miniaturized plug-in-type rectenna element is presented to achieve scalable design features in WPT systems. The scalable approach mitigates the need to design different rectenna modules as the energy requirement or orientation of the sensor nodes changes in an IoT application, resulting in a low-cost system. The experimental results validate the claims regarding the advantages of the presented scalable design feature with the presented plug-and-play rectenna element.

7.1.5 Chapter 6

Chapter 6 presented the WPT-enabled RFID tag antennas to achieve wireless operations, which include cloth inventory, biodegradability, and water inventory applications. Moreover, the presented IoT antennas offer long-distance wireless operation, which makes them suitable for IoT applications. The long reading range is achieved by developing two new techniques, non-uniform meander lines for low dielectric materials, i.e., wood, glass, plastic, and rubber, and the dual loops technique is investigated for high-dielectric materials, which include water, alcohol, and fruit juices. The results show that the presented WPT-enabled RFID antennas harvest more power efficiently, and the DC chip retransmits one-bit data to the user at a longer distance.

7.2 Future work

The generalized rectenna systems have a large footprint, which makes them unsuitable for IoT applications. Future work can be carried out in the following areas:

- The WPT system should be compact, with high power harvesting capabilities. This can be achieved by employing new schemes in designing compact high-gain, wideband and multi-polarized antennas. Furthermore, the performance of the WPT system can be improved by introducing advanced Schottky diodes, which have low circuit losses and efficiently rectify RF power.
- The performance of the WPT system can be improved by increasing the surface area of the rectennas. This can be achieved by utilizing reversible rectennas.

- The literature work and presented WPT system lack a complete integrated system, which includes power management circuits and DC-DC converters. The harvested power must be stored in an integrated supercapacitor or battery for later use. Moreover, fully integrated sensor nodes are desirable which can harvest RF power as per their requirement and retransmit undesired RF power to increase reflections at the adjacent or power-hungry nodes to fulfill their needs.

References

[1] A. Zielonka, A. Sikora, M. Woźniak, W. Wei, Q. Ke, and Z. Bai, "Intelligent internet of things system for smart home optimal convection," *IEEE Trans. Ind. Informat.*, vol. 17, no. 6, pp. 4308–4317, 2021.

[2] Y. Mehmood, F. Ahmad, I. Yaqoob, A. Adnane, M. Imran, and S. Guizani, "Internet-of-things-based smart cities: Recent advances and challenges," *IEEE Commun. Mag.*, vol. 55, no. 9, pp. 16–24, 2017.

[3] L. Guntupalli, M. Gidlund, and F. Y. Li, "An on-demand energy requesting scheme for wireless energy harvesting powered IoT networks," *IEEE Internet Things J.*, vol. 5, no. 4, pp. 2868–2879, 2018.

[4] S. Sudevalayam and P. Kulkarni, "Energy harvesting sensor nodes: Survey and implications," *IEEE Commun. Surveys Tuts.*, vol. 13, no. 3, pp. 443–461, 2011.

[5] W. Lin and R. W. Ziolkowski, "Electrically small, single-substrate huygens dipole rectenna for ultracompact wireless power transfer applications," *IEEE Trans. Antennas Propag.*, vol. 69, no. 2, pp. 1130–1134, 2021.

[6] N. Shinohara, "History and innovation of wireless power transfer via microwaves," *IEEE J. Microwaves*, vol. 1, no. 1, pp. 218–228, 2021.

[7] M. Wagih, A. S. Weddell, and S. Beeby, "Rectennas for radio-frequency energy harvesting and wireless power transfer: A review of antenna design [antenna applications corner]," *IEEE Antennas Propag. Mag.*, vol. 62, no. 5, pp. 95–107, 2020.

[8] J. Akkermans, M. van Beurden, G. Doodeman, and H. Visser, "Analytical models for low-power rectenna design," *IEEE Antennas Wireless Propag. Lett.*, vol. 4, pp. 187–190, 2005.

[9] C. T. Rodenbeck, P. I. Jaffe, B. H. Strassner II, P. E. Hausgen, J. O. McSpadden, H. Kazemi, N. Shinohara, B. B. Tierney, C. B. DePuma, and A. P. Self, "Microwave and millimeter wave power beaming," *IEEE Journal of Microwaves*, vol. 1, no. 1, pp. 229–259, 2021.

[10] M. A. Ullah, R. Keshavarz, M. Abolhasan, J. Lipman, K. P. Esselle, and N. Shariati, "A review on antenna technologies for ambient rf energy harvesting and wireless power transfer: Designs, challenges and applications," *IEEE Access*, vol. 10, pp. 17231–17267, 2022.

[11] M. Arrawatia, M. S. Baghini, and G. Kumar, "Broadband bent triangular omnidirectional antenna for RF energy harvesting," *IEEE Antennas Wireless Propag. Lett.*, vol. 15, pp. 36–39, 2016.

[12] H. Zhang, S.-P. Gao, W. Wu, and Y.-X. Guo, "Uneven-to-even power distribution for maintaining high efficiency of dual-linearly polarized rectenna," *IEEE Microw. Wireless Compon. Lett.*, vol. 28, no. 12, pp. 1119–1121, 2018.

[13] J. McSpadden, L. Fan, and K. Chang, "Design and experiments of a high-conversion-efficiency 5.8-ghz rectenna," *IEEE Trans. Microw. Theory Techn.*, vol. 46, no. 12, pp. 2053–2060, 1998.

[14] S. D. Joseph, Y. Huang, S. S. H. Hsu, A. Alieldin, and C. Song, "Second harmonic exploitation for high-efficiency wireless power transfer using duplexing rectenna," *IEEE Trans. Microw. Theory Techn.*, vol. 69, no. 1, pp. 482–494, 2021.

[15] H. Sun, Y.-x. Guo, M. He, and Z. Zhong, "Design of a high-efficiency 2.45-ghz rectenna for low-input-power energy harvesting," *IEEE Antennas Wireless Propag. Lett.*, vol. 11, pp. 929–932, 2012.

[16] P. Lu, C. Song, and K. M. Huang, "A two-port multipolarization rectenna with orthogonal hybrid coupler for simultaneous wireless information and power transfer (swipt)," *IEEE Trans. Antennas Propag.*, vol. 68, no. 10, pp. 6893–6905, 2020.

[17] Z.-X. Du, S. F. Bo, Y. F. Cao, J.-H. Ou, and X. Y. Zhang, "Broadband circularly polarized rectenna with wide dynamic-power-range for efficient wireless power transfer," *IEEE Access*, vol. 8, pp. 80561–80571, 2020.

[18] P. He, D. Zhao, L. Liu, J. Xu, Q. Zheng, C. Yu, and X. You, "A w-band 2×2 rectenna array with on-chip cmos switching rectifier and on-pcb tapered slot antenna for wireless power transfer," *IEEE Trans. Microw. Theory Techn.*, vol. 69, no. 1, pp. 969–979, 2021.

[19] J. McSpadden and J. Mankins, "Space solar power programs and microwave wireless power transmission technology," *IEEE Microwave Magazine*, vol. 3, no. 4, pp. 46–57, 2002.

[20] Z. A. Pour, L. Shafai, and B. Tabachnick, "A practical approach to locate offset reflector focal point and antenna misalignment using vectorial representation of far-field radiation patterns," *IEEE Trans. Antennas Propag.*, vol. 62, no. 2, pp. 991–996, 2014.

[21] T. Shaw and D. Mitra, "Wireless power transfer system based on magnetic dipole coupling with high permittivity metamaterials," *IEEE Antennas Wireless Propag. Lett.*, vol. 18, no. 9, pp. 1823–1827, 2019.

[22] H. Bahrami, S. A. Mirbozorgi, R. Ameli, L. A. Rusch, and B. Gosselin, "Flexible, polarization-diverse UWB antennas for implantable neural recording systems," *IEEE Trans. Biomed. Circuits Syst.*, vol. 10, no. 1, pp. 38–48, 2016.

[23] C. Lu, X. Huang, X. Tao, X. Liu, C. Rong, Y. Zeng, and M. Liu, "Design and analysis of an omnidirectional dual-band wireless power transfer system," *IEEE Trans. Antennas Propag.*, vol. 69, no. 6, pp. 3493–3502, 2021.

[24] M. Haerinia and S. Noghanian, "Analysis of misalignment effects on link budget of an implantable antenna," in *2019 URSI International Symposium on Electromagnetic Theory (EMTS)*, pp. 1–4, 2019.

[25] C. Miozzi, G. Saggio, E. Gruppioni, and G. Marrocco, "Constrained safety-integrity performance of through-the-arms UHF-RFID transcutaneous wireless communication for the control of prostheses," *IEEE J. Radio Freq. Identif.*, vol. 3, no. 4, pp. 236–244, 2019.

[26] V. K. Srivastava, S. Kumar, and A. Sharma, "3D polarized field-forming for mitigation of angular misalignment problem in microwave power transfer systems," in *2021 IEEE 19th International Symposium on Antenna Technology and Applied Electromagnetics (ANTEM)*, pp. 1–2, 2021.

[27] S. F. Bo, J.-H. Ou, Y. Dong, S.-W. Dong, and X. Y. Zhang, "All-polarized wideband rectenna with enhanced efficiency within wide input power and load ranges," *IEEE Trans. Ind. Electron.*, vol. 69, no. 7, pp. 7470–7480, 2022.

[28] M. Wagih, A. S. Weddell, and S. Beeby, "Omnidirectional dual-polarized low-profile textile rectenna with over 50% efficiency for sub-μw/cm^2 wearable power harvesting," *IEEE Trans. Antennas Propag.*, vol. 69, no. 5, pp. 2522–2536, 2021.

[29] Y.-S. Chen and C.-W. Chiu, "Insertion loss characterization of impedance matching networks for low-power rectennas," *IEEE Trans. Compon. Packag. Manuf. Technol.*, vol. 8, no. 9, pp. 1632–1641, 2018.

[30] M. Kumar, S. Kumar, and A. Sharma, "Dual-purpose planar radial-array of rectenna sensors for orientation estimation and RF-energy harvesting at IoT nodes," *IEEE Microw. Wireless Compon. Lett.*, pp. 1–4, 2022.

[31] Y.-Y. Hu, S. Sun, H. Wu, S. Yang, and J. Hu, "Integrated coupler-antenna design for multibeam dual-polarized patch-array rectenna," *IEEE Trans. Antennas Propag.*, vol. 70, no. 3, pp. 1869–1883, 2022.

[32] M. Mattsson, C. I. Kolitsidas, and B. L. G. Jonsson, "Dual-band dual-polarized full-wave rectenna based on differential field sampling," *IEEE Antennas Wireless Propag. Lett.*, vol. 17, no. 6, pp. 956–959, 2018.

[33] T. Q. V. Hoang, E. Séguenot, F. Ferrero, J.-L. Dubard, P. Brachat, and J.-L. Desvilles, "3d voltage pattern measurement of a 2.45 ghz rectenna," *IEEE Trans. Antennas Propag.*, vol. 61, no. 6, pp. 3354–3356, 2013.

[34] M. Kumar, S. Kumar, and A. Sharma, "Dual-purpose planar radial-array of rectenna sensors for orientation estimation and RF-energy harvesting at iot nodes," *IEEE Microw. Wireless Compon. Lett.*, pp. 1–4, 2022.

[35] H. Sun, J. Huang, and Y. Wang, "An omnidirectional rectenna array with an enhanced RF power distributing strategy for RF energy harvesting," *IEEE Trans. Antennas Propag.*, pp. 1–1, 2022.

[36] W. Shepherd and K. M. A. Eissawi, "Some properties of a rectifier circuit with sinusoidal supply voltage and resistive load," *IEEE Trans. Ind. Electron. and Control Instrumentation*, vol. IECI-24, no. 2, pp. 183–191, 1977.

[37] S. Cochran, C. Zhao, and D. Costinett, "Multilevel switched-capacitor ac–dc step-down rectifier for wireless charging with reduced conduction loss and harmonic content," *IEEE Trans. Power Electron.*, vol. 37, no. 7, pp. 8669–8681, 2022.

[38] Y.-Y. Hu, S. Sun, H. Wu, S. Yang, and J. Hu, "Integrated coupler-antenna design for multibeam dual-polarized patch-array rectenna," *IEEE Trans. Antennas Propag.*, vol. 70, no. 3, pp. 1869–1883, 2022.

[39] D.-J. Lee, S.-J. Lee, I.-J. Hwang, W.-S. Lee, and J.-W. Yu, "Hybrid power combining rectenna array for wide incident angle coverage in RF energy transfer," *IEEE Trans. Microw. Theory Techn.*, vol. 65, no. 9, pp. 3409–3418, 2017.

[40] S.-T. Khang, D.-J. Lee, I.-J. Hwang, T.-D. Yeo, and J.-W. Yu, "Microwave power transfer with optimal number of rectenna arrays for midrange applications," *IEEE Antennas Wireless Propag. Lett.*, vol. 17, no. 1, pp. 155–159, 2018.

[41] W. Lin, R. W. Ziolkowski, and J. Huang, "Electrically small, low-profile, highly efficient, huygens dipole rectennas for wirelessly powering internet-of-things devices," *IEEE Trans. Antennas Propag.*, vol. 67, no. 6, pp. 3670–3679, 2019.

[42] D. Ahn, J.-S. Park, C.-S. Kim, J. Kim, Y. Qian, and T. Itoh, "A design of the low-pass filter using the novel microstrip defected ground structure," *IEEE Trans. Microw. Theory Techn.*, vol. 49, no. 1, pp. 86–93, 2001.

[43] M. Fantuzzi, G. Paolini, M. Shanawani, A. Costanzo, and D. Masotti, "An orientation-independent UHF rectenna array with a unified matching and decoupling RF network," *International Journal of Microwave and Wireless Technologies*, vol. 11, no. 5-6, p. 490–500, 2019.

[44] A. Eid, J. G. D. Hester, and M. M. Tentzeris, "5G as a wireless power grid," *Sci. Rep.*, vol. 11, p. 636, 2021.

[45] C. Chen, "A compact wideband endfire filtering antenna inspired by a uniplanar microstrip antenna," *IEEE Antennas Wireless Propag. Lett.*, vol. 21, no. 4, pp. 853–857, 2022.

[46] Z. He, H. Lin, and C. Liu, "Codesign of a schottky diode's and loop antenna's impedances for dual-band wireless power transmission," *IEEE Trans. Antennas Propag.*, vol. 19, no. 10, pp. 1813–1817, 2020.

[47] Y.-Y. Hu, S. Sun, H. Xu, and H. Sun, "Grid-array rectenna with wide angle coverage for effectively harvesting RF energy of low power density," *IEEE Trans. Microw. Theory Techn.*, vol. 67, no. 1, pp. 402–413, 2019.

[48] J. Kimionis, M. Isakov, B. S. Koh, A. Georgiadis, and M. M. Tentzeris, "3D-printed origami packaging with inkjet-printed antennas for RF harvesting sensors," *IEEE Trans. Microw. Theory Techn.*, vol. 63, no. 12, pp. 4521–4532, 2015.

[49] E. Vandelle, D. H. N. Bui, T.-P. Vuong, G. Ardila, K. Wu, and S. Hemour, "Harvesting ambient RF energy efficiently with optimal angular coverage," *IEEE Trans. Antennas Propag.*, vol. 67, no. 3, pp. 1862–1873, 2019.

[50] Y.-Y. Hu, S. Sun, and H. Xu, "Compact collinear quasi-yagi antenna array for wireless energy harvesting," *IEEE Access*, vol. 8, pp. 35308–35317, 2020.

[51] P. Prajapat, A. K. R, G. R, and C. Saha, "Near-omnidirectional 3D rectenna array for ambient microwave energy harvesting," in *2021 IEEE Indian Conference on Antennas and Propagation (InCAP)*, pp. 747–749, 2021.

[52] E. Vandelle, P. L. Doan, D. H. N. Bui, T. P. Vuong, G. Ardila, K. Wu, and S. Hemour, "High gain isotropic rectenna," in *2017 IEEE Wireless Power Transfer Conference (WPTC)*, pp. 1–4, 2017.

[53] Y.-Y. Hu, S. Sun, H.-J. Su, S. Yang, and J. Hu, "Dual-beam rectenna based on a short series-coupled patch array," *IEEE Trans. Antennas Propag.*, vol. 69, no. 9, pp. 5617–5630, 2021.

[54] S. Shen, C.-Y. Chiu, and R. D. Murch, "Multiport pixel rectenna for ambient RF energy harvesting," *IEEE Trans. Antennas Propag.*, vol. 66, no. 2, pp. 644–656, 2018.

[55] C. Song, P. Lu, and S. Shen, "Highly efficient omnidirectional integrated multiband wireless energy harvesters for compact sensor nodes of Internet-of-Things," *IEEE Trans. Ind. Electron.*, vol. 68, no. 9, pp. 8128–8140, 2021.

[56] S. F. Bo, J.-H. Ou, J. W. Wang, J. Tang, and X. Y. Zhang, "Polarization-independent rectifier with wide frequency and input power ranges based on novel six-port network," *IEEE Trans. Microw. Theory Techn.*, vol. 69, no. 11, pp. 4822–4830, 2021.

[57] L. Li, X. Zhang, C. Song, W. Zhang, T. Jia, and Y. Huang, "Compact dual-band, wide-angle, polarization angle independent rectifying metasurface for ambient energy

harvesting and wireless power transfer," *IEEE Trans. Microw. Theory Techn.*, vol. 69, no. 3, pp. 1518–1528, 2021.

[58] Y. Wei, J. Duan, H. Jing, Z. Lyu, J. Hao, Z. Qu, J. Wang, and B. Zhang, "A multiband, polarization-controlled metasurface absorber for electromagnetic energy harvesting and wireless power transfer," *IEEE Trans. Microw. Theory Techn.*, vol. 70, no. 5, pp. 2861–2871, 2022.

[59] A. Dolgov, R. Zane, and Z. Popovic, "Power management system for online low power RF energy harvesting optimization," *IEEE Trans. Circuits Syst. I: Regul. Pap.*, vol. 57, no. 7, pp. 1802–1811, 2010.

[60] Z. Popović, S. Korhummel, S. Dunbar, R. Scheeler, A. Dolgov, R. Zane, E. Falkenstein, and J. Hagerty, "Scalable RF energy harvesting," *IEEE Trans. Microw. Theory Techn.*, vol. 62, no. 4, pp. 1046–1056, 2014.

[61] T. Sakamoto, Y. Ushijima, E. Nishiyama, M. Aikawa, and I. Toyoda, "5.8 GHz series/parallel connected rectenna array using expandable differential rectenna units," *IEEE Trans. Antennas Propag.*, vol. 61, no. 9, pp. 4872–4875, 2013.

[62] B. Strassner, S. Kokel, and K. Chang, "5.8 GHz circularly polarized low incident power density rectenna design and array implementation," in *IEEE Antennas and Propagation Society International Symposium. Digest. Held in conjunction with: USNC/CNC/URSI North American Radio Sci. Meeting (Cat. No.03CH37450)*, vol. 3, pp. 950–953 vol.3, 2003.

[63] Y.-S. Chen and J.-W. You, "A scalable and multidirectional rectenna system for RF energy harvesting," *IEEE Trans. Compon. Packag. Manuf. Technol.*, vol. 8, no. 12, pp. 2060–2072, 2018.

[64] F. Erkmen and O. M. Ramahi, "A scalable, dual-polarized absorber surface for electromagnetic energy harvesting and wireless power transfer," *IEEE Trans. Microw. Theory Techn.*, vol. 69, no. 9, pp. 4021–4028, 2021.

[65] T. Matsunaga, E. Nishiyama, and I. Toyoda, "5.8 GHz stacked differential mode rectenna suitable for large-scale rectenna arrays," in *2013 Asia-Pacific Microwave Conference Proceedings (APMC)*, pp. 1200–1202, 2013.

[66] T. Matsunaga, E. Nishiyama, and I. Toyoda, "5.8 GHz stacked differential rectenna suitable for large-scale rectenna arrays with dc connection," *IEEE Trans. Antennas Propag.*, vol. 63, no. 12, pp. 5944–5949, 2015.

[67] A. Mavaddat, S. H. M. Armaki, and A. R. Erfanian, "Millimeter-wave energy harvesting using 4×4 microstrip patch antenna array," *IEEE Antennas Wireless Propag. Lett.*, vol. 14, pp. 515–518, 2015.

[68] K. Yasuda, E. Nishiyama, and I. Toyoda, "A high efficiency differential rectenna employing two-parasitic-element stacked antenna," in *2018 Asia-Pacific Microwave Conference (APMC)*, pp. 132–134, 2018.

[69] K. Saito, E. Nishiyama, and I. Toyoda, "A 2.45 and 5.8 GHz dual-band stacked differential rectenna with high conversion efficiency in low power density environment," *IEEE Open Journal of Antennas and Propagation*, pp. 1–1, 2022.

[70] Y. Ushijima, T. Sakamoto, E. Nishiyama, M. Aikawa, and I. Toyoda, "5.8 GHz integrated differential rectenna unit using both-sided mic technology with design flexibility," *IEEE Trans. Antennas Propag.*, vol. 61, no. 6, pp. 3357–3360, 2013.

[71] F. Erkmen, T. S. Almoneef, and O. M. Ramahi, "Scalable electromagnetic energy harvesting using frequency selective surfaces," *IEEE Trans. Microw. Theory Techn.*, vol. 66, no. 5, pp. 2433–2441, 2018.

[72] F. Erkmen, T. S. Almoneef, and O. M. Ramahi, "Electromagnetic energy harvesting using full-wave rectification," *IEEE Trans. Microw. Theory Techn.*, vol. 65, no. 5, pp. 1843–1851, 2017.

[73] T. S. Almoneef, F. Erkmen, M. A. Alotaibi, and O. M. Ramahi, "A new approach to microwave rectennas using tightly coupled antennas," *IEEE Trans. Antennas Propag.*, vol. 66, no. 4, pp. 1714–1724, 2018.

[74] T. S. Almoneef, H. Sun, and O. M. Ramahi, "A 3-D folded dipole antenna array for far-field electromagnetic energy transfer," *IEEE Antennas Wireless Propag. Lett.*, vol. 15, pp. 1406–1409, 2016.

[75] A. Georgiadis, G. Vera Andia, and A. Collado, "Rectenna design and optimization using reciprocity theory and harmonic balance analysis for electromagnetic (em) energy harvesting," *IEEE Antennas Wireless Propag. Lett.*, vol. 9, pp. 444–446, 2010.

[76] M. Giuseppina, G. Fabrizio, C., D. D. D., and T. Luciano, "Monopole-based rectenna for microwave energy harvesting of uhf rfid systems," *Progress In Electromagnetics Research C*, vol. 31, pp. 109–121, 2012.

[77] S. Ladan, N. Ghassemi, A. Ghiotto, and K. Wu, "Highly efficient compact rectenna for wireless energy harvesting application," *IEEE Microwave Magazine*, vol. 14, no. 1, pp. 117–122, 2013.

[78] M. K. Hosain, A. Z. Kouzani, M. F. Samad, and S. J. Tye, "A miniature energy harvesting rectenna for operating a head-mountable deep brain stimulation device," *IEEE Access*, vol. 3, pp. 223–234, 2015.

[79] S. T. Khang, J. W. Yu, and W.-S. Lee, "Compact folded dipole rectenna with rf-based energy harvesting for iot smart sensors," *Electronics Letters*, vol. 51, no. 12, pp. 926–928, 2015.

[80] A. Zhao and Z. Ren, "Wideband mimo antenna systems based on coupled-loop antenna for 5g n77/n78/n79 applications in mobile terminals," *IEEE Access*, vol. 7, pp. 93761–93771, 2019.

[81] A. Okba, A. Takacs, and H. Aubert, "Compact rectennas for ultra-low-power wireless transmission applications," *IEEE Trans. Microw. Theory Techn.*, vol. 67, no. 5, pp. 1697–1707, 2019.

[82] B. A. F. Esmail, H. A. Majid, S. H. Dahlan, Z. Z. abidin, M. Himdi, R. Dewan, M. K. A. Rahim, and A. Y. I. Ashyap, "Reconfigurable metamaterial structure for 5g beam tilting antenna applications," *Waves in Random and Complex Media*, vol. 31, no. 6, pp. 2089–2102, 2021.

[83] Z. Li, Y. Sun, M. Yang, Z. Wu, and P. Tang, "A broadband dual-polarized magneto-electric dipole antenna for 2g/3g/lte/wimax applications," *Progress In Electromagnetics Research C*, vol. 73, pp. 127–136, 2017.

[84] S. Lee, J. Hur, M.-B. Heo, S. Kim, H. Choo, and G. Byun, "A suboptimal approach to antenna design problems with kernel regression," *IEEE Access*, vol. 7, pp. 17461–17468, 2019.

[85] N. K. Darimireddy, R. R. Reddy, and A. M. Prasad, "A miniaturized hexagonal-triangular fractal antenna for wide-band applications [antenna applications corner]," *IEEE Antennas Propag. Mag.*, vol. 60, no. 2, pp. 104–110, 2018.

[86] H. Ullah and F. A. Tahir, "Broadband planar antenna array for future 5g communication standards," *IET Microwaves, Antennas & Propagation*, vol. 13, no. 15, pp. 2661–2668, 2019.

[87] M. Garg, A. Sharma, I. J. Garcia Zuazola, and A. Gupta, "Compact uhf rfid balun-like integrated tag antenna for long range detection of water bottles," *IET Microw. Antennas Propag.*, vol. 6, no. 6, pp. 1–8.

[88] R. Bhattacharya, R. Garg, and T. K. Bhattacharyya, "A compact yagi-uda type pattern diversity antenna driven by cpw-fed pseudomonopole," *IEEE Trans. Antennas Propag.*, vol. 64, no. 1, pp. 25–32, 2016.

[89] Y. Zhang, J.-Y. Deng, M.-J. Li, D. Sun, and L.-X. Guo, "A mimo dielectric resonator antenna with improved isolation for 5g mm-wave applications," *IEEE Antennas Wireless Propag. Lett.*, vol. 18, no. 4, pp. 747–751, 2019.

[90] Y. Shi, J. Jing, Y. Fan, L. Yang, and M. Wang, "Design of a novel compact and efficient rectenna for wifi energy harvesting," *Progress In Electromagnetics Research C*, vol. 83, pp. 57–70, 01 2018.

[91] F.-J. Huang, C.-M. Lee, C.-L. Chang, L.-K. Chen, T.-C. Yo, and C.-H. Luo, "Rectenna application of miniaturized implantable antenna design for triple-band biotelemetry communication," *IEEE Trans. Antennas Propag.*, vol. 59, no. 7, pp. 2646–2653, 2011.

[92] K. Niotaki, S. Kim, S. Jeong, A. Collado, A. Georgiadis, and M. M. Tentzeris, "A compact dual-band rectenna using slot-loaded dual band folded dipole antenna," *IEEE Antennas Wireless Propag. Lett.*, vol. 12, pp. 1634–1637, 2013.

[93] S. Shen, C.-Y. Chiu, and R. D. Murch, "A dual-port triple-band l-probe microstrip patch rectenna for ambient rf energy harvesting," *IEEE Antennas Wireless Propag. Lett.*, vol. 16, pp. 3071–3074, 2017.

[94] H. Zhang and T. Ngo, "Linear-polarization-insensitive rectenna design for ground-to-air microwave power transmission," *IEEE Access*, vol. 8, pp. 101702–101707, 2020.

[95] E. Brookner, W. M. Hall, and R. H. Westlake, "Faraday loss for l-band radar and communications systems," *IEEE Trans. Aerosp. Electron. Syst.*, vol. AES-21, no. 4, pp. 459–469, 1985.

[96] C. Counselman, "Multipath-rejecting gps antennas," *Proceedings of the IEEE*, vol. 87, no. 1, pp. 86–91, 1999.

[97] H. Sun and W. Geyi, "A new rectenna with all-polarization-receiving capability for wireless power transmission," *IEEE Antennas Wireless Propag. Lett.*, vol. 15, pp. 814–817, 2016.

[98] P. Lu, X.-S. Yang, J.-L. Li, and B.-Z. Wang, "Polarization reconfigurable broadband rectenna with tunable matching network for microwave power transmission," *IEEE Trans. Antennas Propag.*, vol. 64, no. 3, pp. 1136–1141, 2016.

[99] B. Clerckx, J. Kim, K. W. Choi, and D. I. Kim, "Foundations of wireless information and power transfer: Theory, prototypes, and experiments," *Proceedings of the IEEE*, vol. 110, no. 1, pp. 8–30, 2022.

[100] M. Deshpande and M. Bailey, "Input impedance of microstrip antennas," *IEEE Trans. Antennas Propag.*, vol. 30, no. 4, pp. 645–650, 1982.

[101] M. Kumar, S. Kumar, and A. Sharma, "A planar orbicular rectenna array system with 3-d uniform coverage for wireless powering of iot nodes," *IEEE Trans. Microw. Theory Techn.*, pp. 1–8, 2022.

[102] J.-M. Woo, W. Lim, J. Bae, C. M. Song, K.-J. Lee, S.-H. Yi, and Y. Yang, "Extendable array rectenna for a microwave wireless power transfer system," *IEEE Access*, vol. 9, pp. 98348–98360, 2021.

[103] A. A. Eteng, H. H. Goh, S. K. A. Rahim, and A. Alomainy, "A review of metasurfaces for microwave energy transmission and harvesting in wireless powered networks," *IEEE Access*, vol. 9, pp. 27518–27539, 2021.

[104] A. Quddious, M. A. B. Abbasi, A. Saghir, S. Arain, M. A. Antoniades, A. Polycarpou, P. Vryonides, and S. Nikolaou, "Dynamically reconfigurable sir filter using rectenna and active booster," *IEEE Trans. Microw. Theory Techn.*, vol. 67, no. 4, pp. 1504–1515, 2019.

[105] A. Dolgov, R. Zane, and Z. Popovic, "Power management system for online low power rf energy harvesting optimization," *IEEE Trans. Circuits Syst. I: Regul. Pap.*, vol. 57, no. 7, pp. 1802–1811, 2010.

[106] S. Wan and K. Huang, "Methods for improving the transmission-conversion efficiency from transmitting antenna to rectenna array in microwave power transmission," *IEEE Antennas Wireless Propag. Lett.*, vol. 17, no. 4, pp. 538–542, 2018.

[107] P. Lu, C. Song, and K. M. Huang, "A compact rectenna design with wide input power range for wireless power transfer," *IEEE Trans. Power Electron.*, vol. 35, no. 7, pp. 6705–6710, 2020.

[108] Y. H. Cho and W. J. Byun, "Generalized friis transmission equation for orbital angular momentum radios," *IEEE Trans. Antennas Propag.*, vol. 67, no. 4, pp. 2423–2429, 2019.

[109] D. Surender, T. Khan, F. A. Talukdar, and Y. M. Antar, "Rectenna design and development strategies for wireless applications: A review," *IEEE Antennas Propag. Mag.*, vol. 64, no. 5, pp. 16–29, 2022.

[110] S. Kumar, A. S. Dixit, R. R. Malekar, H. D. Raut, and L. K. Shevada, "Fifth generation antennas: A comprehensive review of design and performance enhancement techniques," *IEEE Access*, vol. 8, pp. 163568–163593, 2020.

[111] V. Palazzi, M. Del Prete, and M. Fantuzzi, "Scavenging for energy: A rectenna design for wireless energy harvesting in uhf mobile telephony bands," *IEEE Microwave Magazine*, vol. 18, no. 1, pp. 91–99, 2017.

[112] Z. Xu, A. Khalifa, A. Mittal, M. Nasrollahpourmotlaghzanjani, R. Etienne-Cummings, N. Xiang Sun, S. S. Cash, and A. Shrivastava, "Analysis and design methodology of rf energy harvesting rectifier circuit for ultra-low power applications," *IEEE Open Journal of Circuits and Systems*, vol. 3, pp. 82–96, 2022.

[113] D. Hamill, "An efficient active ripple filter for use in dc-dc conversion," *IEEE Trans. Aerosp. Electron. Syst.*, vol. 32, no. 3, pp. 1077–1084, 1996.

[114] D. Newell and M. Duffy, "Review of power conversion and energy management for low-power, low-voltage energy harvesting powered wireless sensors," *IEEE Trans. Power Electron.*, vol. 34, no. 10, pp. 9794–9805, 2019.

[115] A. Quddious, S. Zahid, F. A. Tahir, M. A. Antoniades, P. Vryonides, and S. Nikolaou, "Dual-band compact rectenna for uhf and ism wireless power transfer systems," *IEEE Trans. Antennas Propag.*, vol. 69, no. 4, pp. 2392–2397, 2021.

[116] S. Shen, C.-Y. Chiu, and R. D. Murch, "A dual-port triple-band l-probe microstrip patch rectenna for ambient rf energy harvesting," *IEEE Antennas Wireless Propag. Lett.*, vol. 16, pp. 3071–3074, 2017.

[117] Y. Ishizawa, "Efficiency estimation of microwave power transmission antenna system," *Electronics and Communications in Japan (Part I: Communications)*, vol. 83, no. 8, pp. 94–104, 2000.

[118] T. Miura, N. Shinohara, and H. Matsumoto, "Experimental study of rectenna connection for microwave power transmission," *Electronics and Communications in Japan (Part II: Electronics)*, vol. 84, pp. 1–8, 02 2001.

[119] R. R. Potera and T. J. Han, "Silicon carbide diodes in power-factor correction circuits: Device and circuit design aspects," *IEEE Power Electronics Magazine*, vol. 6, no. 1, pp. 34–39, 2019.

[120] S. Shen, M. Yu, S. Zhang, X. Zhang, and J. Xu, "An equivalent-circuit model of planar gaas schottky diode for terahertz application," in *2018 10th International Conference on Communications, Circuits and Systems (ICCCAS)*, pp. 34–37, 2018.

[121] Q. Zhang, J.-H. Ou, Z. Wu, and H.-Z. Tan, "Novel microwave rectifier optimizing method and its application in rectenna designs," *IEEE Access*, vol. 6, pp. 53557–53565, 2018.

[122] C. Song, Y. Huang, P. Carter, J. Zhou, S. Yuan, Q. Xu, and M. Kod, "A novel six-band dual cp rectenna using improved impedance matching technique for ambient rf energy harvesting," *IEEE Trans. Antennas Propag.*, vol. 64, no. 7, pp. 3160–3171, 2016.

[123] C. Song, Y. Huang, J. Zhou, P. Carter, S. Yuan, Q. Xu, and Z. Fei, "Matching network elimination in broadband rectennas for high-efficiency wireless power transfer and energy harvesting," *IEEE Trans. Ind. Electron.*, vol. 64, no. 5, pp. 3950–3961, 2017.

[124] U. Guler and M. Ghovanloo, "Power management in wireless power-sipping devices: A survey," *IEEE Circuits and Systems Magazine*, vol. 17, no. 4, pp. 64–82, 2017.

[125] M. S. Reese, C. A. Balanis, C. R. Blncher, and G. C. Barber, "Modeling and simulation of a helicopter-mounted satcom antenna array," *IEEE Antennas Propag. Mag.*, vol. 53, no. 2, pp. 51–60, 2011.

[126] H. Sun, H. He, and J. Huang, "Polarization-insensitive rectenna arrays with different power combining strategies," *IEEE Antennas Wireless Propag. Lett.*, vol. 19, no. 3, pp. 492–496, 2020.

[127] S. Shen, Y. Zhang, C.-Y. Chiu, and R. Murch, "Multiport rectennas for ambient rf energy harvesting," in *2019 IEEE MTT-S International Wireless Symposium (IWS)*, pp. 1–3, 2019.

[128] S. Shen and B. Clerckx, "Beamforming optimization for mimo wireless power transfer with nonlinear energy harvesting: Rf combining versus dc combining," *IEEE Trans. Wirel. Commun.*, vol. 20, no. 1, pp. 199–213, 2021.

[129] C. Song, Y. Ding, A. Eid, J. G. D. Hester, X. He, R. Bahr, A. Georgiadis, G. Goussetis, and M. M. Tentzeris, "Advances in wirelessly powered backscatter communications: From antenna/RF circuitry design to printed flexible electronics," *Proc. IEEE Proc. IRE*, vol. 110, no. 1, pp. 171–192, 2022.

[130] D. Belo, D. C. Ribeiro, P. Pinho, and N. Borges Carvalho, "A selective, tracking, and power adaptive far-field wireless power transfer system," *IEEE Trans. Microw. Theory Techn.*, vol. 67, no. 9, pp. 3856–3866, 2019.

[131] N. Shinohara and H. Matsumoto, "Dependence of dc output of a rectenna array on the method of interconnection of its array elements," *ELECTR ENG JPN.*, vol. 125, no. 1, pp. 9–17, 1998.

[132] C. Chen, "A compact wideband endfire filtering antenna inspired by a uniplanar microstrip antenna," *IEEE Antennas Wireless Propag. Lett.*, vol. 21, no. 4, pp. 853–857, 2022.

[133] C. Liu, H. Lin, Z. He, and Z. Chen, "Compact patch rectennas without impedance matching network for wireless power transmission," *IEEE Trans. Microw. Theory Techn.*, vol. 70, no. 5, pp. 2882–2890, 2022.

[134] N. Shinohara and H. Matsumoto, "Dependence of dc output of a rectenna array on the method of interconnection of its array elements," *ELECTR ENG JPN.*, vol. 125, no. 1, pp. 9–17, 1998.

[135] T. Miura, N. Shinohara, and H. Matsumoto, "Experimental study of rectenna connection for microwave power transmission," *Electron Commun Jpn.*, vol. 84, no. 2, pp. 27–36, 2001.

[136] M.-C. Tang, T. Shi, and R. W. Ziolkowski, "Flexible efficient quasi-yagi printed uniplanar antenna," *IEEE Trans. Antennas Propag.*, vol. 63, no. 12, pp. 5343–5350, 2015.

[137] W. Lin, R. W. Ziolkowski, and J. Huang, "Electrically small, low-profile, highly efficient, huygens dipole rectennas for wirelessly powering internet-of-things devices," *IEEE Trans. Antennas Propag.*, vol. 67, no. 6, pp. 3670–3679, 2019.

[138] M. Wagih, G. S. Hilton, A. S. Weddell, and S. Beeby, "Broadband millimeter-wave textile-based flexible rectenna for wearable energy harvesting," *IEEE Trans. Microw. Theory Techn.*, vol. 68, no. 11, pp. 4960–4972, 2020.

[139] T. Mitani, S. Kawashima, and T. Nishimura, "Analysis of voltage doubler behavior of 2.45-ghz voltage doubler-type rectenna," *IEEE Trans. Microw. Theory Techn.*, vol. 65, no. 4, pp. 1051–1057, 2017.

[140] S.-B. Liu, F.-S. Zhang, M. Boyuan, S.-P. Gao, and Y.-X. Guo, "Multiband dual-polarized hybrid antenna with complementary beam for simultaneous rf energy harvesting and wpt," *IEEE Trans. Antennas Propag.*, pp. 1–1, 2022.

[141] S. F. Bo, J.-H. Ou, Y. Dong, S.-W. Dong, and X. Y. Zhang, "All-polarized wideband rectenna with enhanced efficiency within wide input power and load ranges," *IEEE Trans. Ind. Electron.*, vol. 69, no. 7, pp. 7470–7480, 2022.

[142] M.-J. Nie, X.-X. Yang, G.-N. Tan, and B. Han, "A compact 2.45 GHz broadband rectenna using grounded coplanar waveguide," *IEEE Antennas Wireless Propag. Lett.*, vol. 14, pp. 986–989, 2015.

[143] Y. Luo, Q.-X. Chu, and J. Bornemann, "A differential-fed yagi-uda antenna with enhanced bandwidth via addition of parasitic resonator," *Microwave and Optical Technology Letters*, vol. 59, pp. 156–159, 01 2017.

[144] M. Farran, S. Boscolo, A. Locatelli, A.-D. Capobianco, M. Midrio, V. Ferrari, and D. Modotto, "Compact quasi-yagi antenna with folded dipole fed by tapered integrated balun," *Electronics Letters*, vol. 52, no. 10, pp. 789–790, 2016.

[145] S. S. Jehangir and M. S. Sharawi, "A miniaturized uwb biplanar yagi-like mimo antenna system," *IEEE Antennas Wireless Propag. Lett.*, vol. 16, pp. 2320–2323, 2017.

[146] Y. Luo and Q.-X. Chu, "A yagi–uda antenna with a stepped-width reflector shorter than the driven element," *IEEE Antennas Wireless Propag. Lett.*, vol. 15, pp. 564–567, 2016.

[147] A. P. Sohrab, Y. Huang, M. Hussein, M. Kod, and P. Carter, "A uhf rfid tag with improved performance on liquid bottles," *IEEE Antennas Wireless Propag. Lett.*, vol. 15, pp. 1673–1676, 2016.

[148] A. Dubok and A. B. Smolders, "Miniaturization of robust uhf rfid antennas for use on perishable goods and human bodies," *IEEE Antennas Wireless Propag. Lett.*, vol. 13, pp. 1321–1324, 2014.

[149] Z. Zhao, Z. Lu, R. Ma, Y. Liu, L. Han, and W. Zhang, "Compact uhf rfid tag antenna for platform tolerant applications," in *2018 International Conference on Microwave and Millimeter Wave Technology (ICMMT)*, pp. 1–3, 2018.

[150] T. Deleruyelle, P. Pannier, M. Egels, and E. Bergeret, "An rfid tag antenna tolerant to mounting on materials," *IEEE Antennas Propag. Mag.*, vol. 52, no. 4, pp. 14–19, 2010.

[151] S. R. Aroor and D. D. Deavours, "Evaluation of the state of passive uhf rfid: An experimental approach," *IEEE Systems Journal*, vol. 1, no. 2, pp. 168–176, 2007.

[152] M. C. Caccami and G. Marrocco, "Electromagnetic modeling of self-tuning rfid sensor antennas in linear and nonlinear regimes," *IEEE Trans. Antennas Propag.*, vol. 66, no. 6, pp. 2779–2787, 2018.

[153] L. J. Görtschacher and J. Grosinger, "Uhf rfid sensor system using tag signal patterns: Prototype system," *IEEE Antennas Wireless Propag. Lett.*, vol. 18, no. 10, pp. 2209–2213, 2019.

[154] D. Kim and J. Yeo, "Low-profile rfid tag antenna using compact amc substrate for metallic objects," *IEEE Antennas Wireless Propag. Lett.*, vol. 7, pp. 718–720, 2008.

[155] X. Qing, C. K. Goh, and Z. N. Chen, "Impedance characterization of rfid tag antennas and application in tag co-design," *IEEE Trans. Microw. Theory Techn.*, vol. 57, no. 5, pp. 1268–1274, 2009.

[156] M. Li, Z. Niu, and Y. Wang, "An electrically small antenna with a bidirectional radiation pattern for uhf rfid tags," in *2018 International Conference on Microwave and Millimeter Wave Technology (ICMMT)*, pp. 1–3, 2018.